



Cite as

Nano-Micro Lett.
(2023) 15:52

Received: 9 November 2022

Accepted: 4 January 2023

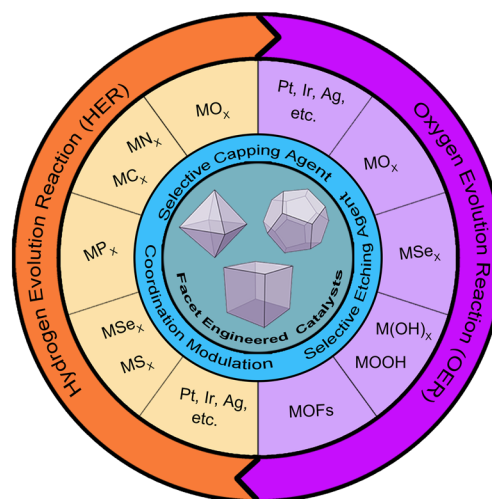
© The Author(s) 2023

Facet Engineering of Advanced Electrocatalysts
Toward Hydrogen/Oxygen Evolution ReactionsChangshui Wang¹, Qian Zhang¹ ✉, Bing Yan¹, Bo You² ✉, Jiaojiao Zheng¹, Li Feng¹,
Chunmei Zhang³, Shaohua Jiang¹, Wei Chen^{4,5,6} ✉, Shuijian He¹ ✉

HIGHLIGHTS

- The crystal facets featured with facet-dependent physical and chemical properties can exhibit varied electrocatalytic activity toward hydrogen evolution reaction (HER) and oxygen evolution reaction (OER) attributed to their anisotropy.
- The highly active exposed crystal facets enable increased mass activity of active sites, lower reaction energy barriers, and enhanced catalytic reaction rates for HER and OER.
- The formation mechanism and control strategy of the crystal facet, significant contributions as well as challenges and perspectives of facet-engineered catalysts for HER and OER are provided.

ABSTRACT The electrocatalytic water splitting technology can generate high-purity hydrogen without emitting carbon dioxide, which is in favor of relieving environmental pollution and energy crisis and achieving carbon neutrality. Electrocatalysts can effectively reduce the reaction energy barrier and increase the reaction efficiency. Facet engineering is considered as a promising strategy in controlling the ratio of desired crystal planes on the surface. Owing to the anisotropy, crystal planes with different orientations usually feature facet-dependent physical and chemical properties, leading to differences in the adsorption energies of oxygen or hydrogen intermediates, and thus exhibit varied electrocatalytic activity toward hydrogen evolution reaction (HER) and oxygen evolution reaction (OER). In this review, a brief introduction of the basic concepts, fundamental understanding of the reaction mechanisms as well as key evaluating parameters for both HER and OER are provided. The formation mechanisms of the crystal facets are comprehensively overviewed aiming to give scientific theory guides to realize dominant crystal planes.



✉ Qian Zhang, zhangqian5689@njfu.edu.cn; Bo You, youbo@hust.edu.cn; Wei Chen, weichen@ciac.ac.cn; Shuijian He, shuijianhe@njfu.edu.cn

¹ International Innovation Center for Forest Chemicals and Materials, Co-Innovation Center of Efficient Processing and Utilization of Forest Resources, Nanjing Forestry University, Nanjing 210037, People's Republic of China² Key Laboratory of Material Chemistry for Energy Conversion and Storage, Ministry of Education, Hubei Key Laboratory of Material Chemistry and Service Failure, School of Chemistry and Chemical Engineering, Huazhong University of Science and Technology (HUST), Wuhan 430074, People's Republic of China³ Institute of Materials Science and Devices, School of Materials Science and Engineering, Suzhou University of Science and Technology, Suzhou 2150009, People's Republic of China⁴ Guangxi Key Laboratory of Low Carbon Energy Materials, College of Chemistry and Pharmaceutical Sciences, Guangxi Normal University, Guilin 541004, People's Republic of China⁵ State Key Laboratory of Electroanalytical Chemistry, Changchun Institute of Applied Chemistry, Chinese Academy of Sciences, Changchun 130022, People's Republic of China⁶ University of Science and Technology of China, Hefei 230026, People's Republic of China

Subsequently, three strategies of selective capping agent, selective etching agent, and coordination modulation to tune crystal planes are comprehensively summarized. Then, we present an overview of significant contributions of facet-engineered catalysts toward HER, OER, and overall water splitting. In particular, we highlight that density functional theory calculations play an indispensable role in unveiling the structure–activity correlation between the crystal plane and catalytic activity. Finally, the remaining challenges in facet-engineered catalysts for HER and OER are provided and future prospects for designing advanced facet-engineered electrocatalysts are discussed.

KEYWORDS Crystal facet engineering; Anisotropy; Oxygen evolution reaction; Hydrogen evolution reaction; Theoretical simulations

1 Introduction

Due to excessive consumption of conventional fossil fuels, global energy crisis and environmental issues are arisen [1–5]. In order to achieve the future low-carbon energy economy, the exploration and utilization of green and sustainable energy sources is crucial and highly urgent. Hydrogen as the most promising energy carriers has gained increasing attention by virtue of its high energy storage capacity, carbon-free nature, and renewable nature [6–10]. Till date, hydrogen production can be realized via natural gas, other fossil fuels, and water electrolysis [1, 11]. Among these approaches, environmentally friendly electrochemical water splitting produces high-purity hydrogen, which is an efficient method to realize carbon neutrality [12–16]. However, the OER involves multiple electron transfer steps and oxygen–oxygen bond formation process, which is regarded as the main bottleneck of hydrogen production from water splitting [7, 17–21]. Furthermore, as a strongly uphill reaction, electrocatalytic splitting of water into hydrogen and oxygen typically requires a higher voltage of 1.8–2.0 V to proceed compared to the theoretical limit of 1.23 V [22, 23]. The electrocatalysts can effectively improve the sluggish kinetics and reduce the overpotentials (η) of HER and OER [24, 25]. Therefore, the elaborate design of HER and OER electrocatalysts for achieving high-efficiency hydrogen production and carbon neutrality is of considerable interest and great significance.

In recent decades, noble metals (Pt, Ir, Ag, etc.), transition metal oxides/phosphides/chalcogenides, metal–organic frameworks (MOFs), and their derivatives have been developed as high-performance electrocatalysts for HER and OER [19, 24, 26–49]. In order to enhance the performance of electrocatalysts, state-of-the-art strategies to tune their electronic structures and further adjust adsorption energies of oxygen or hydrogen intermediates are explored including interface engineering, doping engineering as well as defect engineering [50–69]. However, it has been overlooked that

some electrocatalysts possess well-defined crystal planes with special atomic arrangements and atomic coordination environments, which might exert a positive and profound impact on electrocatalytic performance [70, 71]. Owing to the anisotropy of the crystal planes, some electrocatalysts featured with multiple crystal planes usually exhibit facet-dependent physical and chemical properties including geometric structures, surface electronic structures, surface built-in electric fields, and redox active sites, which causes differences in the adsorption energies of oxygen or hydrogen intermediates, thus leading to different electrochemical activity and selectivity toward HER or OER [30, 72–77]. Remarkably, the X-ray absorption spectroscopy (XAS) is capable of investigating the chemical states and atomic structures of metal ions in facet-engineered catalysts [78]. For instance, local structures of Ir atoms in 2D ultrathin {001}-faceted SrIrO₃ perovskite were analyzed through the XAS. The XAS results confirmed that electron density around Ir atoms is richer and the Ir–O coordination number is 5.8 close to an ideal coordination of 6 [77]. The XAS is conducted to investigate Co oxidation states, electron occupancies, and coordination environments of PrBaCo₂O₆ films with the {100} facets. The XAS results indicated that PrBaCo₂O₆ films with the {100} facets presented more high-spin Co³⁺ states, which can tailor their electronic structure [79]. Besides, the highly active exposed facet should have more reactive active sites, which greatly improves the mass activity of active sites [80–82]. Thus, selective exposure of dominant crystal planes has been regarded as the effective strategy for achieving increased mass activity of active sites, decreasing reaction energy barriers and increasing catalytic reaction rates [83–86]. Nevertheless, it is still challenging to tune catalyst morphology to realize highly active exposed dominant crystal planes without changing the composition.

The crystal morphology can roughly reflect the categories and proportions of main crystal planes [87]. In addition, different crystal planes show different surface energy, resulting in different selective toward HER or OER [30, 82, 88–91].

For example, the high-index facets (edges, steps, and kinks) featured with a high ratio of low-coordinated atoms usually exhibited a higher surface energy than low-index facets, indicating favorable surface atomic structures and hence enhanced electrocatalytic activity for the high-index facets [30, 87, 92–98]. Therefore, optimizing crystal morphology to expose highly active facets with high surface energy can effectively ameliorate electrocatalytic activity. The surface energy across the crystal surface would tend to minimize during the crystal growth process based on Gibbs–Wulff theorem [99]. More specifically, crystal facets with high surface energy would slowly decrease or even disappear, which reduces electrocatalytic activity. Fortunately, during the growth of the crystal, some additives have emerged as effective capping agents or etching agents in controlling the crystal growth process and to obtain targeted crystal morphology aiming to preserve the highly active crystal facets [72]. Crystal facet engineering is capable of controlling and further expanding the percentage of desired crystal facets on the crystal surface. Accordingly, it is an effective strategy to tailor crystal morphology with the assistance of crystal facet engineering for designing electrocatalysts dominated by high-activity facets (Fig. 1).

With the increasing demand for high-efficiency catalysts, the last decades have witnessed the boom of facet-engineered catalysts for electrochemical hydrogen and oxygen evolution. However, a comprehensive summary in facet-engineered electrocatalysts toward the HER and OER is still lacking. Herein, in this review, we provide a systematic summary of facet engineering for HER, OER, and overall water splitting (OWS) (Fig. 1). First, this review starts from the basic concepts, fundamental mechanisms, and evaluation parameters of HER and OER. Meanwhile, the formation mechanism of the crystal facet is highlighted. Then, various strategies of selective capping agent, selective etching agent, and coordination modulation to tailor crystal facets are summarized. Next, a comprehensive overview of significant contributions of facet-engineered catalysts for HER, OER, and OWS is given. Importantly, we point out that the DFT calculations play a fundamental role in accounting for the structure–activity correlation between the crystal plane and catalytic activity. Finally, the challenges and perspectives in facet-engineered catalysts for HER and OER are proposed from our point of view.

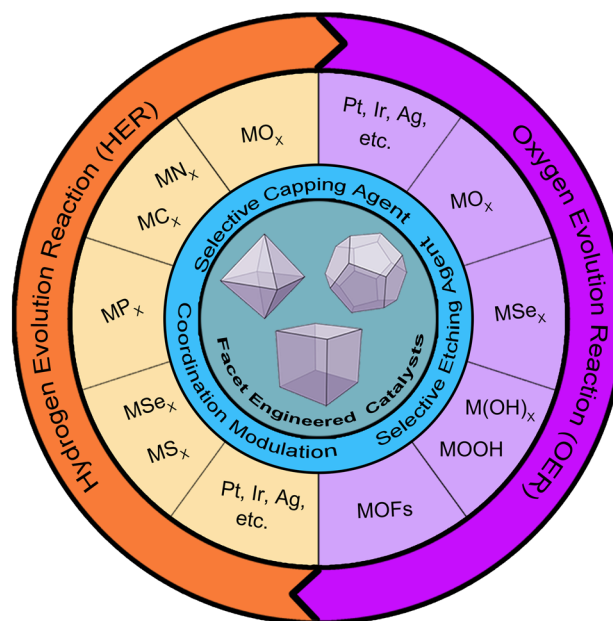


Fig. 1 Summaries of crystal facet control strategies and facet-engineered catalysts for electrocatalysis of HER and OER. M represents transition metals, e.g., Fe, Co, Ni, Cu

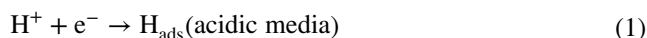
2 Fundamentals of OER and HER

2.1 HER Mechanisms

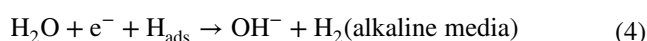
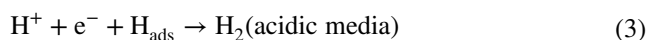
Hydrogen production from electrochemical water splitting involves two different reaction pathways including the reduction of protons in the solution via the Volmer step and generation of hydrogen through electrochemical (the Heyrovsky step) or chemical (Tafel step) route (Fig. 2) [3, 28, 100–103]. The first step of HER is the Volmer reaction, wherein an electron (e^-) transfers to the electrode can react with the H^+ or H_2O in acidic or alkaline solution on a void active site of the catalyst to produce the adsorbed hydrogen atoms (H_{ads}) (Eq. (1) or (2)). Subsequently, the second step is associated with desorption and accumulation of the H_{ads} for H_2 formation [104]. This process could be proceeded either via the Tafel step or the Heyrovsky step (Eqs. (3), (4), or (5)) [42, 105–108]. A low occupancy of H_{ads} on the catalyst surface allows it to transfer an electron and react with H^+ in the solution to produce H_2 . This process is a Heyrovsky reaction

[104]. The formation of H_2 is caused by the bonding between adjacent H_{ads} when their occupancy is high on the catalyst surface. This process is a Tafel reaction [36]. The difference of HER mechanisms in acidic media and alkaline media lies in the proton source [3]. In acidic media, hydronium ions (H_3O^+) are the proton source, while in alkaline media, the proton source is derived from water molecules.

Volmer Step



Heyrovsky Step



The Tafel slope demonstrates the potential difference required to change the current density by order of magnitudes, which is beneficial to discern the mechanism of the HER process [3, 109, 110]. In case the proton discharge reaction is rapid and H_2 formed via a rate-determining step (RDS) of chemical desorption, a Tafel slope of 29 mV dec^{-1} is expected according to the formula ($b = 2.3RT/2F$) at $25 \text{ }^\circ\text{C}$. In case the proton discharge reaction is rapid and H_2 is produced through the rate-limiting step of electrochemical

desorption, a Heyrovsky slope of 38 mV dec^{-1} is deduced from the formula ($b = 4.6RT/3F$) at $25 \text{ }^\circ\text{C}$. In case the proton discharge reaction is slow, a large slope of 116 mV dec^{-1} is acquired from the formula ($b = 4.6RT/F$) at $25 \text{ }^\circ\text{C}$.

2.2 OER Mechanisms

The development and design of high-performance energy conversion and storage systems, including small molecule (water, carbon dioxide and nitrogen) electrolyzers, metal–air batteries, and regenerative fuel cells, are of essential importance for realizing carbon neutrality [111–113]. As shown in Fig. 3, the OER has been regarded as a key reaction process among these electrochemical devices, which can build a bridge between renewable electricity and chemical fuels [114]. For example, the OER can proceed at the anode during the electrolysis of small molecules (Fig. 3a), while the OER occurs on the cathode in metal–air battery (Fig. 3b). A regenerative fuel cell requires participation of powerful oxygen electrolysis to produce high electrical energy (Fig. 3c). However, sluggish kinetics of OER reduces the electrochemical efficiency of these electrochemical devices. The design and exploration of high-performance OER catalysts for improving the efficiency of energy conversion and storage systems are a key step of carbon neutrality. Therefore, in the following, a brief summary of OER mechanisms is

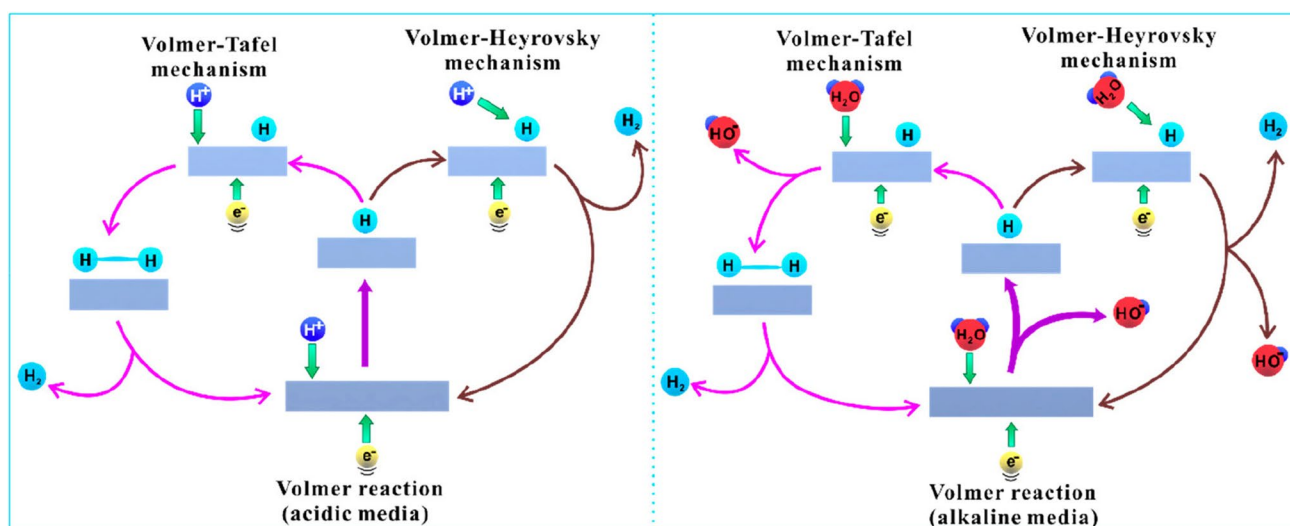


Fig. 2 Schematic diagram of HER mechanisms in acidic media (left) and in alkaline media (right). Reproduced with permission [3]. Copyright 2020, American Chemical Society

presented intending to rational design OER electrocatalysts with high catalytic activity.

2.2.1 Conventional Adsorbate Evolution Mechanism

Mechanistically, oxygen formation occurs on the surface of the anode electrode in two possible reaction pathways: one is the conventional adsorbate evolution mechanism (AEM) and another is the lattice oxygen mechanism (LOM) as depicted in Fig. 4a-c [115–121]. Generally, the OER process of AEM in acidic medium or alkaline medium undergoes four concerted proton–electron transfer steps with multiple oxygenated intermediates (*OH, *O and *OOH) [106, 122, 123]. Taking the alkaline OER process of AEM as an example (Fig. 4d), hydroxide anions firstly adsorb on the active site (*) through one-electron oxidation process, producing an *OH. Subsequently, *OH is coupled to hydroxide anions forming *O. Then, O* combines with another OH to generate *OOH. O₂ is produced through the deprotonation of *OOH with the restoration of initial activity. In theory, the energy barrier of OER might be originated from each

of the four steps. The step with the largest positive value among $\Delta G_1 \sim \Delta G_4$ is identified as the RDS and determines the theoretical η of OER [124]. As displayed in Fig. 4e, for an ideal catalyst, all four reaction steps would have a reaction free energy of 1.23 eV at $U=0$ [125]. However, catalysts cannot achieve this ideal situation in practice because oxygenated intermediates have linearly related adsorption energies [126]. Particularly, the O atom from both *OH and *OOH binds with the surface of catalyst by a single bond [126]. Thus, a linear relationship exists between *OH and *OOH, where the slope is approximately 1 and the intercept is 3.2 eV, which only affects the oxygenated intermediates' interactions with the catalyst surface. Interestingly, ΔG_{*OOH} can be deduced from ΔG_{*OH} , resulting in a lower limit for η of OER. Since two proton–electron transfer steps of an ideal catalyst possess the energy separation of 2.46 (2×1.23) eV, the lowest theoretical η of 0.37 eV (i.e., $[3.2 - 2.46 \text{ eV}]/2$) is acquired [114, 126, 127]. In consideration of a constant adsorption energy difference of 3.2 eV between ΔG_{*OOH} and ΔG_{*OH} , the OER overpotential is determined by *O adsorption energy. In other words, the second or third reaction step might be the RDS for OER [126].

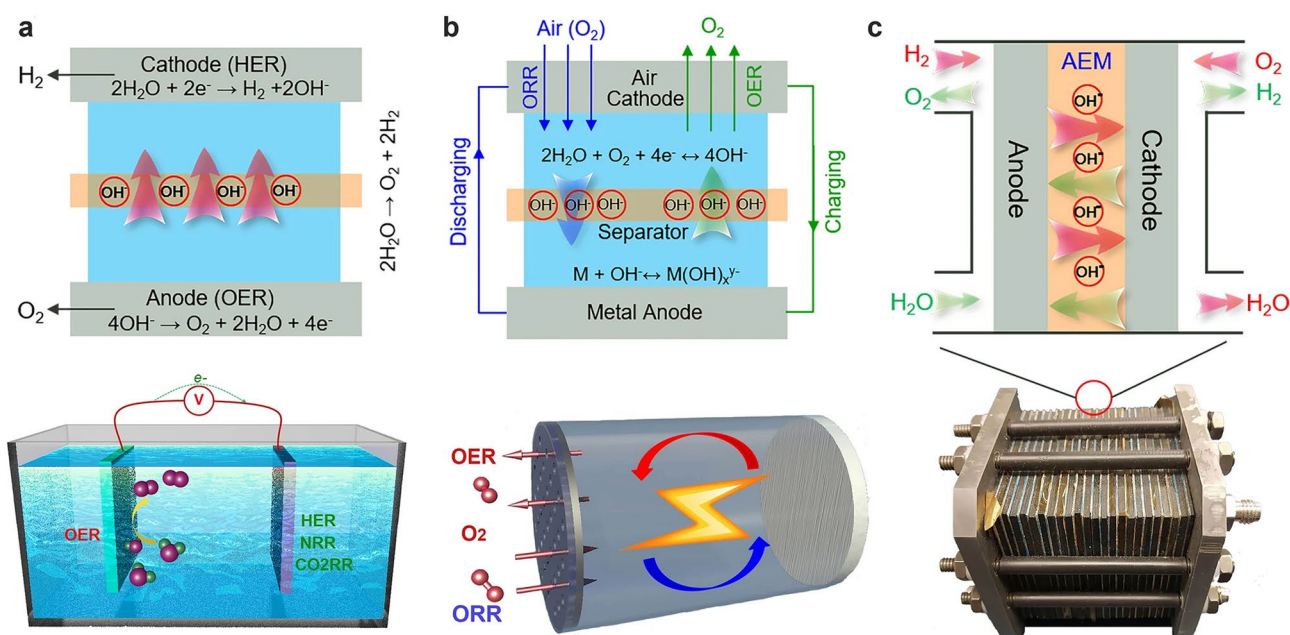


Fig. 3 The OER involved energy conversion and storage devices: **a** small molecule electrolyzers, **b** metal–air batteries, **c** regenerative fuel cells. Reproduced with permission [114]. Copyright 2022, Springer Nature

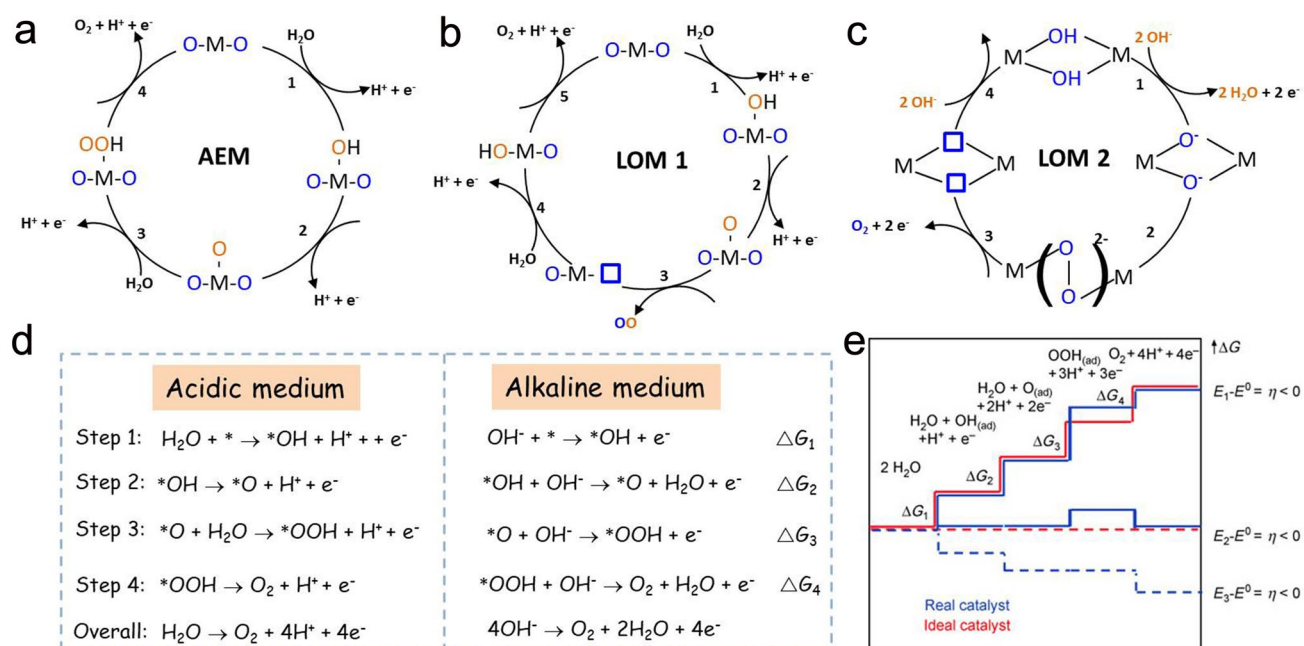


Fig. 4 **a** AEM for OER. **b** LOM 1 for OER with one oxygen atom originated from the catalyst to form oxygen molecular. **c** LOM 2 for OER with both oxygen atoms of oxygen molecular derived from the catalyst. **d** Schematic diagram of AEMs for OER in acidic and alkaline electrolyte. **e** OER Gibbs free energy diagram versus reaction pathways for reactive species and intermediates. Red and blue lines represent ideal and real reaction pathways, respectively. Reproduced with permission [125]. Copyright 2010, Wiley-VCH Verlag GmbH & Co

2.2.2 Lattice Oxygen Mechanism

The traditional AEM followed by the scaling relationship between $*OOH$ and $*OH$ cannot surpass the limitation of minimal overpotential of 0.37 V [116, 128–130]. Fortunately, the emerged LOM can offer a unique reaction pathway for the occurrence of O–O bond coupling, wherein it would neither fully undergo reaction pathways of the AEM and nor restricted by the scaling relationship of the oxygenated intermediates [27, 131, 132]. As shown in Fig. 4b, c, there are two types of LOM reaction pathways, depending on the number of oxygen atom derived from catalysts [50, 128, 133]. The first two steps of LOM 1 and LOM 2 are consistent with the AEM for OER. In the third step of LOM 1, the $*O$ species can couple with the lattice oxygen in the catalyst to yield an O_2 molecule, which generates oxygen vacancy in the catalyst simultaneously. Next, the oxygen vacancy is refilled by a water molecule, producing $*OH$ on the M site of M–O. Finally, H is released to yield refreshed M active sites [132]. For LOM 2, two $*OH$ on the M firstly go through deprotonation intending to

producing two metal-oxo species. Subsequently, an O–O bond is formed by coupling two oxo species. Finally, oxygen gas is evolved through exposing two oxygen vacancies occupied by OH [128, 134].

2.3 Key Evaluating Parameters of the HER and OER

2.3.1 Overpotential

Due to the kinetic energy barrier, electrocatalytic OER or HER can proceed through the additional potential to drive oxygen or hydrogen production. The additional potential is named overpotential (η), which is obtained from the potential difference between the experimental value and the thermodynamic equilibrium value [104]. η is regarded as one of the dominating factors to evaluate the electrocatalytic performance [135]. η at a geometric current density of 10 mA cm^{-2} originated from the potential corresponding to photoelectrocatalytic H_2O splitting efficiency of 10% is widely accepted to evaluate the HER and OER performances

of the electrocatalysts [136, 137]. Generally, an electrocatalyst with high catalytic activity would exhibit lower overpotential.

2.3.2 Tafel Slope

The Tafel slope (b) depicts the reaction kinetics of the electrochemical reaction, which can offer valuable and insightful information toward reaction mechanisms, especially for elucidating the RDS [138]. The Tafel slope is calculated from the linear portion of the Tafel plot. The Tafel equation is expressed as $\eta = a + b \log(j/j_0)$, where a represents the constant determined by temperature, electrode properties, and electrolyte [11], j is the total current density at a given η , and j_0 is the exchange current density. The Tafel value is associated with the reaction mechanisms, especially for the HER [3, 138]. j_0 reveals the intrinsic activity of a specific electrocatalyst under equilibrium conditions [109]. Generally speaking, an electrocatalyst with high catalytic activity would exhibit a small Tafel slope (b) and a high j_0 .

2.3.3 Stability

Stability performance is regarded as another crucial parameter in evaluating catalysts for practical applications. The first approach to evaluate the stability is comparing the change between the linear sweep voltammetry (LSV) curve before and after a certain number of cyclic voltammetric scans [11]. The second method of stability test is conducted via monitoring the current density (potential) variation with time at a fixed potential (current density) [139]. The third method (denoted as multi-step chronopotentiometric test) to judge the stability is to monitor the changes of potential (corresponding to the same current density) after running at varied current densities within multiple cycles. Generally, a smaller change at the same current density indicates better stability toward HER and OER.

2.3.4 Turnover Frequency

Turnover frequency (TOF) is another vital parameter for evaluating the intrinsic activity of an electrocatalyst [139]. The TOF value can be deduced from the following equation: $\text{TOF} = (j \times A) \times (n \times F \times m)^{-1}$, where A represents the area of working electrode, n refers to the electron transfer number at a specific η , F stands for the Faraday constant, and m is

the mole number of metal on the surface of catalyst. Thus, an electrocatalyst with a larger TOF value demonstrates the higher intrinsic activity.

2.3.5 Faradaic Efficiency

Faradaic efficiency (FE) depicts the electron conversion efficiency for hydrogen or oxygen production. The FE value of HER or OER is the ratio of experimental value to theoretical value of H_2 or O_2 production [124, 140]. The practical amount of H_2 or O_2 production is detected through gas chromatography (GC) or the conventional water–gas displacement method, and the theoretical yield of hydrogen or oxygen is obtained via the chronoamperometric or chronopotentiometric analysis [141].

2.3.6 Electrochemically Active Surface Area

Electrochemically active surface area (ECSA) can reflect the electrocatalytic performances of HER/OER catalysts through evaluating the specific surface area and the number of active sites [19]. The ECSA is positively correlated to the double-layer capacitor (C_{dl}), which is usually obtained by analyzing CV curves of varied scanning rates in the non-faradaic region [130]. The large C_{dl} value for the catalyst indicates abundant catalytically active sites and thus presents enhanced electrocatalytic performances during the HER/OER process.

3 Formation Mechanism of the Crystal Facet

The formation of the crystal involves two steps: nucleation and growth. When the saturation of a solution exceeds a critical value, crystal nuclei are produced [142, 143]. When the size of the crystal nucleus is larger than the critical size, its Gibbs free energy changes more than the surface energy and the crystal nucleus gradually grows to form a crystal. Remarkably, the crystal eventually evolves into a polyhedral shape composed of planes with different orientations during its growth process. These planes with different orientations are called crystal facets, which can be generally expressed by a set of Miller indices $\{hkl\}$ [87]. The generation of the crystal facet needs to follow the Gibbs–Wulff theorem during the growth of the crystals [99]. As presented in Fig. 5,

the crystal facets with higher surface energies allow fast growth rates and usually occupy a small part of the surface or even disappear as the crystal grows, while the crystal planes with lower surface energies grow slowly and take up larger proportions of the surface, which constitutes the main part of the entire crystal facet [72]. Therefore, the surface energy of the crystal facet can be tailored by using organic or inorganic additives during the crystal growth process, thus achieving shape-controlled synthesis of crystals with desired crystal facets. Nowadays, with the progress of science and technology, the crystal facets of materials can be characterized and further identified through the collaborative combination of various advanced instruments including powder X-ray diffractometer (XRD), high-resolution transmission electron microscope (HR-TEM), high-angle annular dark-field scanning transmission electron microscope (HAADF-STEM), etc. Specifically, in the XRD test, a specific angle corresponds to a specific diffraction peak, which can identify theoretical crystal facets and provide the theoretical interplanar distance. HR-TEM and HAADF-STEM instruments can measure interplanar distances of crystal facets at ultra-high multiples, which is mutually verified with XRD results.

4 Various Strategies of Crystal Plane Control

4.1 Capping Agent with Crystal Plane Selectivity

As shown in Fig. 6a, capping agent can selectively attach on some specific crystal planes with higher surface energies and lower the surface energies to slow down the growth rate of the adsorbed planes, therefore expanding the percentage of the adsorbed planes (exposed planes) on the entire crystal surface [144]. Thus, the proportion of different crystal planes on the entire surface can be determined through controlling the amount of capping agent added. For instance, Yang and coauthors revealed that the anatase TiO_2 is exposed with {001} facets by increasing the concentration of fluoride ions (as the capping agent) to adjust the order of surface energy [145]. As result, the percentage of exposed {001} facets reached 47% while only 4% was obtained without fluoride ions. Subsequently, inspired by the above, anatase TiO_2 crystals with the exposure of 60%, 64%, and 89% {001} facets are produced by further optimizing the experiments [146–148]. Zhang et al. [149] realized the evolution of Cu_2O nanocrystals from

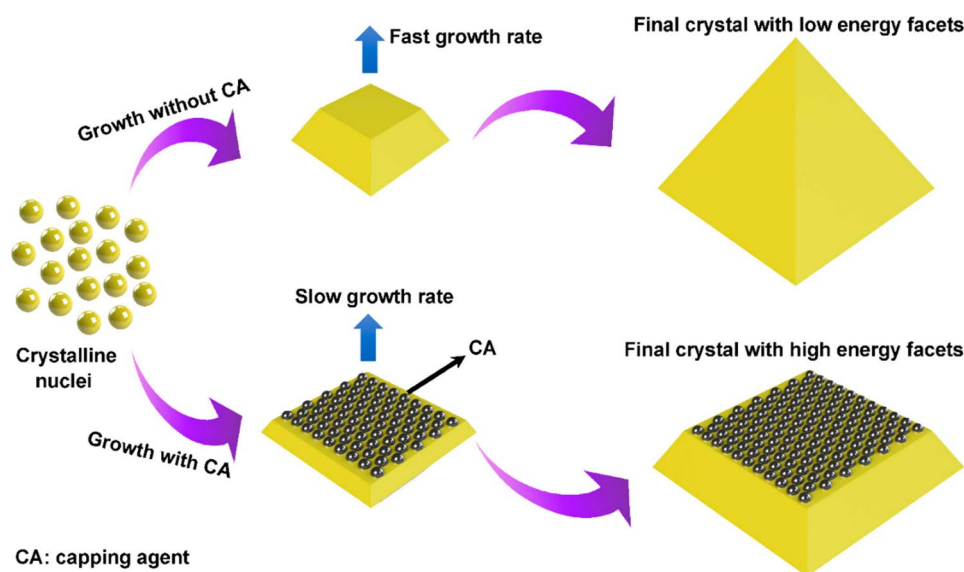


Fig. 5 Schematic diagram of organic or inorganic additive used for crystal facet engineering. Reproduced with permission [72]. Copyright 2019, American Chemical Society

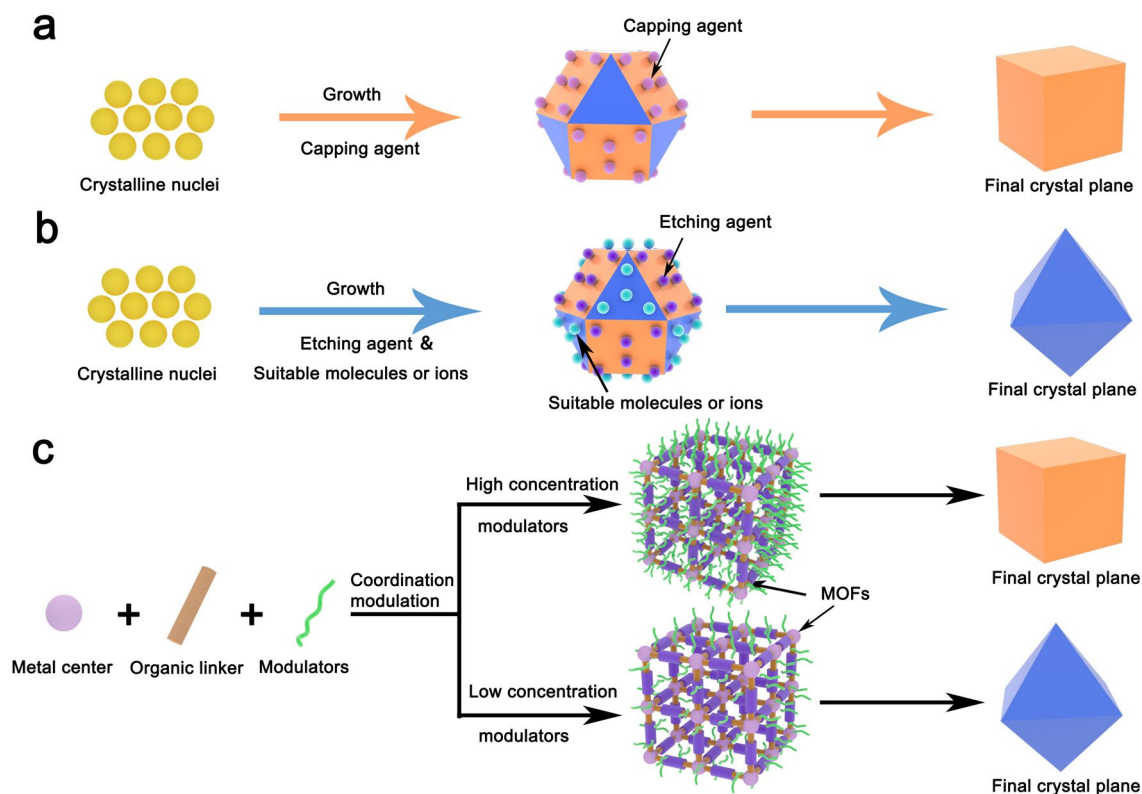


Fig. 6 Schematic illustration of crystal plane control using **a** selective capping agents, **b** selective etching agents, and **c** modulators

nanocubes to truncated nanocubes, nanocubooctahedrons, truncated nanooctahedrons, and finally nanooctahedrons through changing the amount of polyvinylpyrrolidone (PVP). Cu_2O exposed different facets during the evolution. The Cu_2O cubes with the exposure of $\{100\}$ facets can be obtained without the addition of PVP, while with the addition of PVP increased, the Cu_2O cubes eventually transform into the Cu_2O octahedrons with the exposed $\{111\}$ facets. Zeng et al. [144] found that citrate and PVP can selectively attach to surfaces of Ag nanoparticles to decelerate the grow rate, resulting in the generation of Ag octahedrons with $\{111\}$ facets and Ag nanocubes/nanobars with $\{100\}$ facets, respectively.

4.2 Etching Agent with Crystal Plane Selectivity

As mentioned above, capping agent strategy is adopted to control crystal planes during crystal formation. Yet, etching agent strategy is used to tailor crystal planes after crystal formation. Intriguingly, two strategies have a similar effect

on crystal plane control: The basic principle is all originated from the selective effect between the added reagent and the crystal plane. Etching agent strategy is a top-down route for the preparation of targeted planes. The top-down approach involves selecting certain molecules or ions that can selectively attach to the targeted planes, avoiding them being damaged from etching agent (Fig. 6b). In theory, targeted planes will be preserved and other undesirable planes will be dissolved by the etching agent. However, surface recrystallization phenomena may occur on the mother crystal facets during the etching process [99]. Besides, different planes may demonstrate diverse anticorrosion property to a specific etching reagent. Hence, it is important to choose a proper etching agent for the construction of desired facets. For instance, Pal et al. [150] proposed a simple, facile, and surfactant-free approach to prepare five types of Cu_2O nanoparticles with different shapes. The morphological evolution of Cu_2O nanoparticles can be achieved attributed to the etching agents (NaOH solution, triethylamine (TEA), and oxalic acid solution). After the etching process, NaOH-etched, TEA-etched, and oxalic acid-etched products of octahedral

Cu₂O nanoparticles exhibited the exposed {110} facets, {111} facets, and {110} as well as {200} facets, respectively. Tsai et al. [151] achieved precise etching {110} facets of Cu₂O nanocrystals by adding HCl during the growth of Cu₂O nanocrystals. Liu et al. [152] found that {001} facets of anatase TiO₂ can be selectively etched by HF and corresponding {101} facets were preserved. During the etching process, the {001} facets were slightly etched or fully etched by tuning the concentration of HF.

4.3 Coordination Modulation

The tunable of crystal planes is feasible using modulators via the coordination modulation method. Notably, the coordination modulation method to control crystal planes is currently suitable for MOFs. As displayed in Fig. 6c, the role of the coordination modulator is to control the kinetics of diverse processes (e.g., nucleation) and induce the crystal orientation growth in a specific axis, thus leading to the generation of the crystal with specific and desirable facets [153–155]. For instance, Umemura et al. [154] prepared a porous coordination framework of [Cu₃(btc)₂]_n (btc is benzene-1,3,5-tricarboxylate) assembled with btc as the organic ligand and copper(II) nitrate trihydrate as the metal source. The morphological evolution of [Cu₃(btc)₂]_n from octahedron and cuboctahedron to cube was achieved by increasing the concentration of lauric acid (as the modulator). When the concentration of modulator was low, [Cu₃(btc)₂]_n with exposed dominant {111} facets was obtained, whereas when the concentration of modulator was high, the resulting [Cu₃(btc)₂]_n exposed dominant {100} facets. Yang et al. reported that coordination modulation of MIL-125 crystals with truncated octahedral shape was realized by using butyric acid as the modulator. The as-prepared MIL-125 crystals consisted of two exposed {001} and eight {101} facets. Sikdar et al. [156] realized the morphological and dimensionality transition with diverse crystal facets through varying the concentration of dodecanoic acid (as a modulator). As-obtained hex-MOF1, rod-MOF1, and meso-MOF1 were dominated by {200} planes, {075} and {07–5} planes, and {030} planes, respectively.

5 Facet-Engineered Catalysts for HER

5.1 Noble Metal Catalysts

Noble metal catalysts, especially Pt-based nanocatalysts with optimal hydrogen absorption energy, are considered as the promising HER catalysts [157, 158]. The proportions of various crystal facets on the Pt nanocrystal surface can be regulated by changing its morphology. For instance, the cuboctahedron of the Pt nanocrystal is mainly composed of {111} facets and {100} facets, while its cube and tetrahedral are dominated by {100} facets and {111} facets, respectively [159]. As shown in Fig. 7a, Bao and co-authors proposed an in situ electrochemical reduction strategy to synthesize Pt nanosheets anchored on carbon nanotubes (Pt NSs/CNTs) with high-index {311} facets as well as low-index {200} and {111} facets during the HER process [160]. Theoretical calculations and experimental results revealed that adsorbed H₂O was served as capping agents to protect the {311} and {200} facets of Pt nanosheets. Thus, the remaining {200} facets performed as efficient active sites for H₂ recombination. As displayed in Fig. 7b, Pt NSs/CNTs exhibited excellent HER activity, requiring low η of 36 and 175 mV to achieve current densities of 10 and 50 mA cm⁻² in 1.0 M KOH, respectively. The corresponding Tafel slope is 44 mV dec⁻¹. Sun et al. [161] fabricated Pt nanodendrites (Pt NDs) with the exposure of {111} facets at the surface of activated carbon via direct electrochemical deposition. Benefiting from the exposed numerous atoms at {111} facets and high surface area, the Pt NDs showed distinguished electrocatalytic activity toward HER with a low η of 27 mV at 10 mA cm⁻², a small Tafel slope of 22.2 mV dec⁻¹, and prominent stability for more than 6 h or even 5000 CV cycles of continuous electrolysis in 0.5 M H₂SO₄ solution. Moreover, Pt NDs also display good catalytic performance within a wide pH range, producing 30–45% more hydrogen compared to that of the commercial catalyst with the same content of Pt. Raspberry-like antimony–platinum (SbPt) nanoparticles with exposed {110}, {100}, {101}, and {012} facets (Fig. 7c) were obtained by Chan et al. [162]. According to the proposed theoretical structural model, the density functional theory (DFT) results demonstrated that

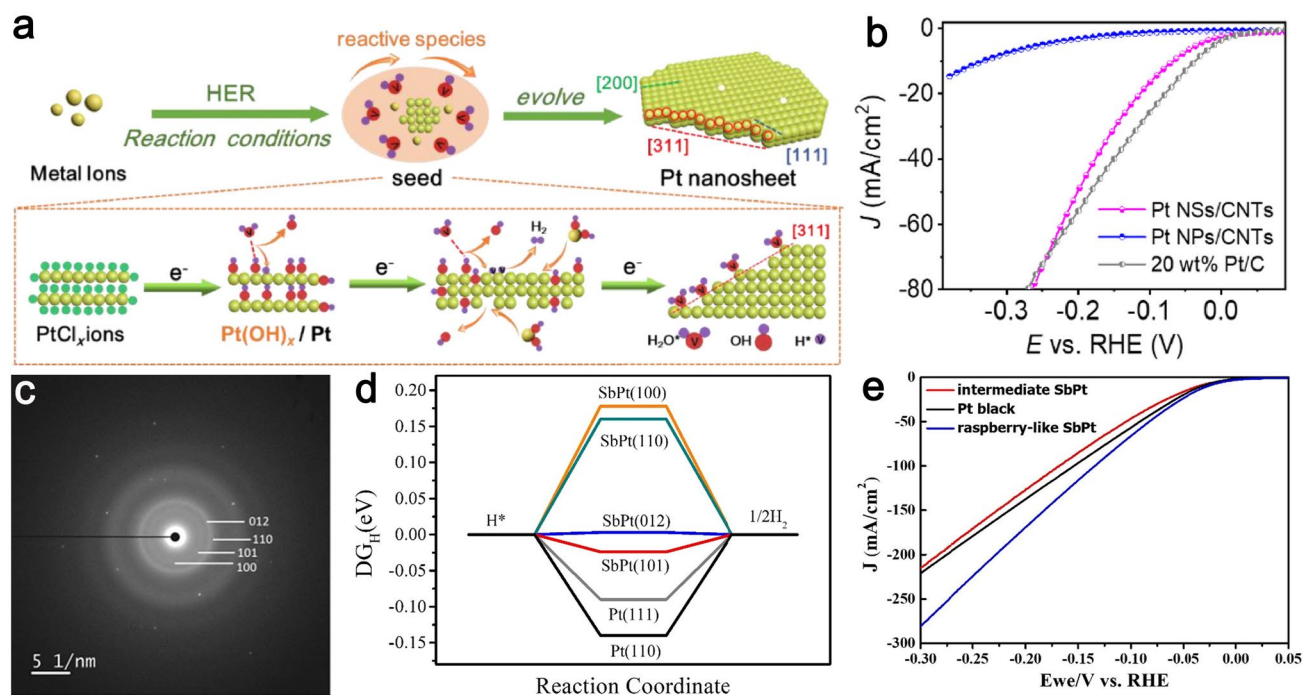


Fig. 7 **a** Schematic diagram of the formation of Pt NSs/CNTs with the exposure of {311} and {200} facets under in situ HER conditions. **b** HER polarization curves of Pt NSs/CNTs, Pt NPs/CNTs, and 20 wt% Pt/C. Reproduced with permission [160]. Copyright 2020, Elsevier B.V. and Science Press on behalf of Science Press and Dalian Institute of Chemical Physics, Chinese Academy of Sciences. **c** Indexed SAED pattern of SbPt nanoparticles. **d** HER free energy diagram for SbPt (100), (110), (012), and (101) as well as Pt (111) and (110). **e** LSV curves of intermediate SbPt, Pt black, and raspberry-like SbPt. Reproduced with permission [162]. Copyright 2020, Elsevier Inc

SbPt nanoparticles featured different adsorption energies for {101} and {012} facets, which were smaller compared to those of the classic Pt crystal planes such as {111} facets and {110} facets (Fig. 7d). The crystal facets of SbPt nanoparticles can be moderated for HER pathway in the chemisorption of H*, resulting in improved HER catalytic activity. As a result, the raspberry-like SbPt nanoparticles with highly active {110}, {100}, {101}, and {012} facets exhibited superior HER activity with a small Tafel slope of 50.5 mV dec⁻¹ and a small η of 81 mV to reach 10 mA cm⁻² in 0.5 M H₂SO₄ solution (Fig. 7e).

Apart from Pt-based electrocatalysts, other precious metal-based materials (e.g., Ag, Pd, etc.) are also promising electrocatalytic materials for HER. For example, Kuo et al. [163] designed and synthesized {100} facets-dominated silver nanocubes (Ag NCs) and {111} facets-dominated silver nanooctahedra (Ag NOs) through the polyol reaction. The Ag NCs and Ag NOs possessed the light-harvesting capabilities for the plasmon-enhanced HER electrochemical system. Plasmonic Ag NOs with exposed {111} facets showed better HER catalytic performance than that of Ag NCs with

exposed {100} facets in the mixture of 0.5 M H₂SO₄ and 1.0 M C₂H₅OH. The DFT calculation revealed that adsorption energy of the surfaces originated from Ag {111} facets is lower compared to that of Ag {100} facets, demonstrating that hydrogen could be easily desorbed on Ag {111} facets during the HER process. Xu et al. [164] proposed a bottom-up synthetic strategy to prepare ultrathin palladium nanosheets (Pd NSs). The key to prepare ultrathin Pd NSs with different exposed facets is to utilize the amphiphilic function of surfactants. Functional groups (carboxyl, pyridyl, quaternary ammonium, etc.) and halide counter ions of surfactants could be attached to different Pd planes, resulting in ultrathin Pd NSs with exposed {100}, {110}, and {111} facets, respectively. The surface facet-dependent HER catalytic properties of ultrathin Pd NSs were systematically explored in 0.5 M H₂SO₄ solution. The results evidenced that the electrocatalytic performances of three exposed facets toward HER followed the order of {111} < {110} < {100}. Pd NSs {100} displayed a η of 67 mV at 10 mA cm⁻² which was much smaller than those of Pd NSs {111} (160 mV) and Pd NSs {110} (91 mV). The better HER catalytic activity

of Pd NSs {100} might be attributed to the optimal balance between adsorption/desorption of H on the {100} facets of Pd NSs during HER process.

5.2 Metal Phosphide Catalysts

Owing to the exceptionally high activity and chemical stability, metal phosphide catalysts are regarded as promising candidates to replace Pt counterparts for HER [165–167]. Yan et al. [168] adopted a facile method to synthesize edge-rich nickel phosphide nanosheet arrays on nickel foam (Ni₂P NSs-NF). On account of abundant active edges, the Ni₂P NSs-NF showed superior catalytic activity toward HER in both acidic and alkaline media and required a low η of 67 mV in the acidic media (0.5 M H₂SO₄) and 89 mV in the alkaline media (1.0 M KOH) to generate 10 mA cm⁻² with a small Tafel slope of 57 and 82 mV dec⁻¹, respectively. The Ni₂P NSs-NF exhibited exceptionally high activity toward HER because the free energy of hydrogen adsorption (ΔG_{H}) on {211} crystal planes was close to zero (– 0.03 V). In another work, {001} facets-dominated hollow Ni₂P nanoparticles were synthesized by Popczun et al. [167]. The exposed {001} facets of Ni₂P nanoparticles have been predicted to possess the highest catalytic performance toward HER according to the previous report [169]. As expected, the Ni₂P nanoparticles on the glassy carbon produced 20 and 100 mA cm⁻² at a small η of 130 and 180 mV, respectively, and demonstrated a low Tafel slope of 30 mV dec⁻¹ in 0.5 M H₂SO₄. Wang et al. fabricated flower-like Ni₅P₄ microballs with the exposure of high-energy {001} facets. The flower-like Ni₅P₄ microballs featured hierarchical structure and high-energy {001} facets, which is beneficial to accelerate electron transfer and boost the inherent catalytic activity. The flower-like Ni₅P₄ microballs achieved outstanding HER performances with a low Tafel slope of 48 mV dec⁻¹ and a small η of 35.4 mV at 10 mA cm² in 0.5 M H₂SO₄, as well as a small Tafel slope of 56 mV dec⁻¹ and a small η of 47 mV at 10 mA cm² in 1.0 M KOH, respectively.

Bimetallic phosphides have been explored as the effective electrocatalysts for HER attributing to high conductivity, abundant active sites and the cooperative effects of bimetal [47, 48, 107]. For example, Ma et al. [170] constructed hetero-structured Ni–Co phosphide nanowires on the Ni–Co alloy foam (Ni₅P₄–Co₂P/NCF) through a simple and versatile method. The rich heterointerfaces of

the highly active {303} crystal planes between Co₂P and Ni₅P₄ endowed Ni₅P₄–Co₂P/NCF with the high intrinsic catalytic property toward HER, requiring a η of 21, 92, and 267 mV to reach 10, 100, and 1000 mA cm⁻², respectively (Fig. 8a). The as-prepared Ni₅P₄–Co₂P/NCF showed a low Tafel slope of 23 mV dec⁻¹ and good stability over 100 h at 250 mA cm⁻² in 1.0 M KOH (Fig. 8b). According to the proposed model of phosphides (Fig. 8c), the DFT calculations revealed the electronic state of the {303} crystal planes of Ni₅P₄–Co₂P/NCF crossed the Fermi level (0 V) and demonstrated its metallic property beneficial to accelerate electron transfer rate (Fig. 8d). As illustrated in Fig. 8e, the Ni₅P₄–Co₂P {303} model exhibited a higher electronic density around the Fermi level than those of Co₂P {303}, Co₂P {113}, and Ni₅P₄, resulting in favorable adsorption of free radicals during the HER process for the Ni₅P₄–Co₂P {303} model. Yu's [171] group synthesized the CoP/Ni₂P hybrid catalysts via the solvothermal synthesis with post-phosphorization treatment. The CoP/Ni₂P hybrid catalysts presented distinguished catalytic activity toward HER with a low η of 36, 54, and 57 mV at 10 mA cm⁻², respectively, and a small Tafel slope of 41.2, 47.3, and 58.6 mV dec⁻¹ in 0.5 M H₂SO₄, 1.0 M phosphate buffer solution (PBS) and 1.0 M KOH, respectively. The DFT results confirmed that the superiority of the CoP/Ni₂P hybrid was contributed to the strong synergistic effects originated from the CoP {101} and Ni₂P {001} planes, thus boosting the overall HER activity with an optimal ΔG_{H} close to 0.08 eV.

5.3 Metal Chalcogenide Catalysts

Metal chalcogenide-containing metal sulfide and metal selenide are promising electrocatalysts for HER attributed to their earth abundance, high intrinsic catalytic activity, and abundant active sites [40, 41, 92, 110, 172, 173]. Taking the metal sulfide catalysts as an example, Liang et al. [82] presented a hydrothermal method to controllably prepared two NiS₂ nanocrystals with exposed {111} and {100} planes, respectively (Fig. 9a–f). Based on DFT calculations, the surface energies of {111} and {100} planes were evaluated, which may offer a reasonable explanation for the difference in catalytic activity. The {111} planes of NiS₂ exhibited higher surface energy compared to those of the {100} planes, indicating enhanced HER catalytic activity. Moreover, according to the proposed models

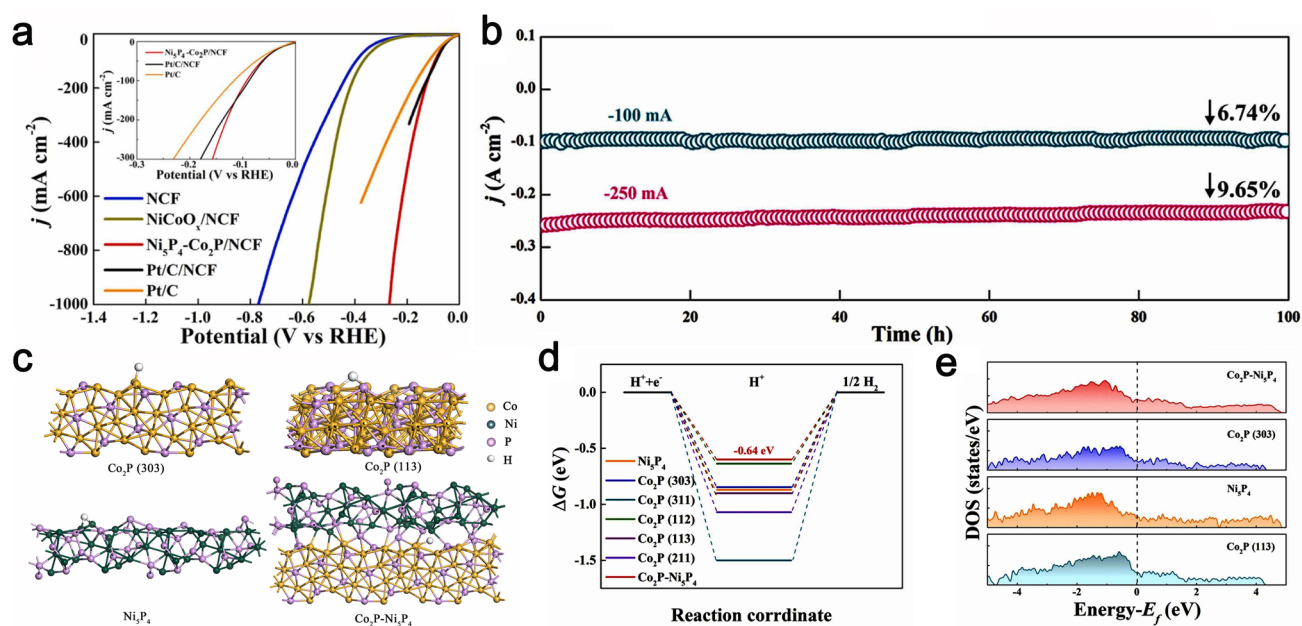


Fig. 8 **a** HER polarization curves of Pt/C, Pt/C/NCF, NCF, NiCoO_x/NCF, and Ni₃P₄-Co₂P/NCF. **b** Chronoamperometry measurements of Ni₃P₄-Co₂P/NCF maintained at j_{100} and j_{250} for 100 h. **c** Theoretical computational models of Co₂P (303), Co₂P (311), Co₂P (112), Co₂P (113), and Co₂P (211). **d** The HER free energy diagram for Co₂P (303), Co₂P (311), Co₂P (112), Co₂P (113), Co₂P (211), Ni₃P₄, and Co₂P-Ni₃P₄. **e** Density of states corresponding to theoretical computational models. Reproduced with permission [170]. Copyright 2022, Elsevier Ltd

(Fig. 9g-j), the adsorption energies of hydrogen atom on Ni-terminated and S-terminated {111} planes were calculated to be 10.67 and 2.42 eV, respectively, which were lower than those of the {100} planes (13.02 and 7.67 eV). The DFT results evidenced that {111} planes of NiS₂ possessed stronger H adsorption capacity and better HER performance than {100} planes. {111} planes of NiS₂ required an η of 138 mV to generate 10 mA cm⁻² in 1.0 M KOH, while a much higher η of 302 mV was required for {100} planes of NiS₂ (Fig. 9k). The {111} planes exhibited a Tafel slope of 139 mV dec⁻¹, which was smaller than that of {100} planes (181 mV dec⁻¹). Miao and co-workers [110] obtained mesoporous FeS₂ via a facile synthetic protocol. The mesoporous structure and exposed {210} facets endowed FeS₂ with a high specific surface area of 128 m² g⁻¹ and abundant accessible active sites, which could be beneficial for HER kinetics. Accordingly, the FeS₂ catalyst achieved superior HER properties with a small Tafel slope of 78 mV dec⁻¹, a low η of 96 mV at 10 mA cm⁻², and long durability in 0.1 M KOH. DFT calculations confirmed that the abundant {210} facets of mesoporous FeS₂ accounted for high HER performance and the low activation barrier.

Inspired by the periodic table where both S and Se are in group VIA, metal selenides were also expected as the potential electrocatalysts for HER [33, 100]. Zhong and coauthors developed a facile solid synthesis strategy for the preparation of RhSe₂ with multiple facets of {200}, {210}, {211}, {220}, and {311} [174]. DFT studies revealed that the ΔG_{H} of RhSe₂ with multiple crystal facets was close to zero, suggesting abundant active sites in the RhSe₂ catalyst. In acidic solution, low-coordinated Rh sites served as real active sites, which might allow the modified Kubas-mediated HER pathway to happen. Thus, the Kubas complexes were employed to overcome the high reaction barriers derived from the surface H diffusion (Tafel Reaction) as well as the proton–electron combination (Heyrovsky reaction) to produce hydrogen. In contrast, Se acted as real active sites and became more active in alkaline solution. Hydrogen evolution could proceed through the Volmer reaction termed rate-limiting step. Accordingly, the as-obtained RhSe₂ with multiple active facets demonstrated the superior electrocatalytic property for HER with a small Tafel slope of 39 mV dec⁻¹ and a low η of 49.9 mV at 10 mA cm⁻² in 0.5 M H₂SO₄ as well as a η of 81.6 mV at 10 mA cm⁻² and a Tafel slope of 86 mV dec⁻¹ in 1.0 M KOH. In another work, Xi's group

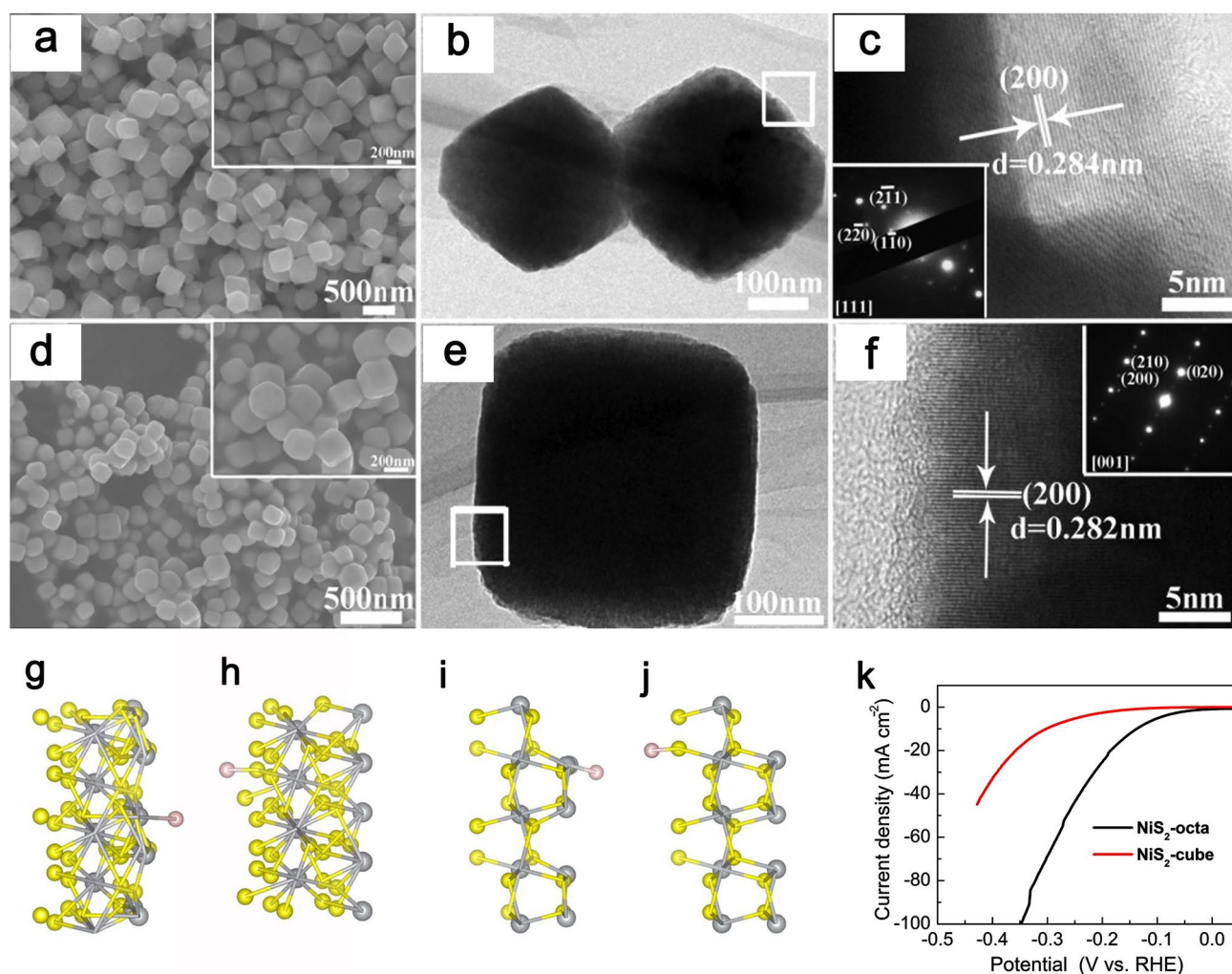


Fig. 9 a–c SEM and TEM images of NiS₂-octa. d–f SEM and TEM images of NiS₂-cube. Views of the H absorbed on the g Ni-terminated (111) surface and h S-terminated (111) surface. Views of the H absorbed on the i Ni-terminated (100) surface and j S-terminated (100) surface. k HER polarization curves of NiS₂-octa and NiS₂-cube. Reproduced with permission [82]. Copyright 2019, Elsevier Inc

successfully designed ultrathin metallic CuFeS₂ nanosheets (CuFeS₂ NSs) with the exposure of high-index {0–224} facets [175]. {112} facets and {200} facets are observed in Fig. 10a, wherein the angle between {112} facets and {200} facets was calculated to be 54.9° (closed to the theoretical value of 55°), indicating the existence of the exposed high-index {0–224} facets. As illustrated in Fig. 10b and c, the CuFeS₂ NSs with the exposed high-index {0–224} facets achieved excellent HER performances with a small η of 88.7 mV (10 mA cm⁻²) and a low Tafel slope (47 mV dec⁻¹) superior to those of CuFeS₂-b with low-index {112} facets, bulk chalcopyrite, CuS NSs, and FeS₂ NSs in 0.5 M H₂SO₄. To investigate the origin of enhanced HER catalytic

activity, the HR-TEM test, XAS test, and DFT calculations of CuFeS₂ NSs are performed, respectively. The HR-TEM results showed that {112} facets and {200} facets were still well preserved after the stability test, suggesting the existence of high-index {0–224} facets. As displayed in Fig. 10d, e, the coordination number of Cu and the $R_{\text{Cu-S}}$ has hardly changed, while the coordination number of Fe decreased from 4.0 to 2.6. These results revealed that S²⁻ in the Fe–S site might be moved to the surface of the CuFeS₂ NSs as active sites, leading to the decreased coordination number of Fe. Moreover, as presented in Fig. 10f, DFT results demonstrated the calculated ΔG_{H} on the high-index {0–224} facets is closest to zero compared to those of {112} facets

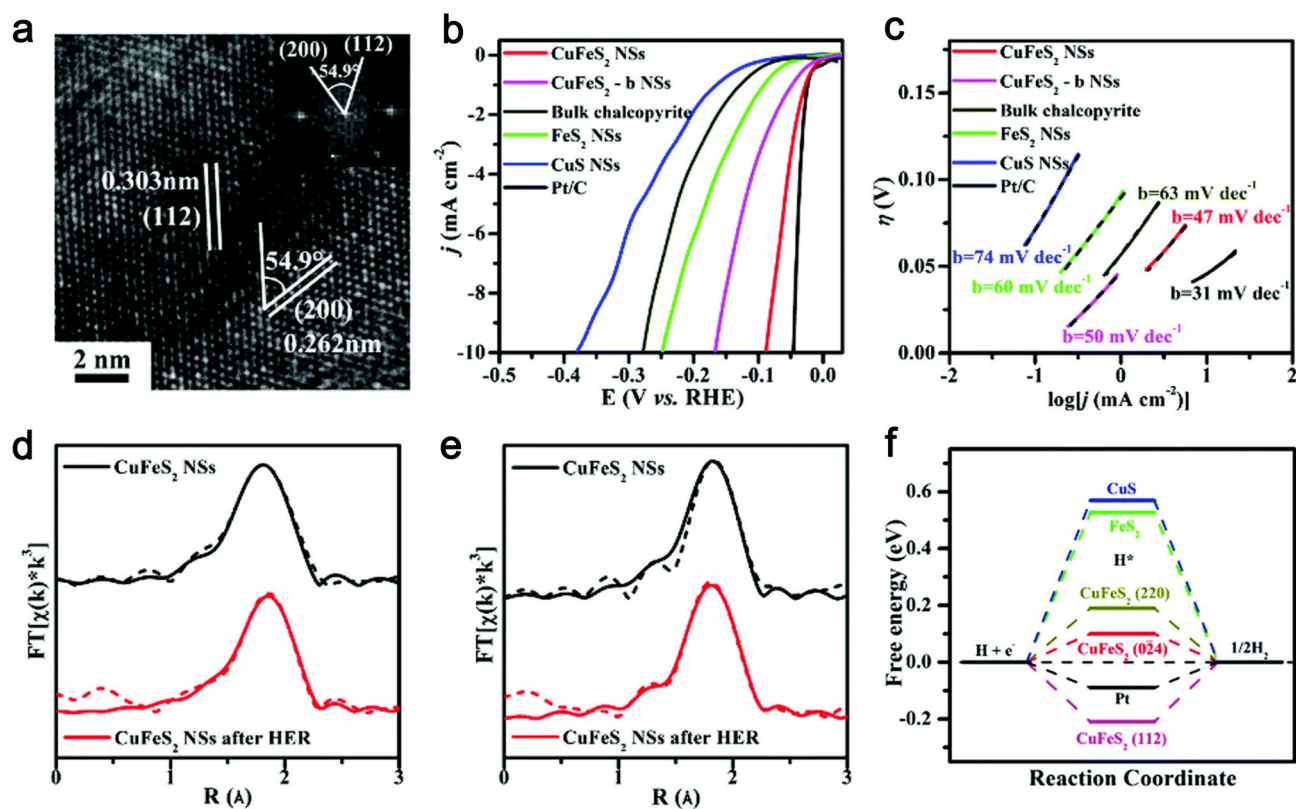


Fig. 10 **a** HR-TEM image of CuFeS₂ NSs. **b** HER polarization curves of CuFeS₂ NSs, CuFeS₂-b NSs, bulk chalcopyrite, CuS NSs, FeS₂ NSs, and Pt/C. **d** Cu K-edge and **e** Fe K-edge before and after HER measurements, respectively. **f** The HER free energy diagram for three materials and Pt reference. Reproduced with permission [175]. Copyright 2017, Royal Society of Chemistry

and {200} facets, which further evidencing that high-index {0–224} facets feature abundant catalytic active sites for HER. Overall, the major cause of highly improved HER catalytic activity for the CuFeS₂ NSs is related to the excess S²⁻ active sites on the exposed high-index {0–4} facets and the ultrathin nanosheet structure.

5.4 Other Metal-Based Catalysts

In addition to the above-mentioned catalysts, other transition metal-based compounds including metal carbides, metal nitrides, and metal oxides were also employed as high-performance HER catalysts. Metal carbides are highlighted by virtue of their high electronic conductivity, high catalytic activity and high stability toward HER [176, 177]. Mu's group reported a "micro-cutting-fragmentation" technique to prepare carbon-cohered tantalum carbide nanocrystals (TaC NCs@C) with the exposure of the dominant high-index

{222} facets by varying the reaction temperature (Fig. 11a) [94]. According to the calculated model, theoretical calculations unveiled the potential HER activity of {222} facets in TaC. Other low-index facets such as {311}, {220}, {200}, and {111} of TaC exhibited a ΔG_{H} value of -0.53, -0.56, -0.73, and -0.67 eV, respectively, which was all smaller than the value of the {222} plane (-0.23 eV), suggesting more active sites on {222} planes toward HER (Fig. 11b-c). The TaC NCs@C with exposed {222} planes produced at 950 °C showed a Tafel slope of 143 mV dec⁻¹, reached 10 mA cm⁻² at a η of 146 mV, and exhibited good stability in N₂-saturated 0.5 M H₂SO₄ (Fig. 11d). Wang's group constructed double-deck carbon-enveloped V₈C₇ networks with exposed highly active {110} planes supported on nickel foam (V₈C₇@GC NSs/NF) [178]. The V₈C₇@GC NSs/NF featured three exposed facets of typical {100}, {110}, and {111}. DFT results demonstrated that exposed {110} facets exhibited smaller ΔG_{H} value compared to those of {100} and {111} facets, indicating the enhanced intrinsic catalytic

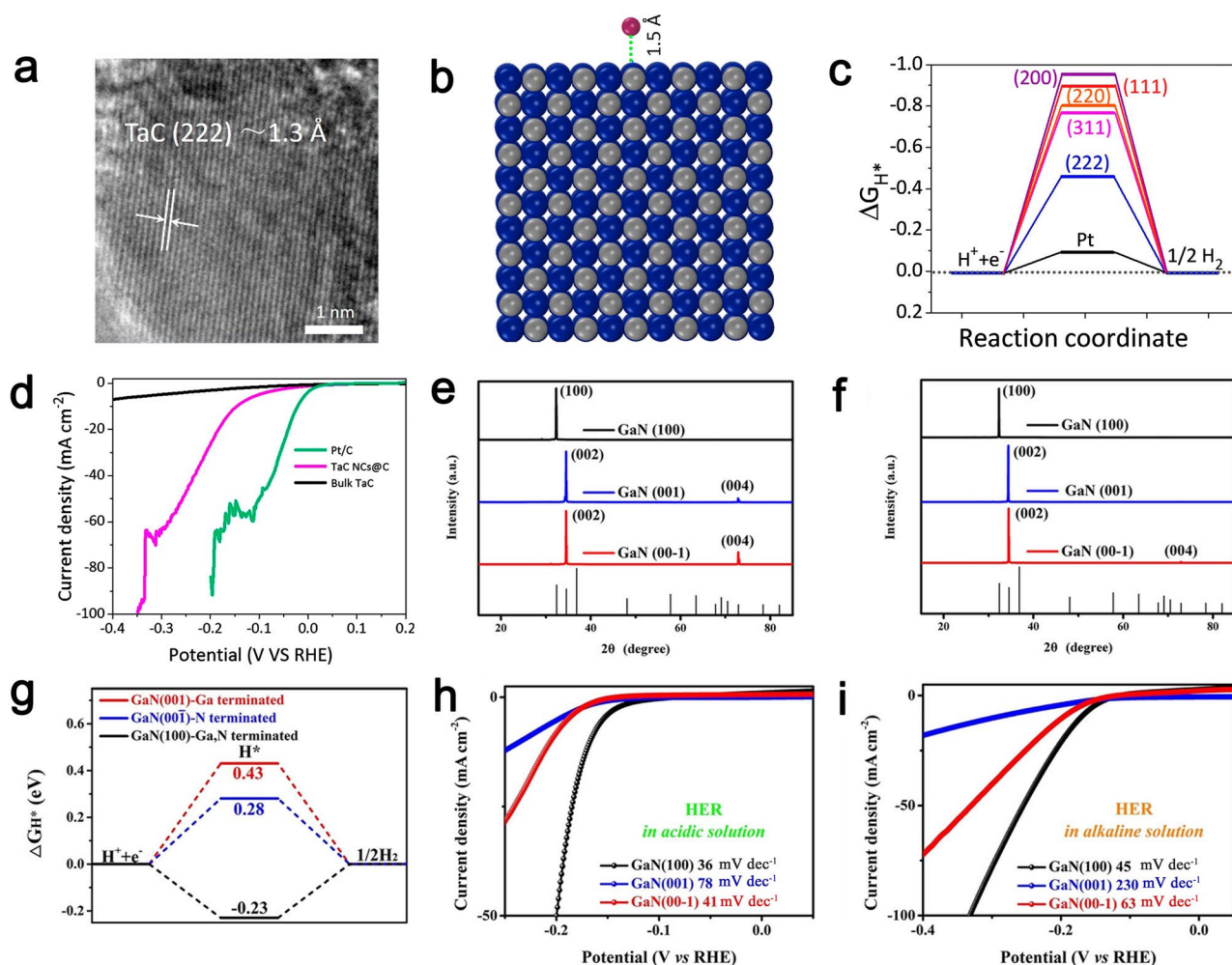


Fig. 11 **a** HR-TEM image of TaC NCs@C. **b** Theoretical absorption model of H^* atom on Miller index facets with an absorption distance of 1.5 Å. **c** DFT-calculated free energy diagram with different adsorption sites of H^* at equilibrium potential for high-index (222) facet, relatively low-index (111), (200), (220), and (311) facets as well as Pt reference. **d** LSV curves of Pt/C, bulk TaC, and TaC NCs@C for HER. Reproduced with permission [94]. Copyright 2017, Elsevier Ltd. XRD patterns of GaN {001}, GaN {00-1}, and GaN {100} after HER durability tests in **e** acidic and **f** alkaline media. **g** DFT-simulated adsorption energies of H^* on GaN (001), GaN (00-1), and GaN (100). HER polarization curves of GaN (001), GaN (00-1), and GaN (100) in **h** acidic and **i** alkaline solution. Reproduced with permission [73]. Copyright 2019, Wiley-VCH Verlag GmbH&Co

activity of {110} facets for HER. Therefore, the V_8C_7 @GC NSs/NF with exposure of highly active {110} facets achieved distinguished catalytic activity toward HER with low η of 47, 77, and 38 mV at 10 mA cm^{-2} along with small Tafel slopes of 44, 64, and 34.5 mV dec^{-1} in 1.0 M KOH, 0.1 M PBS, and 0.5 M H_2SO_4 , respectively.

Metal nitrides have attracted great attention on account of their unique physicochemical properties including high electronic conductivity, high chemical stability, and high electrocatalytic activity toward HER [179–181]. Xiao et al. [182] developed a facile CVD process to synthesis

the face-centered cubic (FCC) 2D single-crystal TiN (FCC TiN) with exposed {111} facets. The FCC TiN exhibited a η of 210 mV at 10 mA cm^{-2} and a Tafel slope of 67 mV dec^{-1} toward HER in 0.5 M H_2SO_4 . The major reason for the good HER activity was related to 2D single-crystal structure and exposed {111} facets. GaN crystals are considered as the ideal model for anisotropically exploring the reactive facets of electrocatalysts. Thus, Hu et al. [73] developed three GaN crystals with plane of {001}, {00-1}, and {100}, respectively. XRD patterns of the GaN crystal catalysts after HER durability tests in acidic and alkaline media are observed

from Fig. 11e, f. Three GaN crystals with corresponding main crystal planes were consistent with the XRD results of the simulated GaN crystal catalysts, indicating distinguished chemical stability of GaN single-crystalline catalysts. The HER activity of corresponding three planes was theoretically and experimentally investigated. DFT calculations proved that the ΔG_{H} of exposed {100} plane was lower than those of {001} and {00-1} planes, demonstrating higher HER catalytic activity for {100} plane (Fig. 11g and Table 1). The electrochemical results also presented that the exposed reactive {100} planes required a η of 168 and 171 mV to produce a current density of 10 mA cm^{-2} in 0.5 M H_2SO_4 and 1.0 M KOH, respectively, which are superior to those of {001} (234 and 296 mV) and {00-1} planes (205 and 197 mV) at the same current density (Fig. 11h, i). The Tafel slope of {100} planes was approximately 36 mV dec^{-1} in acidic solution and 45 mV dec^{-1} in alkaline solution, which was smaller compared to the corresponding value of {001} planes (78 and 230 mV dec^{-1}) and {00-1} planes (41 and 63 mV dec^{-1}).

Benefitting from low cost, earth abundance as well structural and compositional diversity, metal oxides as the promising HER electrocatalysts have been attracted increasingly attention [183, 184]. Han and co-workers proposed the facile

solvothermal and hydrothermal methods to fabricate three kinds of Co_3O_4 nanocube ($\text{Co}_3\text{O}_4\text{-NC}$) enclosed by {100} crystal planes, Co_3O_4 nanosheet ($\text{Co}_3\text{O}_4\text{-NS}$) bounded by {110} crystal planes, and Co_3O_4 nanoplate ($\text{Co}_3\text{O}_4\text{-NP}$) dominated by {111} crystal planes, respectively (Fig. 12a-i) [185]. The HER catalytic performances of three Co_3O_4 catalysts were measured in 0.1 M KOH electrolyte. The $\text{Co}_3\text{O}_4\text{-NS}$ exhibited better HER catalytic activity in comparison with those of $\text{Co}_3\text{O}_4\text{-NC}$ and $\text{Co}_3\text{O}_4\text{-NS}$, demonstrating that the HER catalytic properties of three exposed planes followed the order of {100} < {111} < {110} (Fig. 12j). As shown in Fig. 12k, the difference among the corresponding values of Tafel slopes was relatively small. The higher HER activity of $\text{Co}_3\text{O}_4\text{-NS}$ might be accredited to higher electroconductivity and higher content of Co^{3+} ions on the surface of $\text{Co}_3\text{O}_4\text{-NS}$.

6 Facet-Engineered Catalysts for OER

6.1 Noble Metal Catalysts

Noble metal-based catalysts, especially Ru- and Ir-based nanomaterials, are recognized as the most promising electrocatalysts toward OER attributing to their high intrinsic

Table 1 Comparisons of HER/OER intrinsic properties according to some electrocatalysts depending on their facets

HER/OER/OWS electrocatalysts	Dominant facets	Hydrogen adsorption free energy (ΔG_{H} , eV)	Theoretical overpotential (η , V)	References
GaN	{100}	-0.23	/	[73]
GaN	{00-1}	0.28	/	
GaN	{001}	0.43	/	
Pd@Ir TOH	{331}	/	0.73	[191]
Pd@Ir cube	{100}	/	0.99	
Pd@Ir oct	{111}	/	1.47	
$\alpha\text{-Fe}_2\text{O}_3$	{012}-O	/	0.34	[70]
$\alpha\text{-Fe}_2\text{O}_3$	{012}	/	0.57	
$\alpha\text{-Fe}_2\text{O}_3$	{104}	/	0.95	
$\alpha\text{-Fe}_2\text{O}_3$	{110}	/	1.55	
Co_3O_4 nanooctahedron	{111}	0.166	0.72	[221]
Co_3O_4 nanosheet	{112}	0.266	0.78	
Co_3O_4 nanobelt	{110}	0.291	1.04	
Co_3O_4 nanocube	{001}	0.419	1.12	
NiCo_2O_4 nanosheet	{110}	0.15	0.65	[223]
NiCo_2O_4 octahedron	{111}	0.36	0.71	
NiCo_2O_4 -truncated octahedron	{100}	0.62	0.91	
	{111}	0.36	0.71	



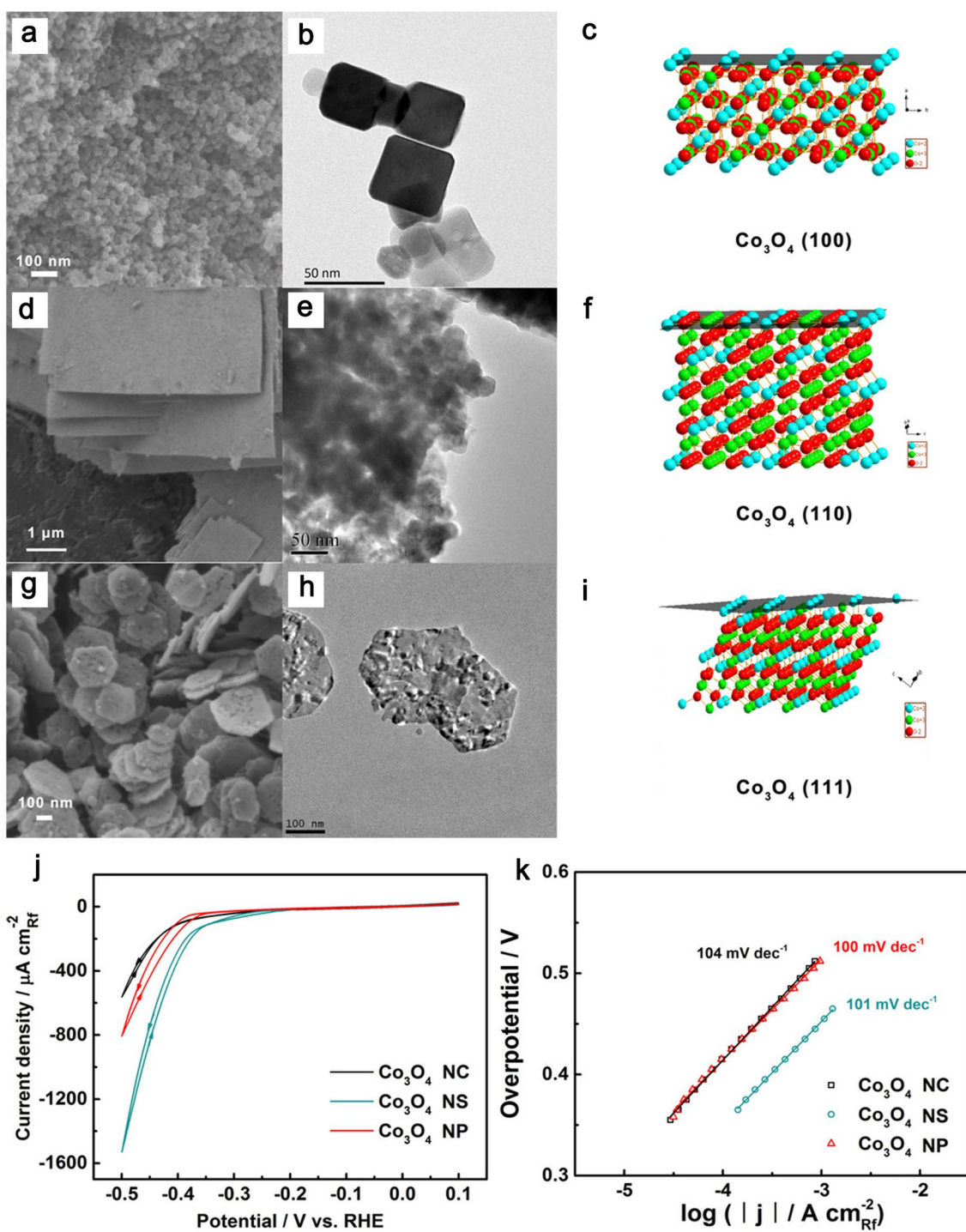


Fig. 12 **a**, **d**, and **g** SEM images, **b**, **e**, and **h** TEM images, and **c**, **f**, and **i** structure models of Co_3O_4 -NC, Co_3O_4 -NS, and Co_3O_4 -NP, respectively. **j** LSV curves of Co_3O_4 -NC, Co_3O_4 -NS, and Co_3O_4 for HER. **k** Tafel plots derived from panel j. Reproduced with permission [185]. Copyright 2018, Wiley-VCH Verlag GmbH & Co. KGaA, Weinheim

catalytic activity [26, 186–190]. For example, Xue et al. [191] constructed Pd@Ir core-shell nanostructures with diverse shapes of cubes (cube), octahedron (oct), and trioctahedron (TOH) via a conformal deposition method. The Pd@Ir cube, Pd@Ir oct, and Pd@Ir TOH were dominated by exposed Ir {100}, Ir {111}, and high-indexed Ir {331} facets, respectively (Fig. 13a–c). According to the DFT calculation results, Pd@Ir TOH enclosed by high-indexed {331} facets indicated the highest uphill energy barriers named RDS for the overall OER, which is lower than those of the Pd@Ir cube with exposed {100} facets and the Pd@Ir oct with exposed {111} facets, demonstrating an outstanding OER behavior for the Pd@Ir TOH (Fig. 13d and Table 1). The standard free energy difference ($\Delta G_{\text{O}} - \Delta G_{\text{OH}}$) was performed to further evaluate OER performance. As a result, the value of $\Delta G_{\text{O}} - \Delta G_{\text{OH}}$ of exposed {331} facets derived from the Pd@Ir TOH was calculated to be about 1.60 eV, which was higher than those of exposed {100} facets of the Pd@Ir cube and exposed {111} facets of the Pd@Ir oct, confirming the better OER

catalytic activity of exposed {331} facets in the Pd@Ir TOH (Fig. 13e). The electrochemical results in HClO_4 aqueous solution also evidenced that the Pd@Ir TOH with the exposure of high-indexed {331} facets exhibited good OER properties with a Tafel slope of 84.9 mV dec^{-1} and a η of 300 mV, which were lower than the corresponding value of Pd@Ir cubes (311.5 mV , 97.8 mV dec^{-1}), Pd@Ir oct (356 mV , 110 mV dec^{-1}), and commercial Ir/C (370 mV , $111.7 \text{ mV dec}^{-1}$) (Fig. 13f). Zhang et al. [192] explored a series of $\text{Ag}_{2-x}\text{O}/\text{FTO}-i$ electrodes (i stands for the current density during the electrodeposition) via galvanostatic electrocrystallization. The optimized $\text{Ag}_{2-x}\text{O}/\text{FTO}-1$ electrode enclosed by dominated {111} facets presented good catalytic activity toward OER with a Tafel slope of 47 mV dec^{-1} and a η of 417 mV at 10 mA cm^{-2} and good stability over 10 h in $0.1 \text{ M K}_2\text{B}_4\text{O}_7$. The high OER activity of $\text{Ag}_{2-x}\text{O}/\text{FTO}-1$ is on account of larger exposed high-activity {111} facets and more exposed $\text{Ag}^+/\text{Ag}^{2+}$ ions.

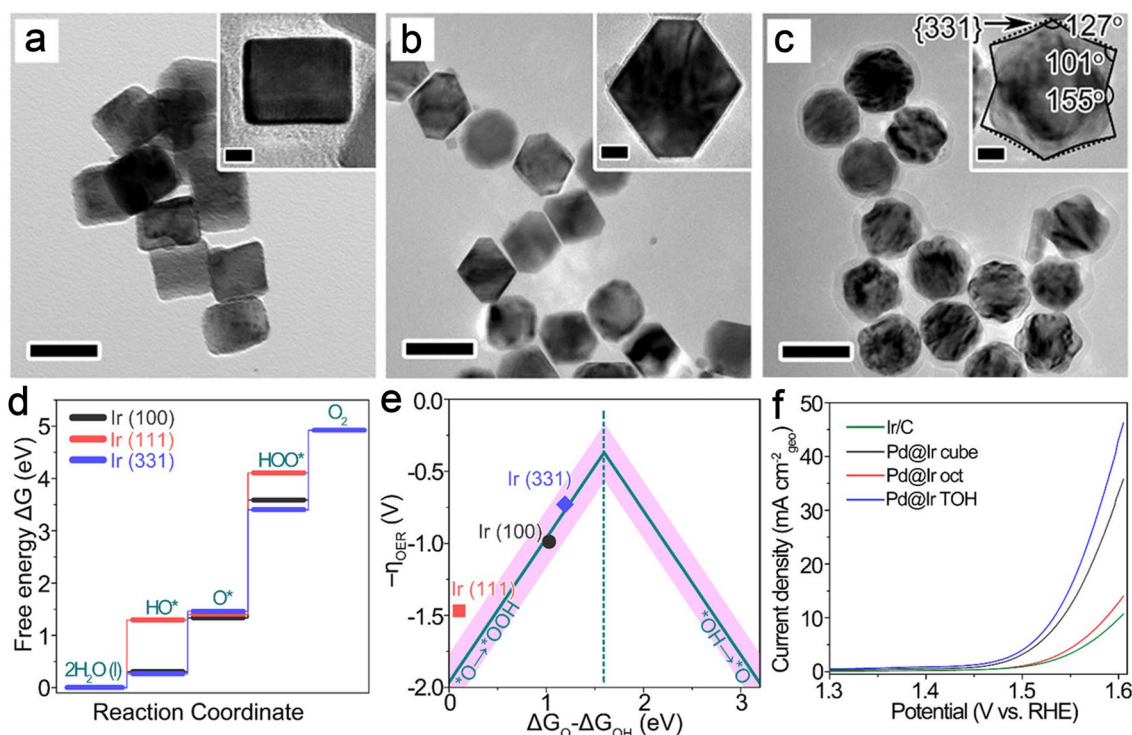


Fig. 13 TEM images of **a** Pd@Ir cube, **b** Pd@Ir oct, and **c** Pd@Ir TOH (scale bar: 50 nm). **d** Free energy diagram of Ir (100) facets, Ir (111) facets, and Ir (331) facets, respectively. **e** Simulated η against the standard free energy of $\Delta G_{\text{O}} - \Delta G_{\text{OH}}$ on Ir (100), Ir (111), and Ir (331) facets. **f** OER polarization curves of Ir/C, Pd@Ir cube, Pd@Ir oct, and Pd@Ir TOH. Reproduced with permission [191]. Copyright 2021, American Chemical Society

6.2 Metal Oxide Catalysts

A strategy known as selective etching of low-active crystal facets with retention of highly reactive crystal facets has shown to be effective in improving the OER intrinsic catalytic activity. Wu et al. [70] prepared three binary hematites ($\alpha\text{-Fe}_2\text{O}_3$) enclosed by $\{104\}$, $\{110\}$, and $\{012\}$ -O facets through the conventional solvothermal and hydrothermal methods as well as unconventional acid-etching strategy, respectively (Fig. 14a, b). The $\alpha\text{-Fe}_2\text{O}_3$ was treated by HCl solution to produce $\{012\}$ -O facets, which could be evidenced from the HR-TEM image in Fig. 14c. Subsequently, the acid-etched $\alpha\text{-Fe}_2\text{O}_3$ was treated with NaBH_4 solution

to yield the $\{012\}$ facets. In order to reveal the local environment, Fe K-edge (X-ray adsorption near edge structure) XANES spectra of $\alpha\text{-Fe}_2\text{O}_3$ with $\{012\}$ -O facets were performed using the XAS. As depicted in Fig. 14d, $\alpha\text{-Fe}_2\text{O}_3$ with $\{012\}$ -O facets demonstrated the lower intensity in terms of pre-edge peak at around 7114 eV. Besides, the corresponding Fourier transforms (FT) of extended X-ray absorption fine structure (EXAFS) were conducted to plot and fit intending to elucidate the local atomic and electronic structure (Fig. 14e). The XANES results illustrated that $\alpha\text{-Fe}_2\text{O}_3$ with $\{012\}$ -O facets possessed a higher coordination number (close to seven) of Fe–O, which reduces the e_g occupancy in the highly covalent Fe orbital and further

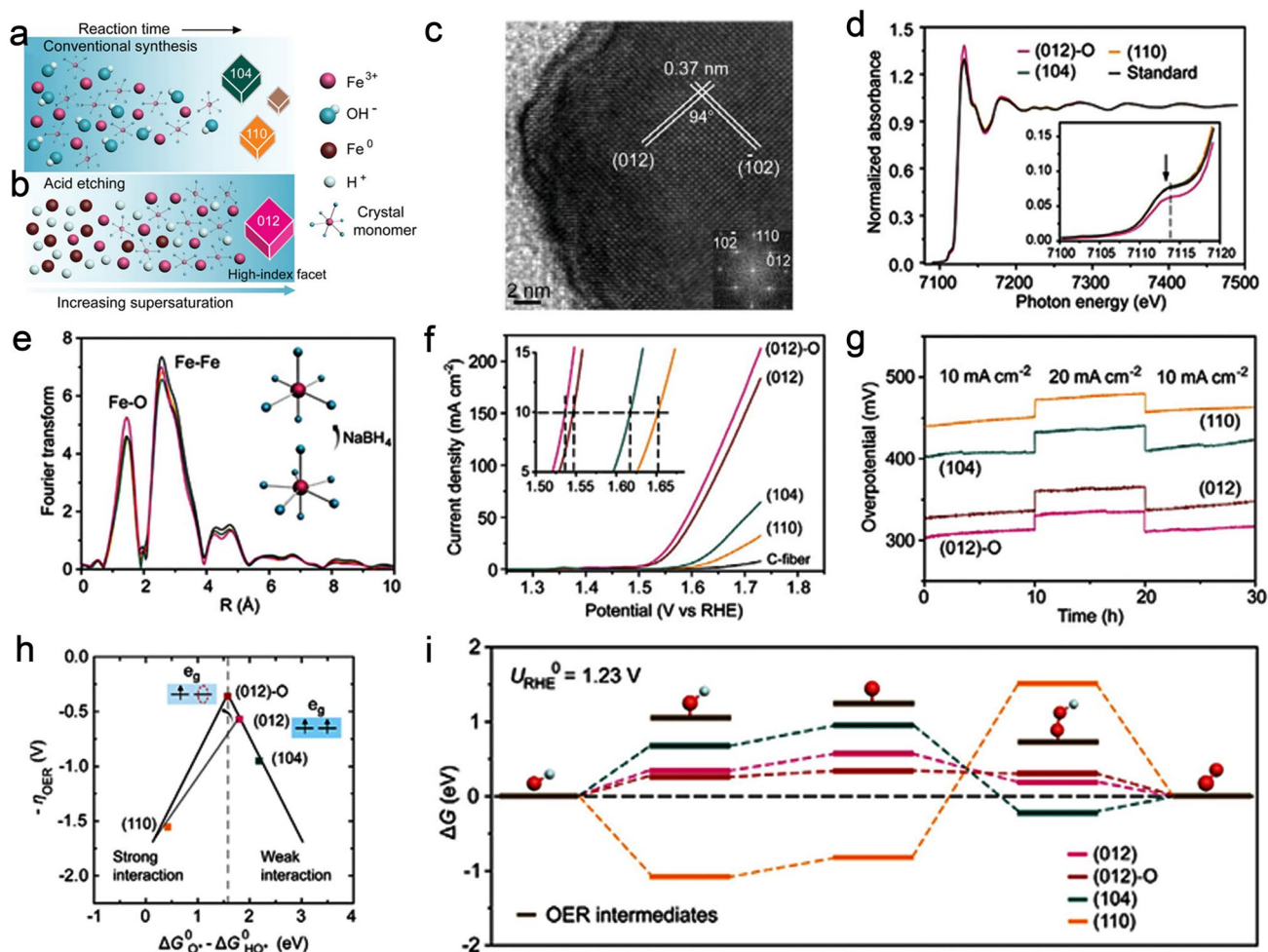


Fig. 14 Schematic representation of $\alpha\text{-Fe}_2\text{O}_3$ with different facets through **a** conventional solvothermal method and **b** acid-etching strategy. **c** HR-TEM image of the acid-etched $\alpha\text{-Fe}_2\text{O}_3$. **d** XANES spectra of the three nanocrystals and standard hematite. **e** FT of EXAFS. Inset, schematic illustration of six- and seven-coordinated configurations. **f** OER polarization curves of C-fiber, $\{110\}$ facets, $\{104\}$ facets, $\{012\}$ facets, and $\{104\}$ -O facets. **g** Galvanostatic stability measurements. **h** Calculated η against the standard free energy of $\Delta G_{\text{O}^-} - \Delta G_{\text{OH}^-}$ on $\{110\}$ facets, $\{104\}$ facets, $\{012\}$ facets, and $\{104\}$ -O facets. **i** Free energy diagram for OER on $\{110\}$ facets, $\{104\}$ facets, $\{012\}$ facets, and $\{104\}$ -O facets at $U = 1.23$ V. Reproduced with permission [70]. Copyright 2018, Wiley-VCH Verlag GmbH & Co

strengthens the weak bonding of the OER intermediates during the OER process, thus boosting the intrinsic catalytic activity. The exposed high-indexed {012} facets endowed corresponding α -Fe₂O₃ with high OER activity in 1.0 M NaOH, requiring a η of 317 mV to drive 10 mA cm⁻², which was lower compared to the value of {104} facets (388 mV) and {110} facets (422 mV) at the same current density (Fig. 14f). In addition, the Tafel slope of the {012} facets was 58.5 mV dec⁻¹, which was lower than that of {104} facets (62.5 mV dec⁻¹) and {110} facets (67.2 mV dec⁻¹). The α -Fe₂O₃ with the {012}-O facets exhibited superior stability than those of {012}, {104}, and {110} facets, which are observed from Fig. 14g. DFT studies unveiled that bonding between {104} facets and the two intermediates (HO* and O*) was too weak, while the {110} facet was excessively strong, indicating unfavorable OER kinetics. The {012} facets at the apex of the volcano diagram exhibited a relatively more suitable binding energy, which was beneficial for a favorable intermediary adsorption/desorption and thus generated a lower reaction energy barrier (Fig. 14h-i). However, Fe sites of the seven-coordinated Fe centers endowed the acid-etched α -Fe₂O₃ with the extension of Fe–O bonds, which can strengthen the weak bonding of oxygenated intermediates and accelerate the OER kinetics during the OER process. Therefore, compared to other facets, the {012}-O facets delivered the best OER properties with a relatively low Tafel slope of 51.8 mV dec⁻¹ and a smaller η of 305 mV at 10 mA cm⁻².

The morphology of metal oxides can be manipulated for the preparation of dominant highly active facets to boost OER performances. Wang et al. [193] fabricated NiO nanobelts and nanoplates with dominant {110} and {111} planes, respectively. The NiO nanobelts with dominant {110} planes exhibited the good electrocatalytic OER performance with a η of 382 mV at 50 mA cm⁻² superior to that of the NiO nanobelts with dominant {111} planes in 1.0 M KOH. DFT results demonstrated that the NiO nanobelts with dominant {110} planes exhibited the lower theoretical η (0.70 V) than {110} planes (1.70 V), illustrating the enhanced intrinsic electrocatalytic activity of {110} planes. The higher OER activity of {110} planes might be originated from the different crystallinities of NiO. Niu et al. [194] designed and synthesized four kinds of Fe₂O₃ (concave octahedral-Fe₂O₃ (CO-Fe₂O₃) with dominant {206} and {119} facets, rod-like Fe₂O₃ (RO-Fe₂O₃) with dominant {119} and {0012} facets, octahedron-like Fe₂O₃ (OC-Fe₂O₃) with dominant

{119} and {0012} facets, and spindle-like Fe₂O₃ (SP-Fe₂O₃) with dominant {203} facets) by pyrolyzing a series of FeO_x node-based MOFs. The 3D porous structure endowed CO-Fe₂O₃ with fast charge/mass transport, which could be beneficial for OER kinetics. Importantly, the CO-Fe₂O₃ featured the highly active facets of {206} and {119}, which could effectively boost the intrinsic catalytic activity. As a result, the CO-Fe₂O₃ exhibited better catalytic activity with a η of 439 mV and a Tafel slope of 99 mV dec⁻¹ which are better than those of RO-Fe₂O₃ (478 and 104 mV dec⁻¹), OC-Fe₂O₃ (533 and 115 mV dec⁻¹), and SP-Fe₂O₃ (575 and 120 mV dec⁻¹) in N₂-saturated 1.0 M KOH solution.

Similarly, Liu et al. [90] reported a hydrothermal strategy to fabricate CoMoO₄ nanorods (NR) predominantly enclosed by {100} facets and CoMoO₄ nanosheets (NS) mainly bounded by {010} facets. The CoMoO₄ NR required a η of 550 mV to yield 8.93 mA_{cat}⁻², lower than the value of the CoMoO₄ NS (1.56 mA_{cat}⁻²) at the same η . The major cause of the higher intrinsic OER activity of CoMoO₄ NR was related to exposed {100} facets and thus abundant Co active sites at {100} facets. Besides, DFT studies demonstrated that the {100} facets presented a higher surface energy of 0.54 J m⁻² than 0.41 J m⁻² for {010} facets, indicating {100} facets were more reactive toward OER. Wang and co-workers synthesized ferric vanadate (FeVO₄) nanosheets and nanobelts dominated by {001} and {010} facets, respectively [195]. The open surface structure and countless catalytic active sites of Fe and V on the {010} facets can enhance the electrocatalytic activity of FeVO₄ nanobelts toward OER with superior durability over 36 h continuous electrolysis, a small Tafel slope of 37.4 mV dec⁻¹ and a low η of 240 mV to obtain 10 mA cm⁻² in 1.0 M KOH electrolyte.

6.3 Metal Selenide Catalysts

The metal selenides have been widely developed as high-efficiency OER electrocatalysts thanks to their special layered architecture, relatively narrow bandgap and high intrinsic catalytic activity [33, 196, 197]. Dang et al. [198] proposed a high-temperature liquid-phase route to construct CoSe₂ nanosheets with dominant {001} facets (Fig. 15a). The exposure ratio of {001} facets can be tailored through varying the temperature. Apart from {001} facets, CoSe₂ nanosheets also featured other crystal facets including {111}-a, {111}-b, {011}, {010}, and {100}

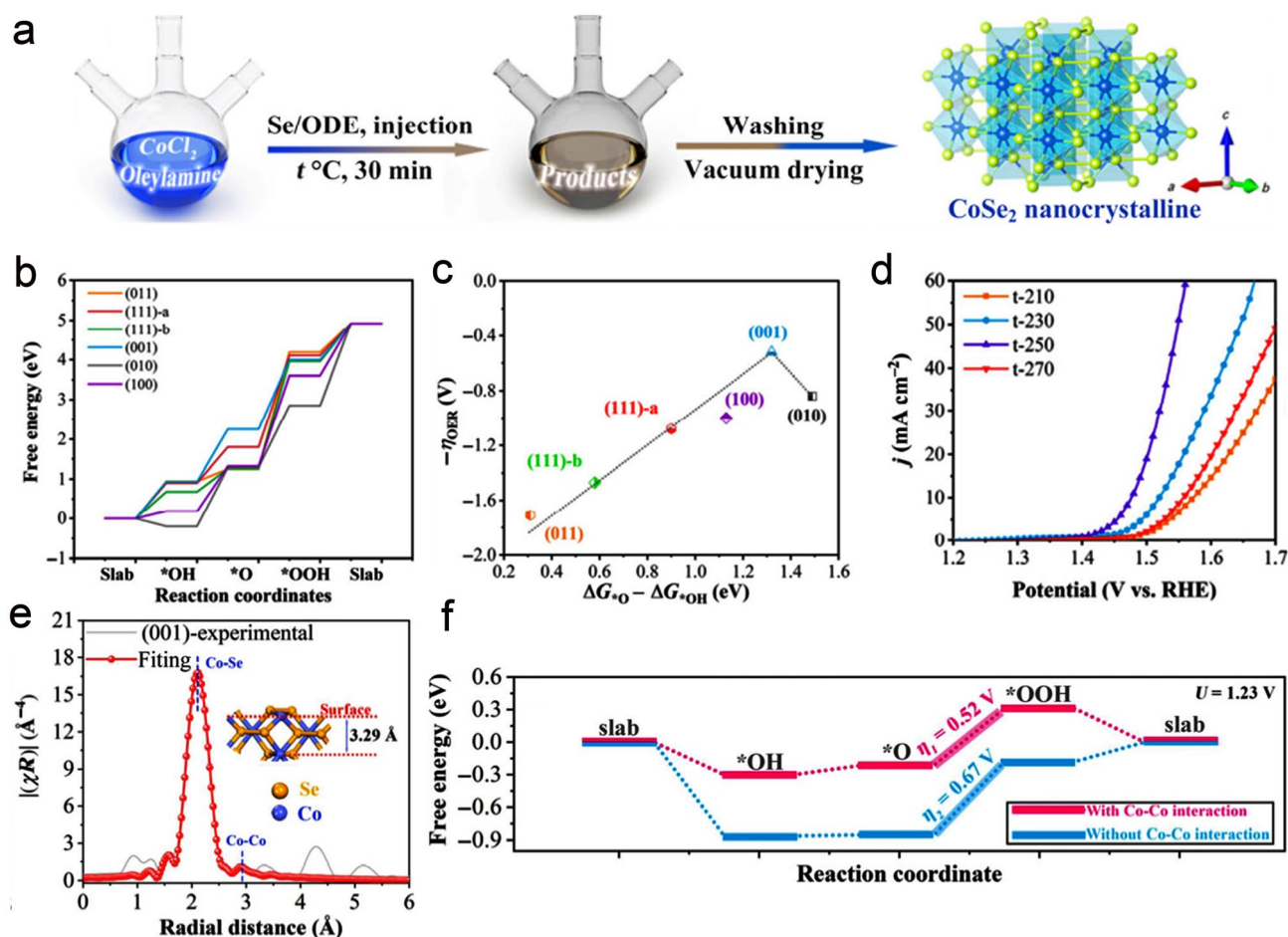


Fig. 15 **a** Synthesis of *o*-CoSe₂ nanocrystalline. **b** Reaction energy diagrams of the OER on (011) facets, (111)-a facets, (111)-b facets, (001) facets, (010) facets, and (100) facets, respectively. **c** Volcano plots for the OER overpotential on different crystal planes from **b**. **d** LSV curves of t-210, t-230, t-250, and t-270 for OER. Reproduced with permission [198]. Copyright 2021, Tsinghua University Press and Springer-Verlag GmbH Germany

facets (Fig. 15b). The OER activity of these crystal facets was investigated by the DFT calculation, and volcano plots of η for corresponding crystal facets were further performed to screen desired facets with relatively high intrinsic catalytic activity (Fig. 15c). As expected, CoSe₂ nanosheets with the exposure of {001} facets showed the better OER performance than CoSe₂ with other facets, requiring a η of 240 mV to drive a current density of 10 mA cm⁻² (Fig. 15d). The corresponding Tafel slope is 75.8 mV dec⁻¹. Interestingly, the XAS is used to study the coordination environment of Co in the CoSe₂ {001}. A small peak of about 2.9 Å, corresponding to the fitting length of 3.23 Å, is observed in Fig. 15e, which is very close to Co–Co path (3.29 Å) around the surface of the slab of *o*-CoSe₂ {001}. The XAS results demonstrated that

shorter Co–Co scattering path was a result of the shrinkage of the surface owing to the absence of Se atoms. The electronic structures of active sites can be tailored by dynamic short-range Co–Co interaction, which can improve OER catalytic performances. The DFT calculations further proved that shortened distance between Co atoms could enhance the electropositivity of active sites and tailor electronic structure, thus reducing the energy barrier of OER (Fig. 15f). In another study, Cai et al. [199] synthesized the dendrite-like nickel selenide (NiSe₂) with highly active {200} facets at different temperatures. The obtained NiSe₂ at 413 K disclosed good stability and OER activity with a Tafel slope of 71 mV dec⁻¹ and a η of 299 mV at 10 mA cm⁻² in 1.0 M KOH. The higher catalytic activity of NiSe₂ toward OER can be mainly ascribed to the

dendrite-like nanostructures along with high exposure ratio of {200} facets, resulting in high utilization ratio of active Ni sites.

6.4 Metal Hydroxide/Oxyhydroxide Catalysts

Layered double metal hydroxides (LDHs) usually contain metallic divalent cations (M^{II}), metallic trivalent cations (M^{III}) as well as interlayered anions (A^{n-}), which are written as $M^{II}_{1-x}M^{III}_x(OH)_2(A^{n-})_{x/n} \cdot yH_2O$ [200–203]. The layered structures of LDHs are utilized to expose more active facets, thereby enhancing the intrinsic catalytic activity [204, 205]. For example, Zhang et al. [206] synthesized a series of layered serpentine $Ni_3Ge_2O_5(OH)_4$ nanosheets. According to the proposed model (Fig. 16a), the theoretical calculations confirmed that {100} facets in a monolayered slab possessed lower Gibbs free energy to oxygenated intermediates than those of {001} facets in a monolayered slab and {001} facets a multilayered slab, indicating the highly active {100} facets for OER (Fig. 16b). The sheet-like morphology of $Ni_3Ge_2O_5(OH)_4$ was observed from the TEM image in

Fig. 16c. The $Ni_3Ge_2O_5(OH)_4$ with monolayered nanosheet possesses a higher electrochemical active surface area (ECSA), thus ensuring the higher electrocatalytic activity. Thus, synthesis thin layer and small size of $Ni_3Ge_2O_5(OH)_4$ can increase exposure of {100} facets and further add active sites, which is beneficial to boost OER catalytic performance. Monolayered $Ni_3Ge_2O_5(OH)_4$ nanosheet with highly exposed {100} facets demonstrated a low η of 320 mV to reach 10 mA cm^{-2} and a Tafel slope of 67.5 mV dec^{-1} (Fig. 16e, f). Zhao et al. [207] designed hierarchal NiFe LDH nanosheet-arrays-on-microplates (NiFe NSAs-MPs) with abundant exposed edge planes on nickel foam as high-efficiency OER electrocatalysts via a plane engineering method. Compared to NiFe LDHs microshtet arrays (NiFe MSAs) bounded by traditional {003} planes, the NiFe NSAs-MPs featured exposed edge planes of {012}, {015}, and {110} planes. The NiFe NSAs-MPs demonstrated an outstanding OER performance with a η of approximately 250 mV at 100 mA cm^{-2} as well as a small Tafel slope of 34.5 mV dec^{-1} in 1.0 M KOH, which is lower than that of the NiFe MSAs (300 mV and 63.0 mV dec^{-1}). The theoretical calculation disclosed that the Fe sites were recognized

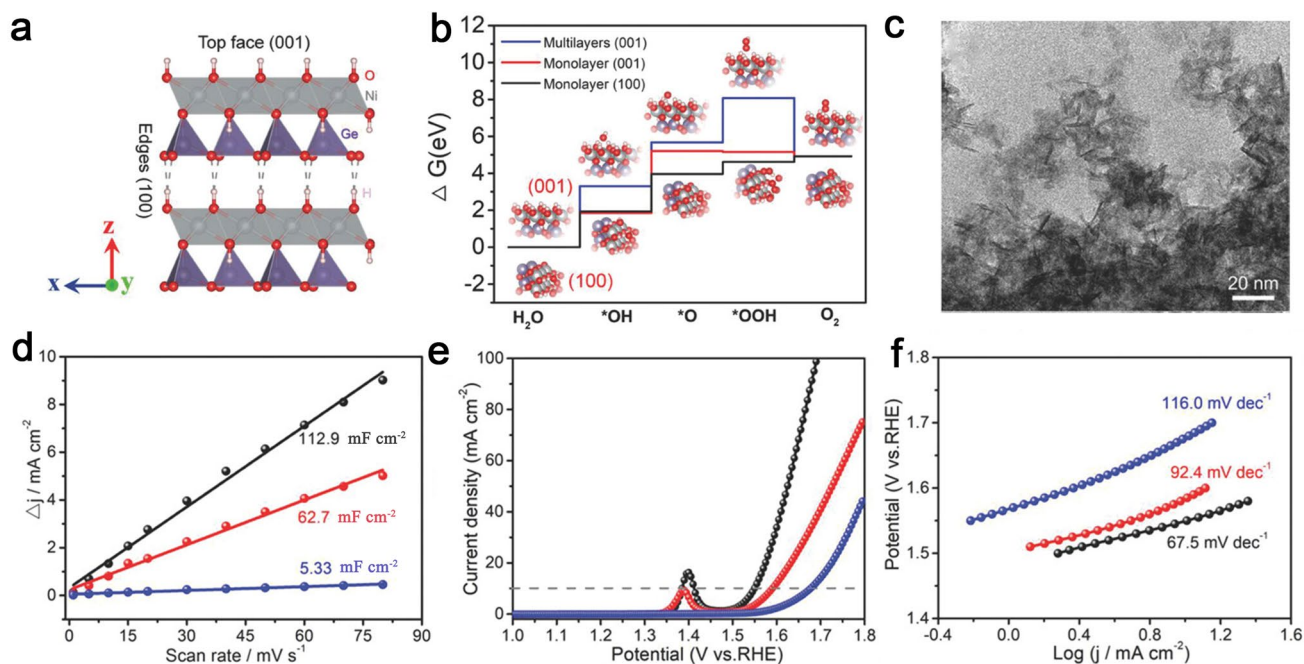


Fig. 16 **a** Crystal structure of a $Ni_3Ge_2O_5(OH)_4$ nanosheet with {001} on top face and {100} on edges. **b** Standard free energy diagrams of OER intermediates on {001} facet in multilayered slab, {001} facet in monolayer slab, and {100} facet in monolayer slab. **c** TEM image of monolayered nanosheets. **d** Current density differences plotted against scan rates. **e** Polarization curves, and **f** Tafel plots of monolayered nanosheets (black plots), five-layered nanosheets (red plots), and ten-layered nanosheets (blue plots). Reproduced with permission [206]. Copyright 2018, Wiley-VCH Verlag GmbH & Co

as the active reaction site instead of the Ni sites. The results of volcano plot showed that the Fe sites as active reaction sites on the {012} planes illustrated a lower η than those of other planes, indicating that {012} plane was the most active plane, which could account for the high OER catalytic performance of NiFe NSAs-MPs.

6.5 Metal–Organic Framework Catalysts

MOFs are assembled by metal nodes and organic linkers through coordination bond [43–45, 208–214]. MOFs generally feature well-defined and anisotropic crystal facets, which may lead to different electrocatalytic activity [46]. Thus, enlarging the proportion of active facets on the MOF surface can boost the intrinsic catalytic activity. Wan et al. [80] utilized sodium dodecyl sulfate (SDS) to reduce adsorption energies of specific facets during the ZIF-67 growth process and produced 2D ZIF-67 nanosheets with high

exposure of the {002} facets (Fig. 17a, b). The as-obtained 2D ZIF-67 generated 10 mA cm^{-2} at a η of 305 mV along with a Tafel slope of 67 mV dec^{-1} (Fig. 17c, d). In order to investigate why 2D ZIF-67 exhibited high catalytic performances toward OER, as shown in Fig. 17e, f, the DFT calculations were performed and the results revealed that {002} facets exhibited a lower η of 0.48 V than those of {011} and {111} facets. Zhao et al. developed a new and facile coordination modulation method to achieve accurate construction of 2D NiFe-MOFs with dominant exposed {001} facets [84]. Specifically, acetate ions were selected as the coordination modulators to fabricate ultrathin NiFe-MOFs nanosheets with mainly exposure of {001} facets, while the bulk NiFe-MOF was obtained without the coordination modulator. The highly exposed {001} facet of the 2D NiFe-MOFs offered abundant active sites, enhanced mass/charge transport and accelerated surface kinetics. The 2D NiFe-MOFs with mainly exposed {001} facets disclosed high OER properties with a Tafel slope of 73.4 mV dec^{-1}

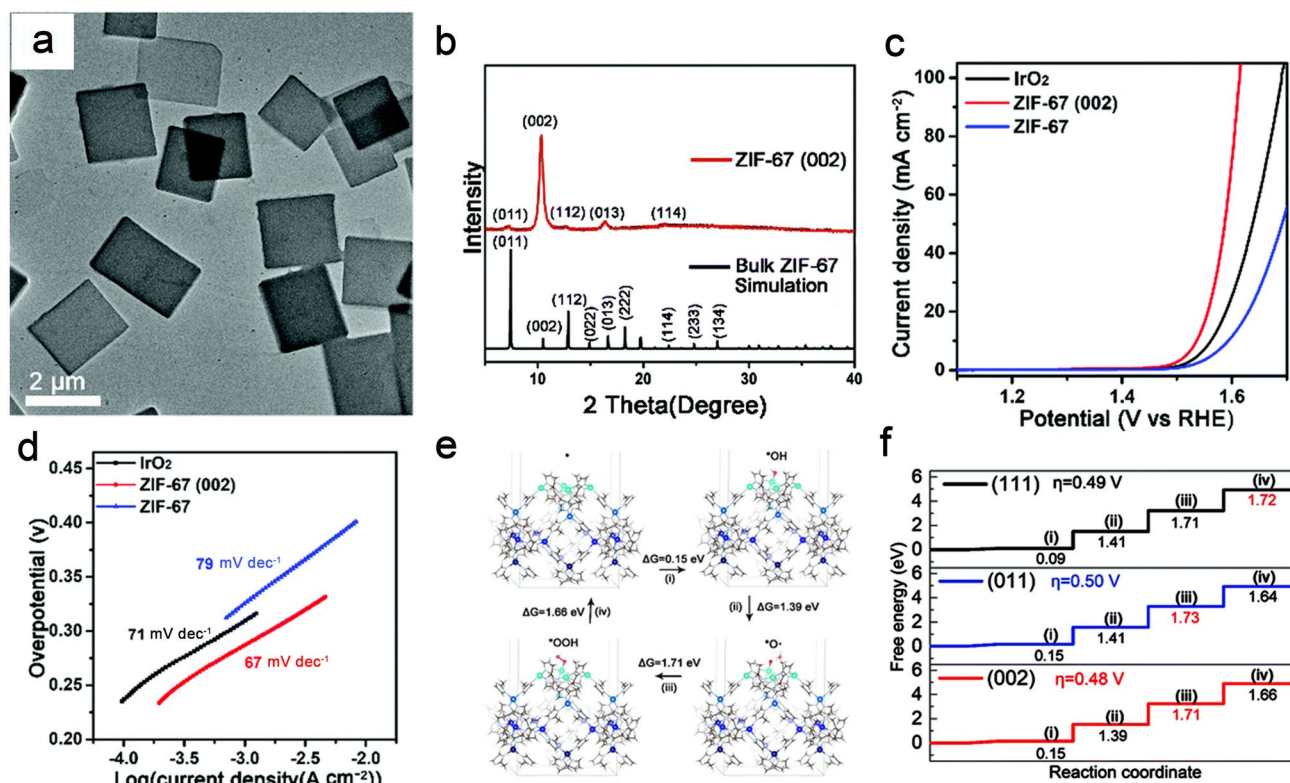


Fig. 17 a TEM image and b XRD pattern of ZIF-67 {002} facets. c LSV curves and d Tafel plots of IrO₂, ZIF-67 {002}, and ZIF-67. e Four energy steps of the OER process on ZIF-67 {002} surface. f Reaction energy diagrams of the OER for the {002}, {011}, and {111} facets, respectively. Reproduced with permission [80]. Copyright 2020, Royal Society of Chemistry

and an attractive η of 240 mV at 10 mA cm⁻² and superior stability over 16 h in 1.0 M KOH.

7 Facet-Engineered Bifunctional Catalysts for the Water Splitting

The simultaneous occurrence of the HER and OER under the same electrolyte is the prerequisite for practical electrolysis of water [13, 22]. Unfortunately, HER catalysts usually exhibit remarkable electrocatalytic activity in strong acidic solution, while OER catalysts typically demonstrate distinguished catalytic performances in strong alkaline solution. The mismatching of working conditions is an inevitable concern in searching for water splitting catalysts [215]. Importantly, the true catalytically active sites of the HER and OER are inconsistent. For example, reconstruction phenomena usually occur on the surface of metal oxides/phosphides/sulfides during anodic OER polarization, resulting in the formation of the real active sites [117, 216–219]. Due to the differences between HER and OER catalytic mechanisms, design high-efficiency bifunctional water splitting catalysts is a challenging project [220]. Crystal facet engineering has been regarded as the effective method to obtain dominant exposed highly active crystal facets. These crystal facets featured with abundant unsaturated coordination sites would present superior water splitting activity. Therefore, in the following, in-depth discussions about facet-engineered water splitting catalysts of metal oxides and sulfides are given as the typical examples.

7.1 Metal Oxide Catalysts

Pure metal oxides, especially the bulk materials, have not demonstrated satisfactory HER performances attributed to their poor electrical conductivity, which hinders the development of metal oxides for electrocatalytic water splitting [183, 184]. Thus, various strategies of doping, oxygen vacancy engineering, surface reconstruction, and facet engineering have been proposed to boost the HER activity [183]. Intriguingly, metal oxides constructed by facet engineering exhibit comparable catalytic performances toward both HER and OER. Liu et al. [221] successfully prepared four morphological Co₃O₄ catalysts including nanocube bounded by {001} facets, nanobelt enclosed by {110} facets, nanooctahedron dominated by {111} facets, and nanosheet with

exposed {112} facets. The electrochemical properties of these facets for OER, HER, and OWS were systematically explored in 1.0 M KOH. The {111} facets achieved better OER performances with the smallest η of 285 mV to afford a current density of 10 mA cm⁻² compared to those of {001} facets (362 mV), {110} facets (341 mV), and {112} facets (312 mV). The {111} facets exhibited a Tafel slope of 49 mV dec⁻¹, which was much lower than those of {001} facets (119 mV dec⁻¹), {110} facets (101 mV dec⁻¹) as well as {112} facets (73 mV dec⁻¹). Moreover, the {111} facets delivered better catalytic activity toward HER with a smaller η of 195 mV superior to those of {001} facets (284 mV), {110} facets (260 mV), and {112} facets (232 mV). The corresponding Tafel slopes of {111}, {001}, {110}, and {112} facets were 47, 97, 78, and 59 mV dec⁻¹. The Co₃O₄ nanooctahedron system ({111}||{111}) needed a potential of 1.60 V to reach 10 mA cm⁻² toward OWS, which was much lower than those of {001}||{001} (1.74 V), {110}||{110} (1.69 V), and {112}||{112} (1.65 V). DFT calculations were used to reveal the correlation between electrocatalytic activity and crystal facets (Table 1). The results demonstrated that the {111} facets possessed the highest surface energy, the biggest dangling bond density as well as the smallest absolute value of ΔG_{H} than those of other facets, which were responsible for the superior catalytic activity of {111} facets for both the OER and HER. Wu et al. proposed a hydrothermal synthesis of octahedral Co₃O₄ particles grown on cobalt foam [222]. An interplanar distance of 0.47 nm in Fig. 18a corresponds to the high-index {111} facets of the Co₃O₄, which is proven to feature satisfactory catalytic performances toward HER and OER. The octahedral Co₃O₄ particles with exposed high-index {111} facets displayed good HER, OER, and OWS performances with the η of 77.9, 301.2, and 370 mV to drive the current density of 10 mA cm⁻² in 1.0 M KOH, respectively. The high catalytic activity of the octahedral Co₃O₄ particles mainly originates from the exposure of a large number of high-index {111} facets as well as the existence of rich hydroxyl groups on cobalt oxide surface. Interestingly, as shown in Fig. 18b, c, after CV stability test, the catalytic performances of the octahedral Co₃O₄ particles for both HER and OER are improved. To investigate the reason of highly improved catalytic activity, The XRD, SEM, and BET tests to characterize the octahedral Co₃O₄ particles are performed. The XRD result showed the main phase peaks of the octahedral Co₃O₄ particles after HER/OER stability



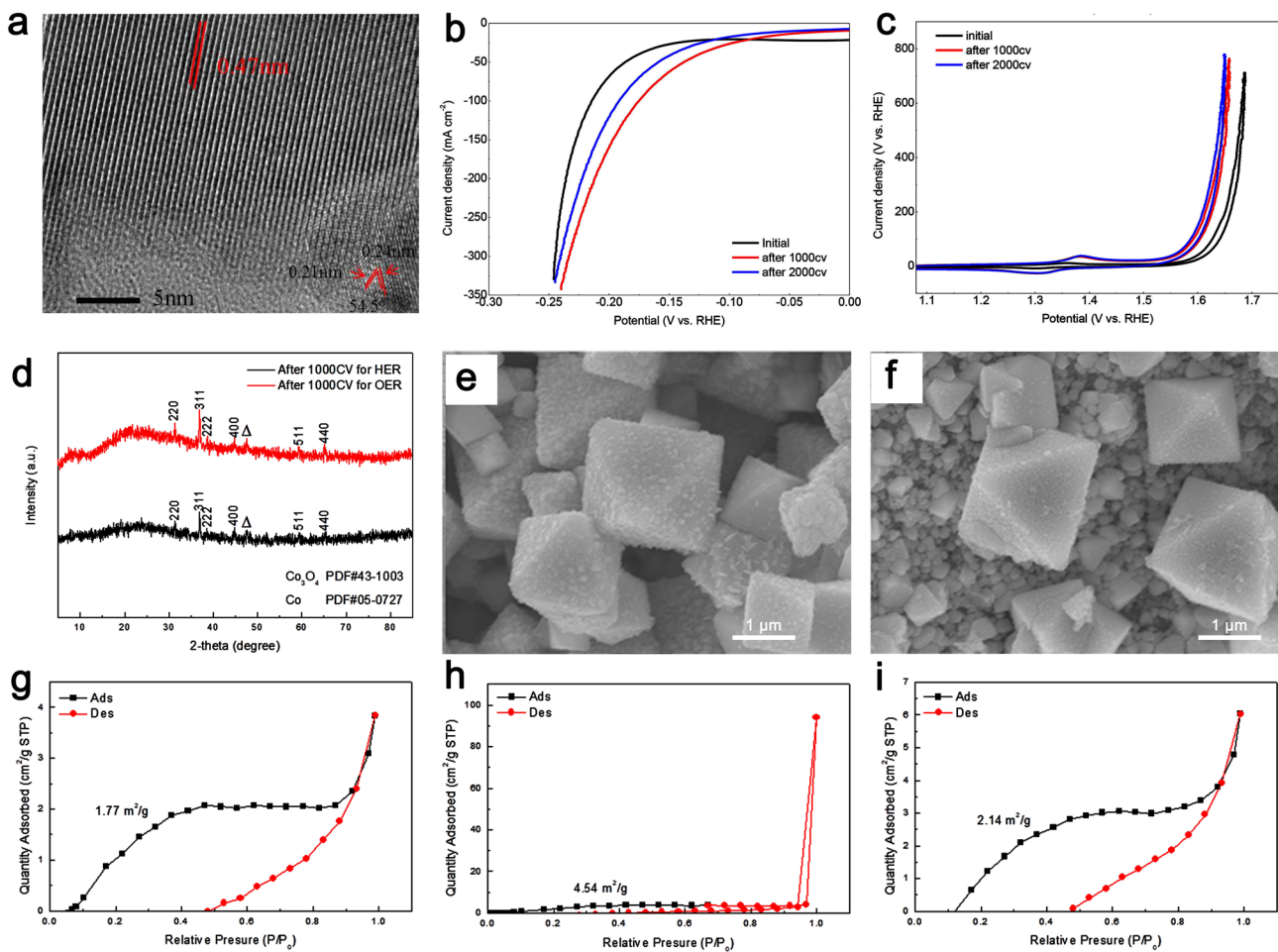


Fig. 18 **a** HR-TEM image of the octahedral Co_3O_4 particles. **b** HER and OER, **c** polarization curves before and after continuous potential sweeps at 50 mV s^{-1} . **d** XRD patterns of the octahedral Co_3O_4 particles after stability test of 1000 cycles. **e**, **f** SEM images of the octahedral Co_3O_4 particles after stability test of 1000 cycles toward **e** HER and **f** OER. BET adsorption and desorption isotherm for **g** octahedral Co_3O_4 particles, **h** octahedral Co_3O_4 particles after HER stability test, and **i** octahedral Co_3O_4 particles after OER stability test. Reproduced with permission [222]. Copyright 2018, Elsevier Ltd

tests are well preserved (Fig. 18d). The surface of the octahedral Co_3O_4 particles became significantly roughened after HER/OER stability tests (Fig. 18e, f). The results of BET tests illustrated that the increased specific surface area of the octahedral Co_3O_4 particles after HER/OER stability test is observed from Fig. 18g-i, which can expose more electrochemically active sites and thus enhance electrocatalytic activity toward HER and OER.

In another typical example, Fang et al. [223] proposed a simple and general method of controlling the pH of the solution for the preparation of NiCo_2O_4 nanosheet enclosed by {110} crystal planes, NiCo_2O_4 octahedron bounded by {111} crystal planes as well as NiCo_2O_4 -truncated

octahedron dominated by {111} and {100} crystal planes, respectively (Fig. 19a-c). Theoretical calculations were performed to evaluate catalytic activity of these crystal planes. As illustrated in Fig. 19d-g and Table 1, compared to {111} planes and {100} planes, the {110} planes exhibited smaller ΔG_{H} for HER and lower energy barrier for OER as well as higher surface energy for adsorption of ionized oxygen species. The results evidenced that the catalytic performances of three exposed facets for HER and OER followed the order of {110} > {111} > {100}. The NiCo_2O_4 nanosheet required a η of 157 mV to drive 5 mA cm^{-2} , which is lower than the value of NiCo_2O_4

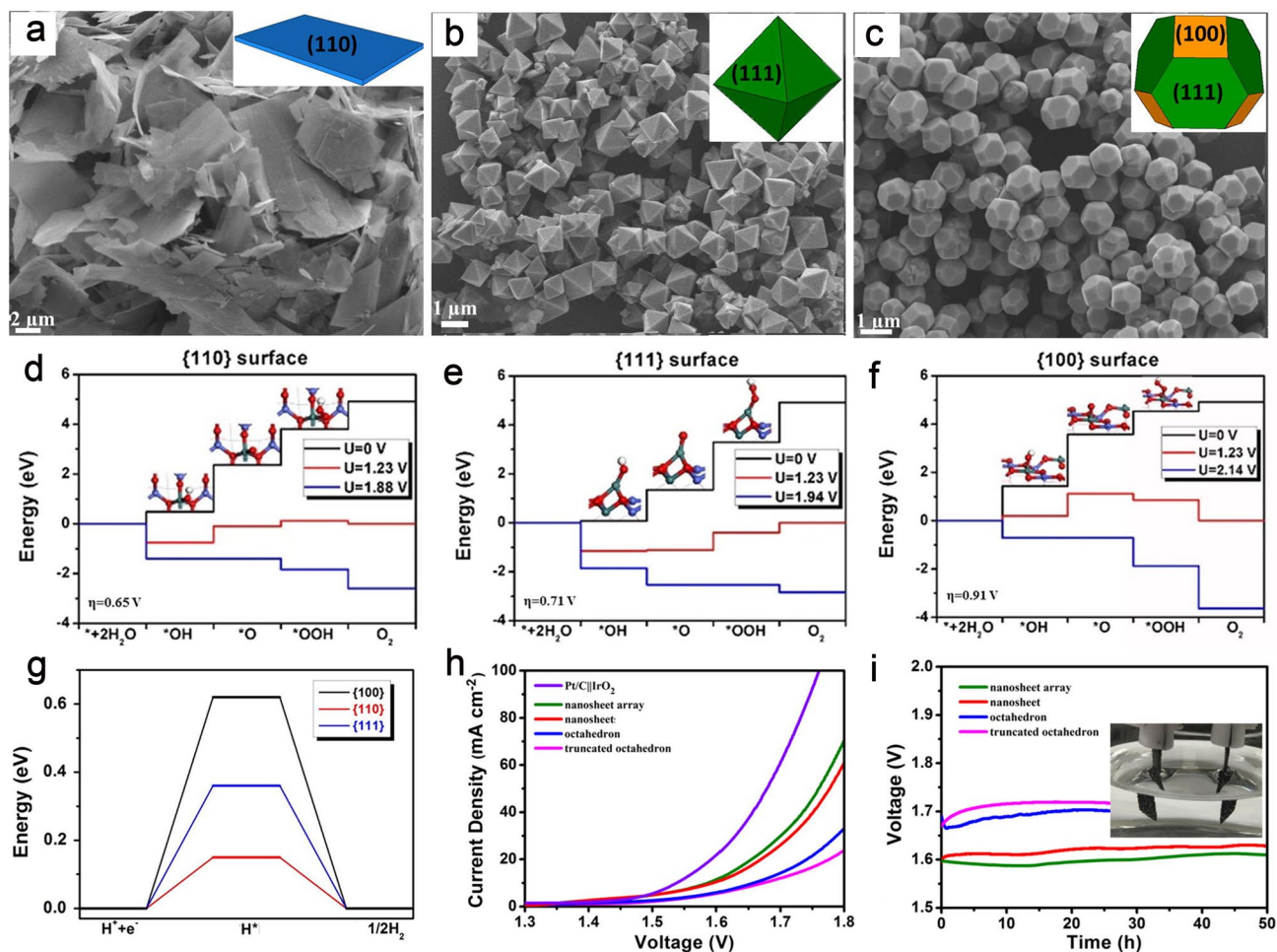


Fig. 19 SEM images of **a** NiCo_2O_4 nanosheets with the exposed $\{110\}$ facet, **b** NiCo_2O_4 octahedrons enclosed by $\{111\}$ facet, and NiCo_2O_4 -truncated octahedrons bounded by $\{111\}$ and $\{100\}$ facet, respectively. Reaction energy diagrams of OER for **d** the $\{110\}$, **e** the $\{111\}$, and **f** the $\{100\}$ facet. **g** Free energy diagram of $\{100\}$, $\{110\}$, and $\{111\}$ for HER, respectively. **h** LSV curves of the OWS for a series of NiCo_2O_4 catalysts and $\text{Pt/C}||\text{IrO}_2$. **i** Long-term stability measurement for a series of NiCo_2O_4 catalysts at 10 mA cm^{-2} . Reproduced with permission [223]. Copyright 2017, Elsevier Inc

octahedron (197 mV) and NiCo_2O_4 -truncated octahedron (223 mV). The corresponding Tafel slopes were 71.2, 93.8, and $110.3 \text{ mV dec}^{-1}$. The NiCo_2O_4 nanosheet illustrated better OER activity with a smaller potential of 1.56 V and a lower Tafel slope of 59.2 mV dec^{-1} compared to the values of NiCo_2O_4 octahedron (1.59 V and 78.1 mV dec^{-1}) and NiCo_2O_4 -truncated octahedron (1.63 V and 86.9 mV dec^{-1}). The NiCo_2O_4 nanosheet displayed excellent electrocatalytic stability toward OWS and reached 10 and 20 mA cm^{-2} at 1.59 and 1.65 V, respectively, which were smaller than the value of NiCo_2O_4 octahedron (1.60 and 1.67 V) and NiCo_2O_4 -truncated octahedron (1.66 and 1.74 V) at the same current density (Fig. 19h, i).

7.2 Metal Sulfide Catalysts

Benefitting from the low cost, excellent conductivity, and considerable electrocatalytic activity, metal sulfides, especially nickel sulfides, are explored as bifunctional electrocatalysts for HER/OER [95, 224]. Dong et al. developed the methods of anodization and vapor sulfurization to synthesis nanoporous thin films of Ni_3S_2 with exposed $\{003\}$ facets supported on nickel foil (Ni_3S_2 NTFs) [225]. The XRD results illustrated Ni_3S_2 catalysts with different sulfurization time possessed $\{003\}$ facets (Fig. 20a). The optimized Ni_3S_2 -300 (sulfurization time of 300 s) displayed remarkable electrocatalytic activity toward HER and OER in alkaline

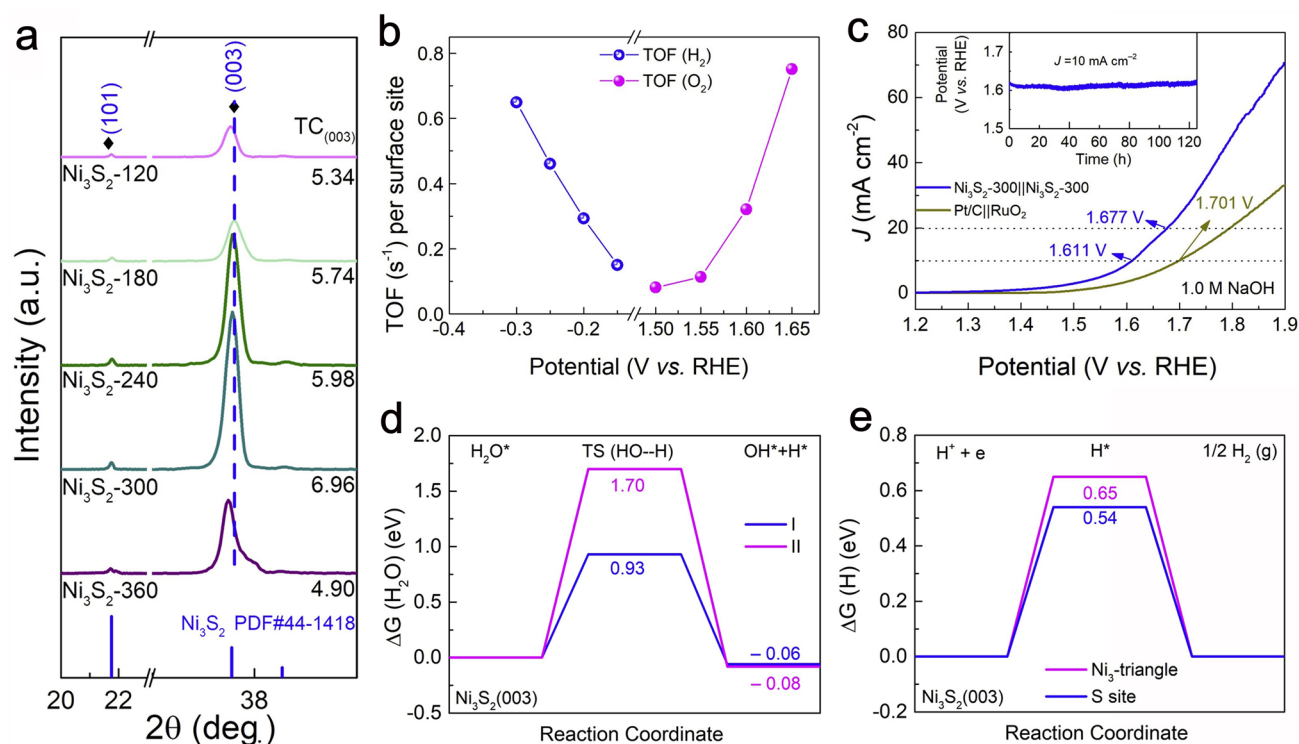


Fig. 20 **a** XRD patterns of Ni₃S₂ with the different sulfurization time. **b** TOFs of Ni₃S₂-300 plotted against potential for HER and OER. **c** LSV curves of the OWS for the Ni₃S₂-300||Ni₃S₂-300 and Pt/C||RuO₂ catalysts. Calculated adsorption free energy diagrams for the **d** Volmer step and **e** Tafel step on the Ni₃S₂(003) facet model. Reproduced with permission [225]. Copyright 2018, Elsevier B.V

electrolyte with a η of 135 and 175 mV at 10 mA cm⁻², respectively. The corresponding Tafel slope was 75.5 and 101.2 mV dec⁻¹. The Ni₃S₂/NF presented TOF values of 0.649 and 0.751 s⁻¹ at the η of 300 and 400 mV for HER and OER, respectively (Fig. 20b). The Ni₃S₂-300 employed as both anode and cathode electrodes could produce 10 mA cm⁻² at 1.61 V in 1.0 M NaOH electrolyte (Fig. 20c). The superior performance of the Ni₃S₂ is due to accessibility of accessible catalytic active sites and mass transfer channels provided by the controllable hollow nanoporous spheres. Remarkably, the DFT studies revealed that Ni₃-triangles on {003} facets exhibited a lower energy barrier of 0.93 eV toward water dissociation than S sites, which can be considered as more active for O–H bond cleavage during the Volmer step. However, the S atoms demonstrated smaller ΔG_{H} value compared to that of Ni₃-triangles, illustrating that S sites were more appropriate for the generation of molecular hydrogen during the Tafel step (Fig. 20d, e). The theoretically result unveiled Ni₃-triangles of Ni₃S₂ {003} facets can boost water dissociation dynamics. For OER, the

major cause of high catalytic performance is related to the combined effects of Ni₃S₂ and NiOOH.

In another work, Feng et al. constructed Ni₃S₂ nanosheet arrays dominated by high-index {210} facets and low-index {001} facets on foam nickel (Ni₃S₂/NF) via the direct sulfurization method [92]. The nanosheet array architecture and highly active {210} facets of the Ni₃S₂/NF guaranteed the distinguished HER and OER catalytic activity in 1.0 M NaOH with a η of 223 and 260 mV to yield the cathodic and anodic current densities of 10 mA cm⁻², respectively. The electrolyzer assembled by Ni₃S₂/NF as both anode and cathode could produce a water splitting current density of about 13 mA cm⁻² at approximately 1.76 V. The DFT computations were performed to understand the surface structures and the catalytic activity of {210} and {001} facets. The R ring site containing two Ni5 sites on the terrace of {210} facets were the most active site and possessed the lowest ΔG_{H} of 0.496 eV, indicating the high catalytic activity of the R ring site toward HER. The DFT results also disclosed that {210} facets required a smaller η of 0.58 V compared

to the value of $\{001\}$ facets (0.70 V), demonstrating better catalytic activity of $\{\bar{2}10\}$ facets toward OER.

8 Summary and Outlook

Benefitting from the advantages of high energy density, natural abundance, and clean combustion, hydrogen is considered as the ideal clean fuel capable of solving global energy crisis and environmental issues and thus realizing carbon neutrality. Electrocatalytic water splitting provides an effective route to produce high-purity hydrogen with zero environmental pollution. The crystal facets featured with facet-dependent physical and chemical properties would exhibit different catalytic activity and selectivity toward HER and OER attributed to their anisotropy. Crystal facet engineering can control the percentage of target crystal planes on the entire crystal surface. Therefore, tailoring crystal planes by crystal facet engineering and further exposing dominant crystal planes with high activity is an effective strategy, which is beneficial for constructing and exploring high-performance OER/HER catalysts. In this review, we firstly outlined the basic concepts, fundamental mechanisms, and evaluation parameters of HER and OER. Then, we summarized the formation mechanisms of the targeted crystal facets and introduced various strategies (selective capping agent, selective etching agent, and coordination modulation) to elaborately control crystal planes. Besides, we also summarized the significant contributions of facet-engineered catalysts toward HER, OER, and OWS. In particular, we highlighted that the DFT calculations played an indispensable role in explaining the superior electrocatalytic activity of dominant crystal planes. Furthermore, some typical examples of facet-engineered electrocatalysts for HER, OER, and OWS are summarized in Table 2. As discussed above, although exciting advancements have been made in facet-engineered electrocatalysts for HER, OER, and OWS, some challenges still exist in the following aspects (Fig. 21):

Firstly, thus far, there are limited strategies to tailor crystal facets and reported strategies possess inherent disadvantages. For the first and second strategies (selective capping agent and selective etching agent) to control planes, the selective effect between the added reagents and the targeted crystal planes is the prerequisite. Worse yet, the strategy of coordination modulation is currently only applicable to MOFs. Additionally, the variety of water splitting catalysts

designed by crystal facet engineering is far from abundant to realize industrial hydrogen production. The design and exploration of water splitting catalysts can be beneficial to simplify electrolyzer design, avoid the mismatch of electrolyte, and reduce the cost in device fabrication. Therefore, more attentions should be paid to developing advanced crystal facet control strategies for the construction of promising water splitting catalysts with highly active facets.

Secondly, although high-index facets present satisfactory catalytic performance toward HER/OER, challenges still exist for the preparation of high-index facets. High-index facets usually exhibit a high ratio of low-coordinated atoms, edges, kinks and steps, providing more highly electrocatalytic active sites. However, high-index facets are unstable and often evolve and disappear quickly because of their high surface energy. Accordingly, the design and exploration of new synthetic methods or new capping and etching agents for tailoring the crystal growth process aiming to preserve high-index facets are crucial and highly urgent.

Thirdly, in spite of amazing catalytic performance toward HER/OER for facet-engineered catalysts, the catalytic mechanism and active sites involved in facet-engineered catalysts are still unclear during the HER/OER process. In situ/operando characterization technologies, such as in situ PXRD, in situ XPS, in situ Raman, in situ TEM, and in situ XAS, can track the evolving behavior during HER/OER process, especially the generation and disappearance of hydrogen or oxygen intermediates, and unveil the real catalytic sites, which contributes to determining the HER/OER mechanisms and further uncover the association between the crystal plane and catalytic activity. Unfortunately, a single in situ/operando technique currently cannot offer a complete picture during the dynamic evolution of HER or OER. Accordingly, the collaborative combination of these techniques is of significant for effectively integrating experimental information.

Fourthly, although the arrangement structure and coordination microenvironment of atoms on the crystal plane can greatly affect electrocatalytic activity, the elaborate design of highly active facet-dependent catalysts still faces following challenges: (1) how to adjust the arrangement structure and coordination microenvironment of atoms on the crystal plane at the molecular level to improve inherent catalytic performance; (2) establishment of the structure–activity relationship between the dominant crystal plane and its macroscopic electrocatalytic performance. Intriguingly, the DFT calculation is beneficial to predict the trend in catalytic

Table 2 Summary of facet-engineered catalysts for the HER, the OER, and the OWS

Catalysts	Substrates	Electrolyte/reactions	Dominant facets	Overpotential η (mV) at 10 mA cm ⁻²	Tafel slope (mV dec ⁻¹)	References
Pt NDs	Glassy carbon	0.5 M H ₂ SO ₄ /HER	{111}	27	22.2	[161]
Raspberry-like SbPt NPs	Glassy carbon	0.5 M H ₂ SO ₄ /HER	{110}, {100}, {101}, {012}	27	50.5	[162]
Pt NSs/CNTs	Glassy carbon	1.0 M KOH/HER	{311}, {200}, {111}	36	44	[160]
Ni _{1.8} Cu _{0.2} -P/NF	Ni foam	1.0 M KOH/HER	{201}	78	70	[226]
CoP UPNSs	Glassy carbon	0.5 M H ₂ SO ₄ /HER	{200}	56	32	[227]
Ni ₃ P ₄ MBs	Ti foil	0.5 M H ₂ SO ₄ /HER 1.0 M KOH/HER	{001}	35.4 47	48 56	[165]
Ni ₂ P	Ti foil	0.5 M H ₂ SO ₄ /HER	{001}	130@20	30	[167]
Ni ₃ P ₄ -Co ₂ P/NCF	Ni-Co alloy foam	1.0 M KOH/HER	{303}	21	23	[170]
Ni ₂ S-octa	Glassy carbon	1.0 M KOH/HER	{111}	138	139	[82]
Meso-FeS ₂	Ni foam	0.1 M KOH	{210}	96	78	[110]
V ₂ Se ₉ @PEDOT NSs/NF	Ni foam	0.5 M H ₂ SO ₄ /HER	{100}	72	36.5	[228]
V ₈ C ₇ @GC NSs/NF	Ni foam	1.0 M KOH/HER 0.5 M H ₂ SO ₄ /HER 1.0 M PBS/HER	{110}	49 38 77	44.5 34.5 64	[178]
TaC NCs@C	Glassy carbon	0.5 M H ₂ SO ₄ /HER	{222}	146	143	[94]
GaN	GaN self-made electrode	1.0 M KOH/HER 0.5 M H ₂ SO ₄ /HER	{100}	171 168	45 36	[73]
Pd@Ir TOH	Glassy carbon	0.1 M HClO ₄ /OER	{331}	300	84.9	[191]
Ag _{2-x} O/FTO-1	FTO	0.1 M K ₂ B ₄ O ₇ /OER	{111}	417	47	[192]
α -Fe ₂ O ₃	Carbon fiber paper	1.0 M NaOH/OER	{012}-O	305	51.8	[70]
MnO polypods	Glassy carbon	0.1 M KOH/OER	{100}	580	149	[229]
CoMoO ₄ NR	Glassy carbon	1.0 M KOH/OER	{100}	550@8.93	72	[90]
FeVO ₄ nanobelts	Ni foam	1.0 M KOH/OER	{010}	240	37.4	[195]
CO-Fe ₂ O ₃	Glassy carbon	0.1 M KOH/OER	{206}, {119}	439	99	[194]
NiO nanobelts	Ni foam	1.0 M KOH/OER	{110}	382@50	142.5	[193]
CoSe ₂ -250	Glassy carbon	1.0 M KOH/OER	{001}	240	75.8	[198]
NiSe ₂	Glassy carbon	1.0 M NaOH/OER	{200}	310	71	[199]
NiFe NSAs-MPs	Ni foam	1.0 M KOH/OER	{012}	250@100	34.5	[207]
Ni ₃ Ge ₂ O ₅ (OH) ₄ nanosheets	Glassy carbon	1.0 M KOH/OER	{100}	320	67.5	[206]
NiFe-MOF NSs	Glassy carbon	1.0 M KOH/OER	{001}	240	73.44	[84]
ZIF-67 (002)	Glassy carbon	1.0 M KOH/OER	{002}	305	67	[80]
Co ₃ O ₄ nanooctahedron	Ni foam	1.0 M KOH/OWS	{111}	370	/	[221]
NiCo ₂ O ₄ nanosheet	Ni foam	1.0 M KOH/OWS	{111}	360	/	[223]
NiMoN nanowire	Ni foam	1.0 M KOH/OWS	{100}	270	/	[230]
Ni ₃ S ₂ -300	Ni foam	1.0 M NaOH/OWS	{003}	390	/	[225]
Ni ₃ S ₂ /NF	Ni foam	1.0 M KOH/OWS	{ $\bar{1}$ 11}	~320	/	[95]
Ni ₃ S ₂ /NF	Ni foam	1.0 M NaOH/OWS	{ $\bar{2}$ 10}	590@13	/	[92]
TiO ₂ @Ni ₃ S ₂	Ni foam	1.0 M KOH/OWS	{ $\bar{2}$ 10}	350	/	[224]

activity, indicate the real active sites as well as reveal the structure–activity correlations between the dominant crystal plane and electrocatalytic activity. More significantly, owing to the difference between real-world conditions and

ideal world conditions for the proposed theoretical structural model, inconsistency between simulation results and experimental results is still unavoidable. Therefore, calling for more attention focus on develop high-efficiency

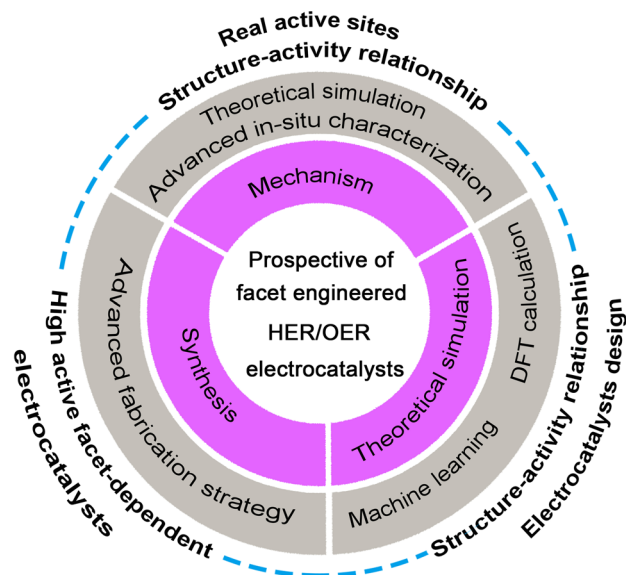


Fig. 21 Schematic diagram of the future development of facet-engineered HER/OER electrocatalysts

computer software and further design advanced theoretical models of DFT computation, which is beneficial for addressing the above-mentioned challenges and providing valuable principles to the scientific design of high-performance electrocatalysts.

Last but not the least, it is time-consuming and labor-intensive to prepare/screen highly active facet-dependent catalysts from experiments. The machine learning (ML) has emerged as a powerful artificial intelligence (AI) tool capable of data mining and data analysis, and thus providing valuable insights on electrocatalyst design and performance evaluation. The ML featured with powerful data-processing capabilities guarantees the low cost and high efficiency during the process of screening the high-performance electrocatalyst. More importantly, the ML can predict electrocatalytic activity with an accuracy close to DFT. Accordingly, with the help of the ML, constructing the model and further simulating the electrochemical process of active crystal faces are expected to reveal the structure–activity relationship between active facets and electrochemical performances. More effort should be devoted to developing the advanced AI technologies intending to rationally designing facet-dependent electrocatalysts with high activity.

Acknowledgements Dr. He gratefully appreciates the financial support from the National Natural Science Foundation of China (No. 22005147). Dr. You acknowledges the financial support from the National Key Research and Development Program of China

(2021YFA1600800), the Innovation and Talent Recruitment Base of New Energy Chemistry and Device (B21003), and the Open Research Fund of Key Laboratory of Material Chemistry for Energy Conversion and Storage (HUST), Ministry of Education (2021JYBK03).

Funding Open access funding provided by Shanghai Jiao Tong University.

Open Access This article is licensed under a Creative Commons Attribution 4.0 International License, which permits use, sharing, adaptation, distribution and reproduction in any medium or format, as long as you give appropriate credit to the original author(s) and the source, provide a link to the Creative Commons licence, and indicate if changes were made. The images or other third party material in this article are included in the article's Creative Commons licence, unless indicated otherwise in a credit line to the material. If material is not included in the article's Creative Commons licence and your intended use is not permitted by statutory regulation or exceeds the permitted use, you will need to obtain permission directly from the copyright holder. To view a copy of this licence, visit <http://creativecommons.org/licenses/by/4.0/>.

References

1. M. Chatenet, B.G. Pollet, D.R. Dekel, F. Dionigi, J. Deseure et al., Water electrolysis: from textbook knowledge to the latest scientific strategies and industrial developments. *Chem. Soc. Rev.* **51**(11), 4583–4762 (2022). <https://doi.org/10.1039/d0cs01079k>
2. D.H. Yang, Y. Tao, X. Ding, B.H. Han, Porous organic polymers for electrocatalysis. *Chem. Soc. Rev.* **51**(2), 761–791 (2022). <https://doi.org/10.1039/d1cs00887k>
3. J. Zhu, L. Hu, P. Zhao, L.Y.S. Lee, K.Y. Wong, Recent advances in electrocatalytic hydrogen evolution using nanoparticles. *Chem. Rev.* **120**(2), 851–918 (2020). <https://doi.org/10.1021/acs.chemrev.9b00248>
4. Z.W. Seh, J. Kibsgaard, C.F. Dickens, I. Chorkendorff, J.K. Nørskov et al., Combining theory and experiment in electrocatalysis: insights into materials design. *Science* **355**(146), 6321–6333 (2017). <https://doi.org/10.1126/science.aad4998>
5. C. Du, P. Li, Z. Zhuang, Z. Fang, S. He et al., Highly porous nanostructures: rational fabrication and promising application in energy electrocatalysis. *Coord. Chem. Rev.* **466**, 214604 (2022). <https://doi.org/10.1016/j.ccr.2022.214604>
6. L. Zhang, R. Li, H. Zang, H. Tan, Z. Kang et al., Advanced hydrogen evolution electrocatalysts promising sustainable hydrogen and chlor-alkali co-production. *Energy Environ. Sci.* **14**(12), 6191–6210 (2021). <https://doi.org/10.1039/d1ee02798k>
7. B. You, M.T. Tang, C. Tsai, F. Abild-Pedersen, X. Zheng et al., Enhancing electrocatalytic water splitting by strain engineering. *Adv. Mater.* **31**(17), 1807001 (2019). <https://doi.org/10.1002/adma.201807001>



8. B. You, X. Liu, N. Jiang, Y. Sun, A general strategy for decoupled hydrogen production from water splitting by integrating oxidative biomass valorization. *J. Am. Chem. Soc.* **138**(41), 13639–13646 (2016). <https://doi.org/10.1021/jacs.6b07127>
9. P. Aggarwal, D. Sarkar, K. Awasthi, P.W. Menezes, Functional role of single-atom catalysts in electrocatalytic hydrogen evolution: current developments and future challenges. *Coord. Chem. Rev.* **452**, 214289 (2022). <https://doi.org/10.1016/j.ccr.2021.214289>
10. K. Chen, Z. Wang, L. Wang, X. Wu, B. Hu et al., Boron nanosheet-supported Rh catalysts for hydrogen evolution: a new territory for the strong metal-support interaction effect. *Nano-Micro Lett.* **13**(1), 138 (2021). <https://doi.org/10.1007/s40820-021-00662-y>
11. L. Li, P. Wang, Q. Shao, X. Huang, Metallic nanostructures with low dimensionality for electrochemical water splitting. *Chem. Soc. Rev.* **49**(10), 3072–3106 (2020). <https://doi.org/10.1039/d0cs00013b>
12. Z. Zhang, X. Wu, Z. Kou, N. Song, G. Nie et al., Rational design of electrospun nanofiber-typed electrocatalysts for water splitting: a review. *Chem. Eng. J.* **428**, 131133–131145 (2022). <https://doi.org/10.1016/j.cej.2021.131133>
13. X. Fu, R. Shi, S. Jiao, M. Li, Q. Li, Structural design for electrocatalytic water splitting to realize industrial-scale deployment: strategies, advances, and perspectives. *J. Energy Chem.* **70**, 129–153 (2022). <https://doi.org/10.1016/j.jechem.2022.02.010>
14. J.N. Hausmann, R. Schlögl, P.W. Menezes, M. Driess, Is direct seawater splitting economically meaningful? *Energy Environ. Sci.* **14**(7), 3679–3685 (2021). <https://doi.org/10.1039/d0ee03659e>
15. S. Sanati, A. Morsali, H. García, First-row transition metal-based materials derived from bimetallic metal-organic frameworks as highly efficient electrocatalysts for electrochemical water splitting. *Energy Environ. Sci.* **15**, 3119 (2022). <https://doi.org/10.1039/d1ee03614a>
16. W. Li, C. Wang, X. Lu, Conducting polymers-derived fascinating electrocatalysts for advanced hydrogen and oxygen electrocatalysis. *Coord. Chem. Rev.* **464**, 214555 (2022). <https://doi.org/10.1016/j.ccr.2022.214555>
17. S. Jin, Are metal chalcogenides, nitrides, and phosphides oxygen evolution catalysts or bifunctional catalysts? *ACS Energy Lett.* **2**(8), 1937–1938 (2017). <https://doi.org/10.1021/acseenergylett.7b00679>
18. K. Zhu, X. Zhu, W. Yang, Application of in situ techniques for the characterization of NiFe-based oxygen evolution reaction (OER) electrocatalysts. *Angew. Chem. Int. Ed.* **58**(5), 1252–1265 (2019). <https://doi.org/10.1002/anie.201802923>
19. M. Yu, E. Budiyo, H. Tuysuz, Principles of water electrolysis and recent progress in cobalt-, nickel-, and iron-based oxides for the oxygen evolution reaction. *Angew. Chem. Int. Ed.* **60**, 2–26 (2021). <https://doi.org/10.1002/anie.202103824>
20. Z.P. Wu, H. Zhang, S. Zuo, Y. Wang, S.L. Zhang et al., Manipulating the local coordination and electronic structures for efficient electrocatalytic oxygen evolution. *Adv. Mater.* **33**, 2103004 (2021). <https://doi.org/10.1002/adma.202103004>
21. Q. Liang, J. Chen, F. Wang, Y. Li, Transition metal-based metal-organic frameworks for oxygen evolution reaction. *Coord. Chem. Rev.* **424**, 213488 (2020). <https://doi.org/10.1016/j.ccr.2020.213488>
22. H. Sun, Z. Yan, F. Liu, W. Xu, F. Cheng et al., Self-supported transition-metal-based electrocatalysts for hydrogen and oxygen evolution. *Adv. Mater.* **32**(3), 1806326 (2020). <https://doi.org/10.1002/adma.201806326>
23. B. You, Y. Sun, Innovative strategies for electrocatalytic water splitting. *Acc. Chem. Res.* **51**(7), 1571–1580 (2018). <https://doi.org/10.1021/acs.accounts.8b00002>
24. J. Yin, J. Jin, H. Lin, Z. Yin, J. Li et al., Optimized metal chalcogenides for boosting water splitting. *Adv. Sci.* **7**(10), 1903070 (2020). <https://doi.org/10.1002/advs.201903070>
25. J. Hou, Y. Wu, B. Zhang, S. Cao, Z. Li et al., Rational design of nanoarray architectures for electrocatalytic water splitting. *Adv. Funct. Mater.* **29**(20), 1808367 (2019). <https://doi.org/10.1002/adfm.201808367>
26. Q. Shi, C. Zhu, D. Du, Y. Lin, Robust noble metal-based electrocatalysts for oxygen evolution reaction. *Chem. Soc. Rev.* **48**(12), 3181–3192 (2019). <https://doi.org/10.1039/c8cs00671g>
27. T. Kwon, T. Kim, Y. Son, K. Lee, Dopants in the design of noble metal nanoparticle electrocatalysts and their effect on surface energy and coordination chemistry at the nanocrystal surface. *Adv. Energy Mater.* **11**(22), 2100265 (2021). <https://doi.org/10.1002/aenm.202100265>
28. Z. Chen, X. Duan, W. Wei, S. Wang, B.J. Ni, Iridium-based nanomaterials for electrochemical water splitting. *Nano Energy* **78**, 105270–105297 (2020). <https://doi.org/10.1016/j.nanoen.2020.105270>
29. J.S. Kim, B. Kim, H. Kim, K. Kang, Recent progress on multimetal oxide catalysts for the oxygen evolution reaction. *Adv. Energy Mater.* **8**(11), 1702774 (2018). <https://doi.org/10.1002/aenm.201702774>
30. C. Xiao, B.A. Lu, P. Xue, N. Tian, Z. Zhou et al., High-index-facet- and high-surface-energy nanocrystals of metals and metal oxides as highly efficient catalysts. *Joule* **4**(12), 2562–2598 (2020). <https://doi.org/10.1016/j.joule.2020.10.002>
31. L. Tian, X. Zhai, X. Wang, J. Li, Z. Li, Advances in manganese-based oxides for oxygen evolution reaction. *J. Mater. Chem. A* **8**(29), 14400–14414 (2020). <https://doi.org/10.1039/d0ta05116k>
32. F. Song, L. Bai, A. Moysiadou, S. Lee, C. Hu et al., Transition metal oxides as electrocatalysts for the oxygen evolution reaction in alkaline solutions: an application-inspired renaissance. *J. Am. Chem. Soc.* **140**(25), 7748–7759 (2018). <https://doi.org/10.1021/jacs.8b04546>
33. S. Anantharaj, S.R. Ede, K. Sakthikumar, K. Karthick, S. Mishra et al., Recent trends and perspectives in electrochemical water splitting with an emphasis on sulfide, selenide, and

- phosphide catalysts of Fe Co, and Ni: a review. *ACS Catal.* **6**(12), 8069–8097 (2016). <https://doi.org/10.1021/acscatal.6b02479>
34. Y. Li, Z. Dong, L. Jiao, Multifunctional transition metal-based phosphides in energy-related electrocatalysis. *Adv. Energy Mater.* **10**(11), 1902104 (2019). <https://doi.org/10.1002/aenm.201902104>
35. Z. Pu, T. Liu, I.S. Amiinu, R. Cheng, P. Wang et al., Transition-metal phosphides: activity origin, energy-related electrocatalysis applications, and synthetic strategies. *Adv. Funct. Mater.* **30**(45), 2004009 (2020). <https://doi.org/10.1002/adfm.202004009>
36. Y. Shi, B. Zhang, Recent advances in transition metal phosphide nanomaterials: synthesis and applications in hydrogen evolution reaction. *Chem. Soc. Rev.* **45**(6), 1529–1541 (2016). <https://doi.org/10.1039/c5cs00434a>
37. Y. Wang, B. Kong, D. Zhao, H. Wang, C. Selomulya, Strategies for developing transition metal phosphides as heterogeneous electrocatalysts for water splitting. *Nano Today* **15**, 26–55 (2017). <https://doi.org/10.1016/j.nantod.2017.06.006>
38. Y. Zhang, Q. Zhou, J. Zhu, Q. Yan, S.X. Dou et al., Nanostructured metal chalcogenides for energy storage and electrocatalysis. *Adv. Funct. Mater.* **27**(35), 1702317–1702350 (2017). <https://doi.org/10.1002/adfm.201702317>
39. X. Wu, H. Zhang, J. Zhang, X.W. Lou, Recent advances on transition metal dichalcogenides for electrochemical energy conversion. *Adv. Mater.* **33**, 2008376 (2021). <https://doi.org/10.1002/adma.202008376>
40. M.R. Gao, Y.F. Xu, J. Jiang, S.H. Yu, Nanostructured metal chalcogenides: synthesis, modification, and applications in energy conversion and storage devices. *Chem. Soc. Rev.* **42**(7), 2986–3017 (2013). <https://doi.org/10.1039/c2cs35310e>
41. D. Kong, J.J. Cha, H. Wang, H.R. Lee, Y. Cui, First-row transition metal dichalcogenide catalysts for hydrogen evolution reaction. *Energy Environ. Sci.* **6**(12), 3553–3558 (2013). <https://doi.org/10.1039/c3ee42413h>
42. P. Yu, F. Wang, T.A. Shifa, X. Zhan, X. Lou et al., Earth abundant materials beyond transition metal dichalcogenides: a focus on electrocatalyzing hydrogen evolution reaction. *Nano Energy* **58**, 244–276 (2019). <https://doi.org/10.1016/j.nanoen.2019.01.017>
43. C.C. Hou, Q. Xu, Metal-organic frameworks for energy. *Adv. Energy Mater.* **9**(23), 1801307 (2018). <https://doi.org/10.1002/aenm.201801307>
44. Z. Li, R. Gao, M. Feng, Y.P. Deng, D. Xiao et al., Modulating metal-organic frameworks as advanced oxygen electrocatalysts. *Adv. Energy Mater.* **11**(16), 2003291 (2021). <https://doi.org/10.1002/aenm.202003291>
45. J. Du, F. Li, L. Sun, Metal-organic frameworks and their derivatives as electrocatalysts for the oxygen evolution reaction. *Chem. Soc. Rev.* **50**(4), 2663–2695 (2021). <https://doi.org/10.1039/d0cs01191f>
46. L. Jiao, J.Y.R. Seow, W.S. Skinner, Z.U. Wang, H.L. Jiang, Metal-organic frameworks: structures and functional applications. *Mater. Today* **27**, 43–68 (2019). <https://doi.org/10.1016/j.mattod.2018.10.038>
47. N. Jiang, B. You, M. Sheng, Y. Sun, Electrodeposited cobalt–phosphorous-derived films as competent bifunctional catalysts for overall water splitting. *Angew. Chem. Int. Ed.* **54**(21), 6251–6254 (2015). <https://doi.org/10.1002/anie.201501616>
48. B. You, Y. Zhang, Y. Jiao, K. Davey, S.Z. Qiao, Negative charging of transition-metal phosphides via strong electronic coupling for destabilization of alkaline water. *Angew. Chem. Int. Ed.* **58**(34), 11796–11800 (2019). <https://doi.org/10.1002/anie.201906683>
49. B. You, X. Liu, G. Hu, S. Gul, J. Yano et al., Universal surface engineering of transition metals for superior electrocatalytic hydrogen evolution in neutral water. *J. Am. Chem. Soc.* **139**(35), 12283–12290 (2017). <https://doi.org/10.1021/jacs.7b06434>
50. J. Shan, Y. Zheng, B. Shi, K. Davey, S.Z. Qiao, Regulating electrocatalysts via surface and interface engineering for acidic water electrooxidation. *ACS Energy Lett.* **4**(11), 2719–2730 (2019). <https://doi.org/10.1021/acsenergylett.9b01758>
51. Q. Shao, P. Wang, X. Huang, Opportunities and challenges of interface engineering in bimetallic nanostructure for enhanced electrocatalysis. *Adv. Funct. Mater.* **29**(3), 1806419 (2019). <https://doi.org/10.1002/adfm.201806419>
52. Z. Yin, X. Liu, S. Chen, T. Ma, Y. Li, Interface engineering and anion engineering of Mo-based heterogeneous electrocatalysts for hydrogen evolution reaction. *Energy Environ. Mater.* (2022). <https://doi.org/10.1002/eem2.12310>
53. Y. Huang, L.W. Jiang, B.Y. Shi, K.M. Ryan, J.J. Wang, Highly efficient oxygen evolution reaction enabled by phosphorus doping of the Fe electronic structure in iron-nickel selenide nanosheets. *Adv. Sci.* **8**(18), 2101775 (2021). <https://doi.org/10.1002/advs.202101775>
54. K. Zhao, W. Yang, L. Li, S. Wang, L. Wang et al., Discharge induced-activation of phosphorus-doped nickel oxyhydroxide for oxygen evolution reaction. *Chem. Eng. J.* **435**, 135049–135057 (2022). <https://doi.org/10.1016/j.cej.2022.135049>
55. H. Sun, W. Jung, Recent advances in doped ruthenium oxides as high-efficiency electrocatalysts for the oxygen evolution reaction. *J. Mater. Chem. A* **9**(28), 15506–15521 (2021). <https://doi.org/10.1039/d1ta03452a>
56. S. Huang, Z. Jin, P. Ning, C. Gao, Y. Wu et al., Synergistically modulating electronic structure of Ni₂S hierarchical architectures by phosphorus doping and sulfur-vacancies defect engineering enables efficient electrocatalytic water splitting. *Chem. Eng. J.* **420**, 127630–127641 (2021). <https://doi.org/10.1016/j.cej.2020.127630>
57. Y. Zhu, X. Liu, S. Jin, H. Chen, W. Lee et al., Anionic defect engineering of transition metal oxides for oxygen reduction and evolution reactions. *J. Mater. Chem. A* **7**(11), 5875–5897 (2019). <https://doi.org/10.1039/c8ta12477a>
58. C. Xie, D. Yan, W. Chen, Y. Zou, R. Chen et al., Insight into the design of defect electrocatalysts: from electronic structure

- to adsorption energy. *Mater. Today* **31**, 47–68 (2019). <https://doi.org/10.1016/j.mattod.2019.05.021>
59. P. Wang, Y. Luo, G. Zhang, Z. Chen, H. Ranganathan et al., Interface engineering of $\text{Ni}_x\text{S}_y@\text{MnO}_x\text{H}_y$ nanorods to efficiently enhance overall-water-splitting activity and stability. *Nano-Micro Lett.* **14**(1), 120–136 (2022). <https://doi.org/10.1007/s40820-022-00860-2>
60. H. Xu, H. Shang, C. Wang, Y. Du, Surface and interface engineering of noble-metal-free electrocatalysts for efficient overall water splitting. *Coord. Chem. Rev.* **418**, 213374 (2020). <https://doi.org/10.1016/j.ccr.2020.213374>
61. C.-F. Li, L.-J. Xie, J.-W. Zhao, L.-F. Gu, J.-Q. Wu et al., Interfacial electronic modulation by $\text{Fe}_2\text{O}_3/\text{NiFe}$ -LDHs heterostructures for efficient oxygen evolution at high current density. *Appl. Catal. B* **306**, 121097 (2022). <https://doi.org/10.1016/j.apcatb.2022.121097>
62. R. Li, Y. Li, P. Yang, P. Ren, D. Wang et al., Synergistic interface engineering and structural optimization of non-noble metal telluride-nitride electrocatalysts for sustainably overall seawater electrolysis. *Appl. Catal. B* **318**, 121834 (2022). <https://doi.org/10.1016/j.apcatb.2022.121834>
63. L. Zhang, C. Lu, F. Ye, R. Pang, Y. Liu et al., Selenic acid etching assisted vacancy engineering for designing highly active electrocatalysts toward the oxygen evolution reaction. *Adv. Mater.* **33**(14), 2007523 (2021). <https://doi.org/10.1002/adma.202007523>
64. L. Zhang, C. Lu, F. Ye, Z. Wu, Y. Wang et al., Vacancies boosting strategy enabling enhanced oxygen evolution activity in a library of novel amorphous selenite electrocatalysts. *Appl. Catal. B* **284**, 119758 (2021). <https://doi.org/10.1016/j.apcatb.2020.119758>
65. H. Jiang, L. Yan, S. Zhang, Y. Zhao, X. Yang et al., Electrochemical surface restructuring of phosphorus-doped carbon@MoP electrocatalysts for hydrogen evolution. *Nano-Micro Lett.* **13**(1), 215 (2021). <https://doi.org/10.1007/s40820-021-00737-w>
66. R. Li, H. Xu, P. Yang, D. Wang, Y. Li et al., Synergistic interfacial and doping engineering of heterostructured $\text{NiCo}(\text{OH})_x\text{-Co}_y\text{W}$ as an efficient alkaline hydrogen evolution electrocatalyst. *Nano-Micro Lett.* **13**(1), 120 (2021). <https://doi.org/10.1007/s40820-021-00639-x>
67. G. Qian, J. Chen, T. Yu, J. Liu, L. Luo et al., Three-phase heterojunction nimo-based nano-needle for water splitting at industrial alkaline condition. *Nano-Micro Lett.* **14**(1), 20 (2021). <https://doi.org/10.1007/s40820-021-00744-x>
68. G. Qian, J. Chen, T. Yu, L. Luo, S. Yin, N-doped graphene-decorated NiCo alloy coupled with mesoporous NiCoMoO nano-sheet heterojunction for enhanced water electrolysis activity at high current density. *Nano-Micro Lett.* **13**(1), 77 (2021). <https://doi.org/10.1007/s40820-021-00607-5>
69. Z. Wu, T. Liao, S. Wang, J.A. Mudiyansele, A.S. Micallef et al., Conversion of catalytically inert 2d bismuth oxide nanosheets for effective electrochemical hydrogen evolution reaction catalysis via oxygen vacancy concentration modulation. *Nano-Micro Lett.* **14**(1), 90 (2022). <https://doi.org/10.1007/s40820-022-00832-6>
70. H. Wu, T. Yang, Y. Du, L. Shen, G.W. Ho, Identification of facet-governing reactivity in hematite for oxygen evolution. *Adv. Mater.* **30**(52), 1804341 (2018). <https://doi.org/10.1002/adma.201804341>
71. K.A. Stoerzinger, L. Qiao, M.D. Biegalski, Y. Shao-Horn, Orientation-dependent oxygen evolution activities of rutile IrO_2 and RuO_2 . *J. Phys. Chem. Lett.* **5**(10), 1636–1641 (2014). <https://doi.org/10.1021/jz500610u>
72. S. Wang, G. Liu, L. Wang, Crystal facet engineering of photoelectrodes for photoelectrochemical water splitting. *Chem. Rev.* **119**(8), 5192–5247 (2019). <https://doi.org/10.1021/acs.chemrev.8b00584>
73. H. Hu, B. Chang, X. Sun, Q. Huo, B. Zhang et al., Intrinsic properties of macroscopically tuned gallium nitride single-crystalline facets for electrocatalytic hydrogen evolution. *Chem. Eur. J.* **25**(44), 10420–10426 (2019). <https://doi.org/10.1002/chem.201901395>
74. M. Peng, J. Huang, Y. Zhu, H. Zhou, Z. Hu et al., Structural anisotropy determining the oxygen evolution mechanism of strongly correlated perovskite nickelate electrocatalyst. *ACS Sustain. Chem. Eng.* **9**(11), 4262–4270 (2021). <https://doi.org/10.1021/acssuschemeng.1c00596>
75. B. Owens-Baird, J.P.S. Sousa, Y. Ziouani, D.Y. Petrovykh, N.A. Zarkevich et al., Crystallographic facet selective HER catalysis: exemplified in FeP and NiP_2 single crystals. *Chem. Sci.* **11**(19), 5007–5016 (2020). <https://doi.org/10.1039/d0sc00676a>
76. C. Zhang, S. Yang, D. Rao, Theoretical study the component and facet dependence of HER performance on nickel phosphides surfaces. *Int. J. Hydrog. Energy* **47**(5), 2992–3000 (2021). <https://doi.org/10.1016/j.ijhydene.2021.10.254>
77. L. Yang, K. Zhang, H. Chen, L. Shi, X. Liang et al., An ultrathin two-dimensional iridium-based perovskite oxide electrocatalyst with highly efficient 001 facets for acidic water oxidation. *J. Energy Chem.* **66**, 619–627 (2022). <https://doi.org/10.1016/j.jechem.2021.09.016>
78. M. Risch, D.M. Morales, J. Villalobos, D. Antipin, What X-ray absorption spectroscopy can tell us about the active state of earth-abundant electrocatalysts for the oxygen evolution reaction. *Angew. Chem. Int. Ed.* **61**(50), e202211949 (2022). <https://doi.org/10.1002/anie.202211949>
79. C. Wu, Y. Sun, Z. Yang, J. Hu, T.-Y. Ding et al., Tuning the spin state of Co^{3+} by crystal facet engineering for enhancing the oxygen evolution reaction activity. *Chem. Mater.* **34**(23), 10509–10516 (2022). <https://doi.org/10.1021/acs.chemmater.2c02574>
80. J. Wan, D. Liu, H. Xiao, H. Rong, S. Guan et al., Facet engineering in metal organic frameworks to improve their electrochemical activity for water oxidation. *Chem. Commun.* **56**(31), 4316–4319 (2020). <https://doi.org/10.1039/d0cc00700e>
81. T. Wu, M.L. Stone, M.J. Shearer, M.J. Stolt, I.A. Guzei et al., Crystallographic facet dependence of the hydrogen evolution

- reaction on CoPS: theory and experiments. *ACS Catal.* **8**(2), 1143–1152 (2018). <https://doi.org/10.1021/acscatal.7b03167>
82. Y. Liang, Y. Yang, K. Xu, T. Yu, S. Yao et al., Crystal plane dependent electrocatalytic performance of NiS₂ nanocrystals for hydrogen evolution reaction. *J. Catal.* **381**, 63–69 (2020). <https://doi.org/10.1016/j.jcat.2019.10.038>
83. T. Maiyalagan, K.R. Chemelewski, A. Manthiram, Role of the morphology and surface planes on the catalytic activity of spinel LiMn_{1.5}Ni_{0.5}O₄ for oxygen evolution reaction. *ACS Catal.* **4**(2), 421–425 (2014). <https://doi.org/10.1021/cs400981d>
84. H. Zhao, L. Yu, L. Zhang, L. Dai, F. Yao et al., Facet engineering in ultrathin two-dimensional NiFe metal-organic frameworks by coordination modulation for enhanced electrocatalytic water oxidation. *ACS Sustain. Chem. Eng.* **9**(32), 10892–10901 (2021). <https://doi.org/10.1021/acssuschemeng.1c03385>
85. T. Odedairo, X. Yan, X. Yao, K.K. Ostrikov, Z. Zhu, Hexagonal sphericon hematite with high performance for water oxidation. *Adv. Mater.* **29**(46), 1703792 (2017). <https://doi.org/10.1002/adma.201703792>
86. Y. Shan, X. Deng, X. Lu, C. Gao, Y. Li et al., Surface facets dependent oxygen evolution reaction of single Cu₂O nanoparticles. *Chin. Chem. Lett.* **33**, 5158–5161 (2022). <https://doi.org/10.1016/j.cclet.2022.03.010>
87. S. Sun, X. Zhang, J. Cui, Q. Yang, S. Liang, High-index faceted metal oxide micro-/nanostructures: a review on their characterization, synthesis and applications. *Nanoscale* **11**(34), 15739–15762 (2019). <https://doi.org/10.1039/c9nr05107d>
88. Y. Zhang, W. Xie, J. Ma, L. Chen, C. Chen et al., Active facet determination of layered double hydroxide for oxygen evolution reaction. *J. Energy Chem.* **60**, 127–134 (2021). <https://doi.org/10.1016/j.jechem.2020.12.038>
89. J. Noh, H. Li, O.I. Osman, S.G. Aziz, P. Winget et al., Impact of hydroxylation and hydration on the reactivity of α -Fe₂O₃ (0001) and (102) surfaces under environmental and electrochemical conditions. *Adv. Energy Mater.* **8**(21), 1800545 (2018). <https://doi.org/10.1002/aenm.201800545>
90. Z. Liu, C. Yuan, F. Teng, Crystal facets-predominated oxygen evolution reaction activity of earth abundant CoMoO₄ electrocatalyst. *J. Alloys Compd.* **781**, 460–466 (2019). <https://doi.org/10.1016/j.jallcom.2018.12.026>
91. J. Yang, G. Ning, L. Yu, Y. Wang, C. Luan et al., Morphology controllable synthesis of PtNi concave nanocubes enclosed by high-index facets supported on porous graphene for enhanced hydrogen evolution reaction. *J. Mater. Chem. A* **7**(30), 17790–17796 (2019). <https://doi.org/10.1039/c9ta03442k>
92. L.L. Feng, G. Yu, Y. Wu, G.D. Li, H. Li et al., High-index faceted Ni₃S₂ nanosheet arrays as highly active and ultrastable electrocatalysts for water splitting. *J. Am. Chem. Soc.* **137**(44), 14023–14026 (2015). <https://doi.org/10.1021/jacs.5b08186>
93. C. Zhang, F. Zheng, Z. Zhang, D. Xiang, C. Cheng et al., Fabrication of hollow pompon-like Co₃O₄ nanostructures with rich defects and high-index facet exposure for enhanced oxygen evolution catalysis. *J. Mater. Chem. A* **7**(15), 9059–9067 (2019). <https://doi.org/10.1039/c9ta00330d>
94. Z. Kou, K. Xi, Z. Pu, S. Mu, Constructing carbon-cohered high-index (222) faceted tantalum carbide nanocrystals as a robust hydrogen evolution catalyst. *Nano Energy* **36**, 374–380 (2017). <https://doi.org/10.1016/j.nanoen.2017.04.057>
95. L. Li, C. Sun, B. Shang, Q. Li, J. Lei et al., Tailoring the facets of Ni₃S₂ as a bifunctional electrocatalyst for high-performance overall water-splitting. *J. Mater. Chem. A* **7**(30), 18003–18011 (2019). <https://doi.org/10.1039/c9ta05578a>
96. R. Wei, M. Fang, G. Dong, C. Lan, L. Shu et al., High-index faceted porous Co₃O₄ nanosheets with oxygen vacancies for highly efficient water oxidation. *ACS Appl. Mater. Interfaces* **10**(8), 7079–7086 (2018). <https://doi.org/10.1021/acsami.7b18208>
97. J. Xiao, S. Liu, N. Tian, Z.Y. Zhou, H.X. Liu et al., Synthesis of convex hexoctahedral Pt micro/nanocrystals with high-index facets and electrochemistry-mediated shape evolution. *J. Am. Chem. Soc.* **135**(50), 18754–18757 (2013). <https://doi.org/10.1021/ja410583b>
98. B. Jiang, Y. Qiu, D. Tian, Y. Zhang, X. Song et al., Crystal facet engineering induced active tin dioxide nanocatalysts for highly stable lithium–sulfur batteries. *Adv. Energy Mater.* **11**(48), 2102995 (2021). <https://doi.org/10.1002/aenm.202102995>
99. G. Liu, J.C. Yu, G.Q. Lu, H.M. Cheng, Crystal facet engineering of semiconductor photocatalysts: motivations, advances and unique properties. *Chem. Commun.* **47**(24), 6763–6783 (2011). <https://doi.org/10.1039/c1cc10665a>
100. X. Zou, Y. Zhang, Noble metal-free hydrogen evolution catalysts for water splitting. *Chem. Soc. Rev.* **44**(15), 5148–5180 (2015). <https://doi.org/10.1039/c4cs00448e>
101. J. Wang, H. Kong, J. Zhang, Y. Hao, Z. Shao et al., Carbon-based electrocatalysts for sustainable energy applications. *Prog. Mater. Sci.* **116**, 100717–100770 (2021). <https://doi.org/10.1016/j.pmatsci.2020.100717>
102. B. You, S.Z. Qiao, Destabilizing alkaline water with 3d-metal (oxy)(hydr)oxides for improved hydrogen evolution. *Chem. Eur. J.* **27**(2), 553–564 (2021). <https://doi.org/10.1002/chem.202002503>
103. L. Sun, Q. Luo, Z. Dai, F. Ma, Material libraries for electrocatalytic overall water splitting. *Coord. Chem. Rev.* **444**, 214049 (2021). <https://doi.org/10.1016/j.ccr.2021.214049>
104. X. Liu, P. Wang, X. Liang, Q. Zhang, Z. Wang et al., Research progress and surface/interfacial regulation methods for electrophotocatalytic hydrogen production from water splitting. *Mater. Today Energy* **18**, 100524–100555 (2020). <https://doi.org/10.1016/j.mtener.2020.100524>
105. J. Wei, M. Zhou, A. Long, Y. Xue, H. Liao et al., Heterostructured electrocatalysts for hydrogen evolution reaction under alkaline conditions. *Nano-Micro Lett.* **10**(4), 75–89 (2018). <https://doi.org/10.1007/s40820-018-0229-x>
106. Y. Xu, C. Wang, Y. Huang, J. Fu, Recent advances in electrocatalysts for neutral and large-current-density water



- electrolysis. *Nano Energy* **80**, 105545 (2021). <https://doi.org/10.1016/j.nanoen.2020.105545>
107. D. Strmcnik, P.P. Lopes, B. Genorio, V.R. Stamenkovic, N.M. Markovic, Design principles for hydrogen evolution reaction catalyst materials. *Nano Energy* **29**, 29–36 (2016). <https://doi.org/10.1016/j.nanoen.2016.04.017>
108. S. Chandrasekaran, D. Ma, Y. Ge, L. Deng, C. Bowen et al., Electronic structure engineering on two-dimensional (2D) electrocatalytic materials for oxygen reduction, oxygen evolution, and hydrogen evolution reactions. *Nano Energy* **77**, 105080–1050123 (2020). <https://doi.org/10.1016/j.nanoen.2020.105080>
109. C.G. Morales-Guio, L.A. Stern, X. Hu, Nanostructured hydrotreating catalysts for electrochemical hydrogen evolution. *Chem. Soc. Rev.* **43**(18), 6555–6569 (2014). <https://doi.org/10.1039/c3cs60468c>
110. R. Miao, B. Dutta, S. Sahoo, J. He, W. Zhong et al., Mesoporous iron sulfide for highly efficient electrocatalytic hydrogen evolution. *J. Am. Chem. Soc.* **139**(39), 13604–13607 (2017). <https://doi.org/10.1021/jacs.7b07044>
111. N.T. Suen, S.F. Hung, Q. Quan, N. Zhang, Y.J. Xu et al., Electrocatalysis for the oxygen evolution reaction: recent development and future perspectives. *Chem. Soc. Rev.* **46**(2), 337–365 (2017). <https://doi.org/10.1039/c6cs00328a>
112. G. Fu, X. Kang, Y. Zhang, X. Yang, L. Wang et al., Coordination effect-promoted durable Ni(OH)₂ for energy-saving hydrogen evolution from water/methanol co-electrocatalysis. *Nano-Micro Lett.* **14**(1), 200 (2022). <https://doi.org/10.1007/s40820-022-00940-3>
113. A. Radwan, H. Jin, D. He, S. Mu, Design engineering, synthesis protocols, and energy applications of MOF-derived electrocatalysts. *Nano-Micro Lett.* **13**(1), 132 (2021). <https://doi.org/10.1007/s40820-021-00656-w>
114. J. Li, Oxygen evolution reaction in energy conversion and storage: design strategies under and beyond the energy scaling relationship. *Nano-Micro Lett.* **14**(1), 112–143 (2022). <https://doi.org/10.1007/s40820-022-00857-x>
115. N. Zhang, X. Feng, D. Rao, X. Deng, L. Cai et al., Lattice oxygen activation enabled by high-valence metal sites for enhanced water oxidation. *Nat. Commun.* **11**(1), 4066 (2020). <https://doi.org/10.1038/s41467-020-17934-7>
116. F. Chen, Z. Wu, Z. Adler, H. Wang, Stability challenges of electrocatalytic oxygen evolution reaction: from mechanistic understanding to reactor design. *Joule* **5**(7), 1704–1731 (2021). <https://doi.org/10.1016/j.joule.2021.05.005>
117. L. Gao, X. Cui, C.D. Sewell, J. Li, Z. Lin, Recent advances in activating surface reconstruction for the high-efficiency oxygen evolution reaction. *Chem. Soc. Rev.* **50**(15), 8428–8469 (2021). <https://doi.org/10.1039/d0cs00962h>
118. N. Zhang, Y. Chai, Lattice oxygen redox chemistry in solid-state electrocatalysts for water oxidation. *Energy Environ. Sci.* **14**(9), 4647–4671 (2021). <https://doi.org/10.1039/d1ee01277k>
119. Z. Chen, X. Duan, W. Wei, S. Wang, B.J. Ni, Electrocatalysts for acidic oxygen evolution reaction: achievements and perspectives. *Nano Energy* **78**, 105392–105421 (2020). <https://doi.org/10.1016/j.nanoen.2020.105392>
120. D. Liu, P. Zhou, H. Bai, H. Ai, X. Du et al., Development of perovskite oxide-based electrocatalysts for oxygen evolution reaction. *Small* **17**(43), 2101605 (2021). <https://doi.org/10.1002/sml.202101605>
121. H. Xu, J. Yuan, G. He, H. Chen, Current and future trends for spinel-type electrocatalysts in electrocatalytic oxygen evolution reaction. *Coord. Chem. Rev.* **475**, 214869 (2023). <https://doi.org/10.1016/j.ccr.2022.214869>
122. H. Sun, X. Xu, Y. Song, W. Zhou, Z. Shao, Designing high-valence metal sites for electrochemical water splitting. *Adv. Funct. Mater.* **31**(16), 2009779 (2021). <https://doi.org/10.1002/adfm.202009779>
123. L. An, C. Wei, M. Lu, H. Liu, Y. Chen et al., Recent development of oxygen evolution electrocatalysts in acidic environment. *Adv. Mater.* **33**(20), 2006328 (2021). <https://doi.org/10.1002/adma.202006328>
124. K. Zhang, R. Zou, Advanced transition metal-based OER electrocatalysts: current status, opportunities, and challenges. *Small* **17**, 2100129 (2021). <https://doi.org/10.1002/sml.202100129>
125. H. Dau, C. Limberg, T. Reier, M. Risch, S. Roggan et al., The mechanism of water oxidation: from electrolysis via homogeneous to biological catalysis. *ChemCatChem* **2**(7), 724–761 (2010). <https://doi.org/10.1002/cctc.201000126>
126. I.C. Man, H. Su, F. Calle-Vallejo, H.A. Hansen, J.I. Martínez et al., Universality in oxygen evolution electrocatalysis on oxide surfaces. *ChemCatChem* **3**(7), 1159–1165 (2011). <https://doi.org/10.1002/cctc.201000397>
127. R. Gao, M. Deng, Q. Yan, Z. Fang, L. Li et al., Structural variations of metal oxide-based electrocatalysts for oxygen evolution reaction. *Small Methods* **5**(12), 2100834 (2021). <https://doi.org/10.1002/smt.202100834>
128. J. Song, C. Wei, Z.F. Huang, C. Liu, L. Zeng et al., A review on fundamentals for designing oxygen evolution electrocatalysts. *Chem. Soc. Rev.* **49**(7), 2196–2214 (2020). <https://doi.org/10.1039/c9cs00607a>
129. A. Kulkarni, S. Siahrostami, A. Patel, J.K. Nørskov, Understanding catalytic activity trends in the oxygen reduction reaction. *Chem. Rev.* **118**(5), 2302–2312 (2018). <https://doi.org/10.1021/acs.chemrev.7b00488>
130. T. Guo, L. Li, Z. Wang, Recent development and future perspectives of amorphous transition metal-based electrocatalysts for oxygen evolution reaction. *Adv. Energy Mater.* **12**, 2200827 (2022). <https://doi.org/10.1002/aenm.202200827>
131. H.N. Nong, T. Reier, H. Oh, M. Gliech, P. Paciok et al., A unique oxygen ligand environment facilitates water oxidation in hole-doped IrNiO_x core-shell electrocatalysts. *Nat. Catal.* **1**(11), 841–851 (2018). <https://doi.org/10.1038/s41929-018-0153-y>
132. Y. Zhang, X. Zhu, G. Zhang, P. Shi, A. Wang, Rational catalyst design for oxygen evolution under acidic conditions: strategies toward enhanced electrocatalytic performance. *J.*

- Mater. Chem. A **9**(10), 5890–5914 (2021). <https://doi.org/10.1039/d0ta11982b>
133. Z. Lei, T. Wang, B. Zhao, W. Cai, Y. Liu et al., Recent progress in electrocatalysts for acidic water oxidation. *Adv. Energy Mater.* **10**(23), 2000478 (2020). <https://doi.org/10.1002/aenm.202000478>
134. Y.-C. Zhang, C. Han, J. Gao, L. Pan, J. Wu et al., NiCo-based electrocatalysts for the alkaline oxygen evolution reaction: a review. *ACS Catal.* **11**(20), 12485–12509 (2021). <https://doi.org/10.1021/acscatal.1c03260>
135. J. Yu, F. Yu, M. Yuen, C. Wang, Two-dimensional layered double hydroxides as a platform for electrocatalytic oxygen evolution. *J. Mater. Chem. A* **9**(15), 9389–9430 (2021). <https://doi.org/10.1039/d0ta11910e>
136. C. Wei, Z.J. Xu, The comprehensive understanding of 10 mA $\text{cm}_{\text{geo}}^{-2}$ as an evaluation parameter for electrochemical water splitting. *Small Methods* **2**(11), 1800168 (2018). <https://doi.org/10.1002/smt.201800168>
137. C.C. McCrory, S. Jung, I.M. Ferrer, S.M. Chatman, J.C. Peters et al., Benchmarking hydrogen evolving reaction and oxygen evolving reaction electrocatalysts for solar water splitting devices. *J. Am. Chem. Soc.* **137**(13), 4347–4357 (2015). <https://doi.org/10.1021/ja510442p>
138. F. Liu, C. Shi, X. Guo, Z. He, L. Pan et al., Rational design of better hydrogen evolution electrocatalysts for water splitting: a review. *Adv. Sci.* **9**, 2200307 (2022). <https://doi.org/10.1002/advs.202200307>
139. C. Wang, B. Yan, Z. Chen, B. You, T. Liao et al., Recent advances in carbon substrate supported nonprecious nanoarrays for electrocatalytic oxygen evolution. *J. Mater. Chem. A* **9**(46), 25773–25795 (2021). <https://doi.org/10.1039/d1ta08039c>
140. Z.P. Wu, X.F. Lu, S.Q. Zang, X.W. Lou, Non-noble-metal-based electrocatalysts toward the oxygen evolution reaction. *Adv. Funct. Mater.* **30**(15), 1910274 (2020). <https://doi.org/10.1002/adfm.201910274>
141. Z.Y. Yu, Y. Duan, X.Y. Feng, X. Yu, M.R. Gao et al., Clean and affordable hydrogen fuel from alkaline water splitting: past, recent progress, and future prospects. *Adv. Mater.* **33**, 2007100 (2021). <https://doi.org/10.1002/adma.202007100>
142. N.T. Thanh, N. Maclean, S. Mahiddine, Mechanisms of nucleation and growth of nanoparticles in solution. *Chem. Rev.* **114**(15), 7610–7630 (2014). <https://doi.org/10.1021/cr400544s>
143. J.J.D. Yoreo, P.G. Vekilov, Principles of crystal nucleation and growth. *Rev. Mineral. Geochem.* **54**(1), 57–93 (2003). <https://doi.org/10.2113/0540057>
144. Q. Zhang, W. Li, L.P. Wen, J. Chen, Y. Xia, Controlling the shapes of silver nanocrystals with different capping agents. *J. Am. Chem. Soc.* **132**, 8552–8553 (2010). <https://doi.org/10.1002/chem.201000341>
145. H.G. Yang, C.H. Sun, S.Z. Qiao, J. Zou, G. Liu et al., Anatase TiO_2 single crystals with a large percentage of reactive facets. *Nature* **453**, 638–641 (2008). <https://doi.org/10.1038/nature06964>
146. G. Liu, H.G. Yang, X. Wang, L. Cheng, J. Pan et al., Visible light responsive nitrogen doped anatase TiO_2 sheets with dominant 001 facets derived from TiN. *J. Am. Chem. Soc.* **131**(36), 12868–12869 (2009). <https://doi.org/10.1021/ja903463q>
147. H.G. Yang, G. Liu, S.Z. Qiao, C.H. Sun, Y.G. Jin et al., Solvothermal synthesis and photoreactivity of anatase TiO_2 nanosheets with dominant 001 facets. *J. Am. Chem. Soc.* **131**(11), 4078–4083 (2009). <https://doi.org/10.1021/ja808790p>
148. X. Han, Q. Kuang, M. Jin, Z. Xie, L. Zheng, Synthesis of titania nanosheets with a high percentage of exposed (001) facets and related photocatalytic properties. *J. Am. Chem. Soc.* **131**, 3152–3153 (2009). <https://doi.org/10.1021/ja8092373>
149. D.F. Zhang, H. Zhang, L. Guo, K. Zheng, X.D. Han et al., Delicate control of crystallographic facet-oriented Cu_2O nanocrystals and the correlated adsorption ability. *J. Mater. Chem.* **19**(29), 5220–5225 (2009). <https://doi.org/10.1039/b816349a>
150. J. Pal, M. Ganguly, C. Mondal, A. Roy, Y. Negishi et al., Crystal-plane-dependent etching of cuprous oxide nanoparticles of varied shapes and their application in visible light photocatalysis. *J. Phys. Chem. C* **117**(46), 24640–24653 (2013). <https://doi.org/10.1021/jp409271r>
151. Y.H. Tsai, C.Y. Chiu, M.H. Huang, Fabrication of diverse Cu_2O nanoframes through face-selective etching. *J. Phys. Chem. C* **117**(46), 24611–24617 (2013). <https://doi.org/10.1021/jp4088018>
152. X. Liu, G. Dong, S. Li, G. Lu, Y. Bi, Direct observation of charge separation on anatase TiO_2 crystals with selectively etched 001 facets. *J. Am. Chem. Soc.* **138**(9), 2917–2920 (2016). <https://doi.org/10.1021/jacs.5b12521>
153. X. Xiao, L. Zou, H. Pang, Q. Xu, Synthesis of micro/nanoscaled metal-organic frameworks and their direct electrochemical applications. *Chem. Soc. Rev.* **49**(1), 301–331 (2020). <https://doi.org/10.1039/c7cs00614d>
154. A. Umemura, S. Diring, S. Furukawa, H. Uehara, T. Tsuruoka et al., Morphology design of porous coordination polymer crystals by coordination modulation. *J. Am. Chem. Soc.* **133**(39), 15506–15513 (2011). <https://doi.org/10.1021/ja204233q>
155. S. Diring, S. Furukawa, Y. Takashima, T. Tsuruoka, S. Kitagawa, Controlled multiscale synthesis of porous coordination polymer in nano/micro regimes. *Chem. Mater.* **22**(16), 4531–4538 (2010). <https://doi.org/10.1021/cm101778g>
156. N. Sikdar, M. Bhogra, U.V. Waghmare, T.K. Maji, Oriented attachment growth of anisotropic meso/nanoscale MOFs: tunable surface area and CO_2 separation. *J. Mater. Chem. A* **5**(39), 20959–20968 (2017). <https://doi.org/10.1039/c7ta02896b>
157. X. Yu, J. Zhao, L.R. Zheng, Y. Tong, M. Zhang et al., Hydrogen evolution reaction in alkaline media: alpha- or beta-nickel hydroxide on the surface of platinum? *ACS Energy Lett.* **3**(1), 237–244 (2017). <https://doi.org/10.1021/acsenenergylett.7b01103>

158. J. Chen, Y. Ha, R. Wang, Y. Liu, H. Xu et al., Inner Co synergizing outer Ru supported on carbon nanotubes for efficient pH-universal hydrogen evolution catalysis. *Nano-Micro Lett.* **14**(1), 186 (2022). <https://doi.org/10.1007/s40820-022-00933-2>
159. H. Liao, D. Zherebetsky, H. Xin, C. Czarnik, P. Ercius et al., Facet development during platinum nanocube growth. *Science* **345**, 6199 (2014). <https://doi.org/10.1126/science.1253149>
160. X. Bao, Y. Gong, X. Zheng, J. Chen, S. Mao et al., Highly performed platinum nanosheets synthesized under in situ reaction conditions for hydrogen generation. *J. Energy Chem.* **51**, 272–279 (2020). <https://doi.org/10.1016/j.jechem.2020.03.064>
161. H. Sun, Q. Zeng, C. Ye, Y. Zhu, F. Chen et al., Pt nanodendrites with (111) crystalline facet as an efficient, stable and pH-universal catalyst for electrochemical hydrogen production. *Chin. Chem. Lett.* **31**(9), 2478–2482 (2020). <https://doi.org/10.1016/j.ccllet.2020.03.032>
162. C.Y. Chan, C.H. Chang, H.Y. Tuan, Synthesis of raspberry-like antimony-platinum (SbPt) nanoparticles as highly active electrocatalysts for hydrogen evolution reaction. *J. Colloid Interface Sci.* **584**, 729–737 (2021). <https://doi.org/10.1016/j.jcis.2020.09.099>
163. T.R. Kuo, Y.C. Lee, H.L. Chou, S. M G, C.Y. Wei et al., Plasmon-enhanced hydrogen evolution on specific facet of silver nanocrystals. *Chem. Mater.* **31**(10), 3722–3728 (2019). <https://doi.org/10.1021/acs.chemmater.9b00652>
164. D. Xu, X. Liu, H. Lv, Y. Liu, S. Zhao et al., Ultrathin palladium nanosheets with selectively controlled surface facets. *Chem. Sci.* **9**(19), 4451–4455 (2018). <https://doi.org/10.1039/c8sc00605a>
165. H. Wang, Y. Xie, H. Cao, Y. Li, L. Li et al., Flower-like nickel phosphide microballs assembled by nanoplates with exposed high-energy (0 0 1) facets: efficient electrocatalyst for the hydrogen evolution reaction. *Chemsuschem* **10**(24), 4899–4908 (2017). <https://doi.org/10.1002/cssc.201701647>
166. Y.H. Chung, K. Gupta, J.H. Jang, H.S. Park, I. Jang et al., Rationalization of electrocatalysis of nickel phosphide nanowires for efficient hydrogen production. *Nano Energy* **26**, 496–503 (2016). <https://doi.org/10.1016/j.nanoen.2016.06.002>
167. E.J. Popczun, J.R. McKone, C.G. Read, A.J. Biacchi, A.M. Wiltrout et al., Nanostructured nickel phosphide as an electrocatalyst for the hydrogen evolution reaction. *J. Am. Chem. Soc.* **135**(25), 9267–9270 (2013). <https://doi.org/10.1021/ja403440e>
168. Q. Yan, X. Chen, T. Wei, G. Wang, M. Zhu et al., Hierarchical edge-rich nickel phosphide nanosheet arrays as efficient electrocatalysts toward hydrogen evolution in both alkaline and acidic conditions. *ACS Sustain. Chem. Eng.* **7**(8), 7804–7811 (2019). <https://doi.org/10.1021/acssuschemeng.8b06861>
169. P. Liu, J.A. Rodriguez, Catalysts for hydrogen evolution from the [NiFe] hydrogenase to the Ni₂P(001) surface: the importance of ensemble effect. *J. Am. Chem. Soc.* **127**, 14871–14878 (2005). <https://doi.org/10.1021/ja0540019>
170. S. Ma, X. Qu, J. Huang, C. Zhang, G. Chen et al., Compositional and crystallographic design of Ni–Co phosphide heterointerfaced nanowires for high-rate, stable hydrogen generation at industry-relevant electrolysis current densities. *Nano Energy* **95**, 106989–106999 (2022). <https://doi.org/10.1016/j.nanoen.2022.106989>
171. L. Liao, C. Cheng, H. Zhou, Y. Qi, D. Li et al., Accelerating pH-universal hydrogen-evolving activity of a hierarchical hybrid of cobalt and dinickel phosphides by interfacial chemical bonds. *Mater. Today Phys.* **22**, 100589–100597 (2022). <https://doi.org/10.1016/j.mtphys.2021.100589>
172. X. Liu, Y. Li, Z. Cao, Z. Yin, T. Ma et al., Current progress of metal sulfides derived from metal-organic frameworks for advanced electrocatalysis: potential electrocatalysts with diverse applications. *J. Mater. Chem. A* **10**(4), 1617–1641 (2022). <https://doi.org/10.1039/d1ta09925f>
173. B. You, Y. Sun, Hierarchically porous nickel sulfide multifunctional superstructures. *Adv. Energy Mater.* **6**(7), 1502333 (2016). <https://doi.org/10.1002/aenm.201502333>
174. W. Zhong, B. Xiao, Z. Lin, Z. Wang, L. Huang et al., RhSe₂: a superior 3D electrocatalyst with multiple active facets for hydrogen evolution reaction in both acid and alkaline solutions. *Adv. Mater.* **33**(9), 2007894 (2021). <https://doi.org/10.1002/adma.202007894>
175. Y. Li, Y. Wang, B. Pattengale, J. Yin, L. An et al., High-index faceted CuFeS₂ nanosheets with enhanced behavior for boosting hydrogen evolution reaction. *Nanoscale* **9**(26), 9230–9237 (2017). <https://doi.org/10.1039/c7nr03182c>
176. Q. Gao, W. Zhang, Z. Shi, L. Yang, Y. Tang, Structural design and electronic modulation of transition-metal-carbide electrocatalysts toward efficient hydrogen evolution. *Adv. Mater.* **31**(2), 1802880 (2019). <https://doi.org/10.1002/adma.201802880>
177. C. Yang, R. Zhao, H. Xiang, J. Wu, W. Zhong et al., Ni-activated transition metal carbides for efficient hydrogen evolution in acidic and alkaline solutions. *Adv. Energy Mater.* **10**(37), 2002260 (2020). <https://doi.org/10.1002/aenm.202002260>
178. H. Xu, J. Wan, H. Zhang, L. Fang, L. Liu et al., A new platinum-like efficient electrocatalyst for hydrogen evolution reaction at all pH: single-crystal metallic interweaved V₈C₇ networks. *Adv. Energy Mater.* **8**(23), 1800575 (2018). <https://doi.org/10.1002/aenm.201800575>
179. J. Theerthagiri, S.J. Lee, A.P. Murthy, J. Madhavan, M.Y. Choi, Fundamental aspects and recent advances in transition metal nitrides as electrocatalysts for hydrogen evolution reaction: a review. *Curr. Opin. Solid State Mater. Sci.* **24**(1), 100805–1008026 (2020). <https://doi.org/10.1016/j.cossms.2020.100805>
180. N. Han, P. Liu, J. Jiang, L. Ai, Z. Shao et al., Recent advances in nanostructured metal nitrides for water splitting. *J. Mater. Chem. A* **6**(41), 19912–19933 (2018). <https://doi.org/10.1039/c8ta06529b>

181. M.S. Balogun, Y. Huang, W. Qiu, H. Yang, H. Ji et al., Updates on the development of nanostructured transition metal nitrides for electrochemical energy storage and water splitting. *Mater. Today* **20**(8), 425–451 (2017). <https://doi.org/10.1016/j.mattod.2017.03.019>
182. M. Xiang, M. Song, Q. Zhu, Y. Yang, C. Hu et al., Inducing two-dimensional single crystal TiN arrays with exposed 111 facets by a novel chemical vapor deposition with excellent electrocatalytic activity for hydrogen evolution reaction. *Chem. Eng. J.* **404**, 126451–126458 (2021). <https://doi.org/10.1016/j.cej.2020.126451>
183. K.A. Adegoke, N.W. Maxakato, Porous metal oxide electrocatalytic nanomaterials for energy conversion: oxygen defects and selection techniques. *Coord. Chem. Rev.* **457**, 214389 (2022). <https://doi.org/10.1016/j.ccr.2021.214389>
184. Y. Zhu, Q. Lin, Y. Zhong, H.A. Tahini, Z. Shao et al., Metal oxide-based materials as an emerging family of hydrogen evolution electrocatalysts. *Energy Environ. Sci.* **13**(10), 3361–3392 (2020). <https://doi.org/10.1039/d0ee02485f>
185. Q. Liu, Z. Chen, Z. Yan, Y. Wang, E. Wang et al., Crystal-plane-dependent activity of spinel Co_3O_4 towards water splitting and the oxygen reduction reaction. *ChemElectroChem* **5**(7), 1080–1086 (2018). <https://doi.org/10.1002/celec.201701302>
186. J. Yu, Q. He, G. Yang, W. Zhou, Z. Shao et al., Recent advances and prospective in ruthenium-based materials for electrochemical water splitting. *ACS Catal.* **9**(11), 9973–10011 (2019). <https://doi.org/10.1021/acscatal.9b02457>
187. L. She, G. Zhao, T. Ma, J. Chen, W. Sun et al., On the durability of iridium-based electrocatalysts toward the oxygen evolution reaction under acid environment. *Adv. Funct. Mater.* **32**(5), 2108465 (2021). <https://doi.org/10.1002/adfm.202108465>
188. K.A. Stoerzinger, O. Diaz-Morales, M. Kolb, R.R. Rao, R. Frydendal et al., Orientation-dependent oxygen evolution on RuO_2 without lattice exchange. *ACS Energy Lett.* **2**(4), 876–881 (2017). <https://doi.org/10.1021/acsenerylett.7b00135>
189. R.R. Rao, M.J. Kolb, L. Giordano, A.F. Pedersen, Y. Katayama et al., Operando identification of site-dependent water oxidation activity on ruthenium dioxide single-crystal surfaces. *Nat. Catal.* **3**(6), 516–525 (2020). <https://doi.org/10.1038/s41929-020-0457-6>
190. Y. Yang, Y. Yu, J. Li, Q. Chen, Y. Du et al., Engineering ruthenium-based electrocatalysts for effective hydrogen evolution reaction. *Nano-Micro Lett.* **13**(1), 160 (2021). <https://doi.org/10.1007/s40820-021-00679-3>
191. F. Xue, X. Guo, B. Min, Y. Si, H. Huang et al., Unconventional high-index facet of iridium boosts oxygen evolution reaction: how the facet matters. *ACS Catal.* **11**(13), 8239–8246 (2021). <https://doi.org/10.1021/acscatal.1c01867>
192. X.F. Zhang, J.S. Li, W.S. You, Z.M. Zhu, $\text{Ag}_2\text{-O}$ with highly exposed 111 crystal facets for efficient electrochemical oxygen evolution: activity and mechanism. *Chin. J. Catal.* **41**(11), 1706–1714 (2020). [https://doi.org/10.1016/s1872-2067\(20\)63574-4](https://doi.org/10.1016/s1872-2067(20)63574-4)
193. J. Wang, J. Xu, Q. Wang, Z. Liu, X. Zhang et al., NiO nanobelts with exposed 110 crystal planes as an efficient electrocatalyst for the oxygen evolution reaction. *Phys. Chem. Chem. Phys.* **24**(10), 6087–6092 (2022). <https://doi.org/10.1039/d1cp05236e>
194. Y. Niu, Y. Yuan, Q. Zhang, F. Chang, L. Yang et al., Morphology-controlled synthesis of metal-organic frameworks derived lattice plane-altered iron oxide for efficient trifunctional electrocatalysts. *Nano Energy* **82**, 105699–105707 (2021). <https://doi.org/10.1016/j.nanoen.2020.105699>
195. W. Wang, Y. Zhang, X. Huang, Y. Bi, Engineering the surface atomic structure of FeVO_4 nanocrystals for use as highly active and stable electrocatalysts for oxygen evolution. *J. Mater. Chem. A* **7**(18), 10949–10953 (2019). <https://doi.org/10.1039/c9ta02922b>
196. X. Peng, Y. Yan, X. Jin, C. Huang, W. Jin et al., Recent advance and perspectives of electrocatalysts based on transition metal selenides for efficient water splitting. *Nano Energy* **78**, 105234–105256 (2020). <https://doi.org/10.1016/j.nanoen.2020.105234>
197. F. Ye, L. Zhang, C. Lu, Z. Bao, Z. Wu et al., Realizing interfacial electron/hole redistribution and superhydrophilic surface through building heterostructural 2 nm $\text{Co}_{0.85}\text{Se-NiSe}$ nanograins for efficient overall water splittings. *Small Methods* **6**(7), 2200459 (2022). <https://doi.org/10.1002/smt.202200459>
198. K. Dang, S. Zhang, X. Wang, W. Sun, L. Wang et al., Cobalt diselenide (001) surface with short-range Co–Co interaction triggering high-performance electrocatalytic oxygen evolution. *Nano Res.* **14**(12), 4848–4856 (2021). <https://doi.org/10.1007/s12274-021-3444-6>
199. C. Cai, Y. Mi, S. Han, Q. Wang, W. Liu et al., Engineering ordered dendrite-like nickel selenide as electrocatalyst. *Electrochim. Acta* **295**, 92–98 (2019). <https://doi.org/10.1016/j.electacta.2018.10.083>
200. L. Lv, Z. Yang, K. Chen, C. Wang, Y. Xiong, 2D layered double hydroxides for oxygen evolution reaction: from fundamental design to application. *Adv. Energy Mater.* **9**(17), 1803358 (2019). <https://doi.org/10.1002/aenm.201803358>
201. G. Fan, F. Li, D.G. Evans, X. Duan, Catalytic applications of layered double hydroxides: recent advances and perspectives. *Chem. Soc. Rev.* **43**(20), 7040–7066 (2014). <https://doi.org/10.1039/c4cs00160e>
202. D. Zhou, P. Li, X. Lin, A. McKinley, Y. Kuang et al., Layered double hydroxide-based electrocatalysts for the oxygen evolution reaction: identification and tailoring of active sites, and superaerophobic nanoarray electrode assembly. *Chem. Soc. Rev.* **50**, 8790–8817 (2021). <https://doi.org/10.1039/d1cs0186h>
203. D.P. Sahoo, K.K. Das, S. Mansingh, S. Sultana, K. Parida, Recent progress in first row transition metal Layered double hydroxide (LDH) based electrocatalysts towards water splitting: a review with insights on synthesis. *Coord. Chem. Rev.* **469**, 214666 (2022). <https://doi.org/10.1016/j.ccr.2022.214666>

204. Z. Cai, X. Bu, P. Wang, J.C. Ho, J. Yang et al., Recent advances in layered double hydroxide electrocatalysts for the oxygen evolution reaction. *J. Mater. Chem. A* **7**(10), 5069–5089 (2019). <https://doi.org/10.1039/c8ta11273h>
205. L. Yang, Z. Liu, S. Zhu, L. Feng, W. Xing, Ni-based layered double hydroxide catalysts for oxygen evolution reaction. *Mater. Today Phys.* **16**, 100292–100315 (2021). <https://doi.org/10.1016/j.mtphys.2020.100292>
206. N. Zhang, B. Yang, Y. He, Y. He, X. Liu et al., Serpentine $\text{Ni}_3\text{Ge}_2\text{O}_5(\text{OH})_4$ nanosheets with tailored layers and size for efficient oxygen evolution reactions. *Small* **14**(48), 1803015 (2018). <https://doi.org/10.1002/sml.201803015>
207. J.W. Zhao, Z.X. Shi, C.F. Li, L.F. Gu, G.R. Li, Boosting the electrocatalytic performance of NiFe layered double hydroxides for the oxygen evolution reaction by exposing the highly active edge plane (012). *Chem. Sci.* **12**(2), 650–659 (2020). <https://doi.org/10.1039/d0sc04196c>
208. F. Li, Y. Tian, S. Su, C. Wang, D.S. Li et al., Theoretical and experimental exploration of tri-metallic organic frameworks (t-MOFs) for efficient electrocatalytic oxygen evolution reaction. *Appl. Catal. B* **299**, 120665–120674 (2021). <https://doi.org/10.1016/j.apcatb.2021.120665>
209. S. Jin, How to effectively utilize MOFs for electrocatalysis. *ACS Energy Lett.* **4**(6), 1443–1445 (2019). <https://doi.org/10.1021/acscenergylett.9b01134>
210. W. Yang, X. Li, Y. Li, R. Zhu, H. Pang, Applications of metal-organic-framework-derived carbon materials. *Adv. Mater.* **31**(6), 1804740 (2019). <https://doi.org/10.1002/adma.201804740>
211. L. Jiao, Y. Wang, H.L. Jiang, Q. Xu, Metal-organic frameworks as platforms for catalytic applications. *Adv. Mater.* **30**(37), 1703663 (2018). <https://doi.org/10.1002/adma.201703663>
212. L. Xiao, Z. Wang, J. Guan, 2D MOFs and their derivatives for electrocatalytic applications: recent advances and new challenges. *Coord. Chem. Rev.* **472**, 214777 (2022). <https://doi.org/10.1016/j.ccr.2022.214777>
213. J.-E. Zhou, J. Chen, Y. Peng, Y. Zheng, A. Zeb et al., Metal-organic framework-derived transition metal sulfides and their composites for alkali-ion batteries: a review. *Coord. Chem. Rev.* **472**, 214781 (2022). <https://doi.org/10.1016/j.ccr.2022.214781>
214. Y. Xue, Y. Guo, Q. Zhang, Z. Xie, J. Wei et al., MOF-derived Co and Fe species loaded on N-doped carbon networks as efficient oxygen electrocatalysts for Zn-air batteries. *Nano-Micro Lett.* **14**(1), 162 (2022). <https://doi.org/10.1007/s40820-022-00890-w>
215. J. Li, J. Li, J. Ren, H. Hong, D. Liu et al., Electric-field-treated Ni/Co₃O₄ film as high-performance bifunctional electrocatalysts for efficient overall water splitting. *Nano-Micro Lett.* **14**(1), 148 (2022). <https://doi.org/10.1007/s40820-022-00889-3>
216. N.C.S. Selvam, L. Du, B.Y. Xia, P.J. Yoo, B. You, Reconstructed water oxidation electrocatalysts: the impact of surface dynamics on intrinsic activities. *Adv. Funct. Mater.* **31**(12), 2008190 (2021). <https://doi.org/10.1002/adfm.202008190>
217. J. Liu, W. Qiao, Z. Zhu, J. Hu, X. Xu, Chameleon-like reconstruction on redox catalysts adaptive to alkali water electrolysis. *Small* **18**, 2202434 (2022). <https://doi.org/10.1002/sml.202202434>
218. Y. Zeng, M. Zhao, Z. Huang, W. Zhu, J. Zheng et al., Surface reconstruction of water splitting electrocatalysts. *Adv. Energy Mater.* **12**, 2201713 (2022). <https://doi.org/10.1002/aenm.202201713>
219. Z. Chen, R. Zheng, M. Graś, W. Wei, G. Lota et al., Tuning electronic property and surface reconstruction of amorphous iron borides via W-P co-doping for highly efficient oxygen evolution. *Appl. Catal. B.* (2021). <https://doi.org/10.1016/j.apcatb.2021.120037>
220. B. Zhou, R. Gao, J.J. Zou, H. Yang, Surface design strategy of catalysts for water electrolysis. *Small* **18**, 2202336 (2022). <https://doi.org/10.1002/sml.202202336>
221. L. Liu, Z. Jiang, L. Fang, H. Xu, H. Zhang et al., Probing the crystal plane effect of Co₃O₄ for enhanced electrocatalytic performance toward efficient overall water splitting. *ACS Appl. Mater. Interfaces* **9**(33), 27736–27744 (2017). <https://doi.org/10.1021/acsami.7b07793>
222. K. Wu, D. Shen, Q. Meng, J. Wang, Octahedral Co₃O₄ particles with high electrochemical surface area as electrocatalyst for water splitting. *Electrochim. Acta* **288**, 82–90 (2018). <https://doi.org/10.1016/j.electacta.2018.08.067>
223. L. Fang, Z. Jiang, H. Xu, L. Liu, Y. Guan et al., Crystal-plane engineering of NiCo₂O₄ electrocatalysts towards efficient overall water splitting. *J. Catal.* **357**, 238–246 (2018). <https://doi.org/10.1016/j.jcat.2017.11.017>
224. S. Deng, K. Zhang, D. Xie, Y. Zhang, Y. Zhang et al., High-index-faceted Ni₃S₂ branch arrays as bifunctional electrocatalysts for efficient water splitting. *Nano-Micro Lett.* **11**(1), 12–23 (2019). <https://doi.org/10.1007/s40820-019-0242-8>
225. J. Dong, F.Q. Zhang, Y. Yang, Y.B. Zhang, H. He et al., (003)-Facet-exposed Ni₃S₂ nanoporous thin films on nickel foil for efficient water splitting. *Appl. Catal. B* **243**, 693–702 (2019). <https://doi.org/10.1016/j.apcatb.2018.11.003>
226. S. Chu, W. Chen, G. Chen, J. Huang, R. Zhang et al., Holey Ni-Cu phosphide nanosheets as a highly efficient and stable electrocatalyst for hydrogen evolution. *Appl. Catal. B* **243**, 537–545 (2019). <https://doi.org/10.1016/j.apcatb.2018.10.063>
227. C. Zhang, Y. Huang, Y. Yu, J. Zhang, S. Zhuo et al., Sub-11 nm ultrathin porous CoP nanosheets with dominant reactive {200} facets: a high mass activity and efficient electrocatalyst for the hydrogen evolution reaction. *Chem. Sci.* **8**(4), 2769–2775 (2017). <https://doi.org/10.1039/c6sc05687c>
228. H. Xu, Z. Jiang, H. Zhang, L. Liu, L. Fang et al., New efficient electrocatalyst for the hydrogen evolution reaction: erecting a V₂Se₉@Poly(3,4-ethylenedioxythiophene) nanosheet array with a specific active facet exposed. *ACS Energy Lett.* **2**(5), 1099–1104 (2017). <https://doi.org/10.1021/acscenergylett.7b00209>

229. C.H. Kuo, I.M. Mosa, S. Thanneeru, V. Sharma, L. Zhang et al., Facet-dependent catalytic activity of MnO electrocatalysts for oxygen reduction and oxygen evolution reactions. *Chem. Commun.* **51**(27), 5951–5954 (2015). <https://doi.org/10.1039/c5cc01152c>
230. B. Chang, J. Yang, Y. Shao, L. Zhang, W. Fan et al., Bimetallic NiMoN nanowires with a preferential reactive facet: an ultraefficient bifunctional electrocatalyst for overall water splitting. *Chemsuschem* **11**(18), 3198–3207 (2018). <https://doi.org/10.1002/cssc.201801337>

